
Master's Thesis

Design of Spectral Beamsplitter for Hybrid Thermoelectric / Photovoltaic Concentrated Solar Energy Devices

Enok Johannes Haahr Skjølstrup

June 2016



AALBORG UNIVERSITY

Department of Physics and Nanotechnology
Aalborg University
Skjernvej 4A
9220 Aalborg East



AALBORG UNIVERSITY
STUDENT REPORT

Department of Physics and Nanotechnology
Aalborg University
Skjernvej 4A
9220 Aalborg East
Telefon 99 40 92 15
Fax 99 40 92 35
Http://nano.aau.dk

Title:

Design of Spectral Beamsplitter for Hybrid Thermoelectric / Photovoltaic Concentrated Solar Energy Devices

Theme:

Master's Thesis

Project Period:

Spring Semester 2016

Project Group:

5.236

Participant(s):

Enok Johannes Haahr Skjølstrup

Supervisor(s):

Thomas Søndergaard

Copies: 3

Page Numbers: 109

Date of Completion:

June 8, 2016

Synopsis:

The purpose of this thesis is to optimize the design of a beamsplitter for a hybrid system consisting of a solar cell and a thermoelectric element. The beamsplitter consists of more than 100 alternating layers of Si_3N_4 and SiO_2 deposited on glass with an outer layer of MgF_2 , and the thicknesses of all these layers are optimized in order to maximize the efficiency of the hybrid system. Thus the thesis considers the optimization of a complicated function of more than 100 variables.

Two equivalent transfer matrix methods are applied to calculate the transmittance, reflectance, and absorbance through the beamsplitter, and for a microcrystalline and an amorphous solar cell the efficiency of the hybrid system is calculated and optimal thicknesses for the layers are found. Due to higher order band gaps it is found impossible to construct a low-wavelength-pass beamsplitter, but good results are obtained for a high-wavelength-pass beamsplitter. The efficiency of the microcrystalline solar cell is higher than the amorphous, but the relative improvement in efficiency by using the hybrid system with a high-wavelength-pass beamsplitter is almost twice as large for the amorphous.

Contents

Preface	7
Danish Summary	9
1 Introduction	11
1.1 Overview	15
2 The beamsplitter	17
2.1 Maxwell's Equations and the Electromagnetic Wave Equations	17
2.2 Reflection and Transmission at an Interface	18
2.3 Band Gaps in the Beamsplitter	21
2.3.1 Boundary Conditions	22
2.4 The Electric Field Transfer Matrix Method	24
2.4.1 Reciprocity	28
2.5 The Admittance Transfer Matrix Method	29
2.5.1 Transmittance in the Admittance Method	32
2.6 Structure Matrices for the Beamsplitter	33
2.7 Band Gaps described by the Transfer Matrix Methods	34
3 Efficiency of Solar Cells	37
3.1 Efficiency of an Ideal Solar Cell	37
3.1.1 The Solar Spectrum	39
3.2 Efficiency of a Solar Cell with Limiting Factors	40
3.2.1 Quantum Efficiencies	40
3.2.2 The Fill Factor	42
4 Efficiency of Thermoelectric Elements	45
4.1 Thermoelectric effects	45
4.2 Thermoelectric refrigerators	47
4.2.1 Maximal Cooling Power	48
4.3 Thermoelectric Generators	49
4.4 Efficiency of the Hybrid System	51
5 The Optimization Problem	53
5.1 The Initial Guess	53
5.2 The Optimization Methods	54
5.2.1 The Gradient Methods	54
5.2.2 The Nelder-Mead Method	58
6 Matlab Implementation	63
6.1 Applied Data and Verification of the Transfer Matrix Methods	63
6.2 Implementation of the Transfer Matrix Method	64
6.2.1 Implementation of the Initial Guess	65
6.3 Implementation and overview of the Main Program in Matlab	68
6.4 Solution of the Optimization Problem	69
6.4.1 Comparison of Initial and Optimized Structure	70
6.4.2 Test of Convergence of the two Initial Guesses	72

6.4.3	Comparison of the Optimization Methods	73
7	Results	77
7.1	Results for an Ideal Solar Cell	77
7.1.1	Efficiency as a Function of Number of Layers	77
7.1.2	Efficiency as a Function of Incident Angle	80
7.1.3	Effect of Imaginary Refractive Index of MgF_2	81
7.2	Results for a Microcrystalline Solar Cell	82
7.2.1	Efficiency as a Function of Number of Layers	85
7.2.2	Efficiency as a Function of Incident Angle	87
7.3	Results for an Amorphous Solar Cell	89
7.3.1	Efficiency as a Function of Number of Layers	92
7.3.2	Efficiency as a Function of Incident Angle	92
7.4	Orientation of the Beamsplitter	93
7.5	Results for a Low-wavelength-pass Beamsplitter	95
7.5.1	Origin of Higher Order Band Gaps	96
7.5.2	Low-wavelength-pass Beamsplitter for a Microcrystalline Solar Cell .	96
7.5.3	Low-wavelength-pass Beamsplitter for an Amorphous Solar Cell . .	98
7.6	Conclusion on the Results	99
8	Conclusion	101
	Bibliography	103
A	Thicknesses of the Optimized Beamsplitters	105
B	Link to Matlab Code	109

Preface

This report is a master's thesis written by a 10th semester physics student at Aalborg University, Denmark.

The thesis studies the design and optimization of a beamsplitter to be implemented in a hybrid system consisting of a solar cell and a thermoelectric element, and the readers of the thesis are assumed to have some knowledge of optics and optimization.

In the thesis vectors are denoted with an arrow like \vec{E} , unit vectors with a hat like \hat{z} and matrices with a double arrow like \overleftrightarrow{T} . Citations are referred to using the Vancouver method where a reference is denoted with a number like [1] and a bibliography is found in the end of the thesis.

The numerical calculations are made using Matlab R2015b. An important part of the thesis consists of the developed Matlab code which can be found in the author's Dropbox folder from the following link:

<https://www.dropbox.com/sh/i9rm4o4fthu6hsa/AACdq3RaUUDPM-UqDwMjt060a?dl=0>, referred to as [30] during the thesis. To run the code, save all the files from the folder and run the MAIN FILE which calls all the other functions.

A big thanks to Thomas Søndergaard for good supervision and help during the project. Also thanks to the ph.d students Morten Rishøj Thomsen and Søren Jacob Bruun to let me use their super computer to the large computations.

Aalborg University, June 8, 2016.

Danish Summary

I dette speciale er der arbejdet med at optimere designet af en beamsplitter som skal bruges i et hybridsystem sammen med en solcelle og et termoelektrisk element.

Solceller kan omdanne sollys til elektricitet og består af et halvledende materiale, typisk silicium eller galiumarsenid, som bl.a er karakteriseret ved at de har et båndgab. Hvis fotonenergien fra lyset er mindre end båndgabsenergien kan lyset ikke omdannes i solcellen, hvilket medfører at kun lys med bølgelængder under 900-1100 nm kan udnyttes af en solcelle. Idéen med beamsplitteren i specialet er at den kun skal lade de relevante bølgelængder ramme solcellen, mens de længere bølgelængder skal dirigeres til et termoelektrisk element, som termisk kan omdanne varme til elektricitet, hvilket medfører at effektiviteten for hybridsystemet bliver større end for solcellen alene. Beamsplitteren består af mere end 100 lag af skiftevis siliciumnitrid, Si_3N_4 , og siliciumdioxid, SiO_2 , belagt på glas med et ydre lag af magnesiumfluorid, MgF_2 , og specialet handler om at optimere alle disse tykkelser for at opnå højest mulig effektivitet af hybridsystemet. Forskellige designs af hybridsystemet er foreslået, og det er fundet bedst at bruge et design hvor de korte bølgelængder reflekteres til solcellen mens de lange transmitteres til det termoelektriske element.

Specialet består af tre dele. Første del består af kapitel 2 til 5 og indeholder al den relevante teori for specialet. Der tages i kapitel 2 udgangspunkt i Maxwells ligninger som bruges til at opstille en bølgeligning for det elektriske felt i en uendelig beamsplitter, som løses analytisk vha. Blochs teorem og båndgab ses at opstå. Derefter bruges to ækvivalente transfermatrixmetoder til at beregne transmittansen, reflektansen og absorptionskoefficienten gennem en endelig beamsplitter. Der ses at eksistere områder hvor transmittansen er nul, hvilket svarer til båndgabene.

Solceller studeres nærmere i kapitel 3 og udtryk for deres effektivitet udledes. Dette gøres først for en ideel solcelle uden tab, og senere tages effekter med som begrænser effektiviteten og som i langt højere grad beskriver rigtige solceller. Kapitel 4 handler om termoelektriske elementer og et udtryk for deres effektivitet udledes. Ved at kombinere effektiviteterne for solcellen og det termoelektriske element opstilles en samlet effektivitet for hybridsystemet. En teoretisk behandling af optimeringsproblemet findes i kapitel 5, hvor der som startgæt vælges at benytte en kvartbølgestruktur. Tre forskellige optimeringsmetoder studeres i detaljer og deres konvergens analyseres.

Andel del af specialet starter i kapitel 6 hvor teorien fra første del implementeres i Matlab. Optimeringsproblemet løses med de tre implementerede optimeringsmetoder, og Nelder-Mead metoden findes at være klart bedre end gradientmetoderne. Specialets vigtigste resultater findes i kapitel 7, hvor optimerede strukturer for beamsplitteren er beregnet når både en mikrokrystallinsk og en amorf solcelle benyttes. Effektiviteten for en enkelt solcelle er højest for den mikrokrystallinske, men forbedringen i effektivitet ved at anvende hybridsystemet er størst for den amorfe. Dette skyldes at den har en mindre båndgabsbølgelængde og dermed udnytter en mindre del af solspektret. Da den samtidig har en lavere effektivitet end den mikrokrystallinske så er den relative forbedring størst for den amorfe, og er fundet til at være næsten dobbelt så stor som for den mikrokrystallinske. Ved at studere reciprociteten for lys indsendt på beamsplitteren er det fundet bedst at vende beamsplitteren om så lyset er indfaldende fra glassiden. Højere ordens båndgab ses at opstå hvilket forhindrer muligheden for at lave en beamsplitter som transmitterer de korte bølgelængder og reflekterer de lange.

Tredje og sidste del af specialet består af to appendiks.

1. Introduction

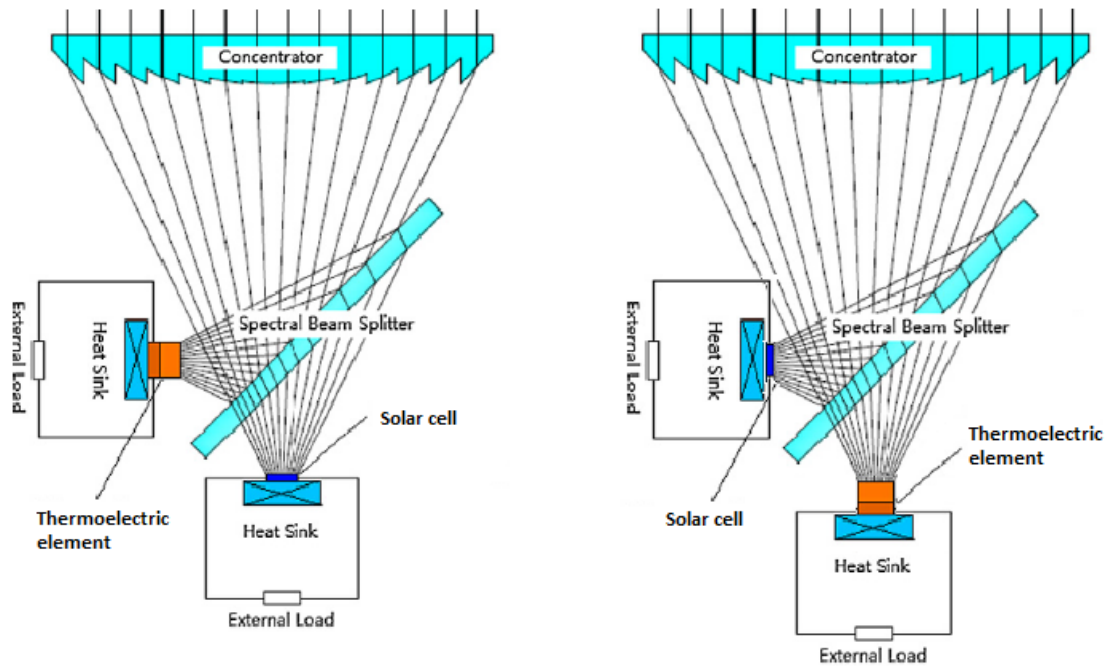
After the oil crisis in the 1970s the world seriously opened the eyes for renewable energy sources instead of coal, oil and gas. Since then several different renewable energy sources have been found and developed such as energy from wind, water and the sun. These three energy sources do not pollute and damage the environment like the fossil fuels coal, oil, and gas do. Over the last 30 years a lot of research has taken place in order to increase the efficiency of these renewable energy sources, especially the solar cells which partly is the topic of this thesis. The solar cells consist of semiconductor materials such as silicon (Si) or Gallium Arsenide (GaAs) and converts the energy from the sun into electricity. These semiconductors have a band gap of approximately 1.1-1.4 eV [32] implying that only light with wavelengths below approximately 900-1100 nm can be converted into electricity. For wavelengths above these values the photon energy of the light is too small and can only be converted to heat in the solar cells which leads to a decrease in their efficiency. [11]

To avoid the waste of energy to heat for the long wavelengths not usable by the solar cell, an idea is to incorporate the solar cell as a component in a hybrid system also consisting of a thermoelectric element as another component, and different designs of the hybrid system have been suggested. The thermoelectric element thermally converts heat into electricity and its efficiency is independent of the wavelengths of light, thus it can utilize the long wavelengths not usable by the solar cell. In [26] two designs are presented, where the first considers a solar cell operating at low temperatures placed on top of a concentrator with a thermoelectric element beneath. The idea in this design is that the long wavelengths not utilized by the solar cell are concentrated onto the thermoelectric element and there converted into electricity. In the other design the position of the solar cell and the concentrator has been switched, such that light is concentrated onto a solar cell placed on top of a thermoelectric element, and in this design the solar cell must be operating at high temperatures. For an illustration of the designs see [26].

For the efficiency of the hybrid system to be as high as possible, it is crucial that the right wavelengths are converted into electricity in the right components. Both the solar cell and the thermoelectric element have an efficiency where only that of the solar cell depends on the wavelength. Hence a cut off wavelength exists that divides the entire wavelength interval from the solar spectrum into different regions, in which the efficiency of one of the components is higher than the other. The wavelengths of the applied solar spectrum range from 280-2500 nm. The cut off wavelengths between these regions determine how to ideally divide the solar spectrum, and if this can be done perfectly a general optimization method for choosing these cut off wavelengths is presented in [4]. Here three different kinds of solar cells are studied in a hybrid system consisting of two different thermoelectric elements, and for perfectly sharp cut off wavelengths the efficiency of the hybrid system is found. The relative improvement of the efficiency compared to single cells is found to be between 11 and 41% depending on the solar cell type and thermoelectric efficiency, thus it is worthwhile researching in such hybrid systems, as their efficiency significantly exceed that of single solar cells.

A disadvantage of the design suggested in [26] is that the long wavelengths have to be transmitted through the solar cell before they enter the thermoelectric element. Some of these wavelengths are maybe reflected by the solar cell and are thereby not utilized anywhere. With the solar cell placed on top of the thermoelectric element it must have a high operating temperature, otherwise the heat decreases its efficiency.

Another design of the hybrid system is suggested in [33], where the idea is to use a



(a) Design of the hybrid system using a low-wavelength-pass beamsplitter, which transmits the short wavelengths onto the solar cell and reflects the long wavelengths onto the thermoelectric element. Figure from [33].

(b) Design of the hybrid system using a high-wavelength-pass beamsplitter, which reflects the short wavelengths onto the solar cell and transmits the long wavelengths onto the thermoelectric element. Figure modified from [33].

Figure 1.1: Two conceptually very different designs of the hybrid system. The left design uses a low-wavelength-pass beamsplitter while a high-wavelength-pass beamsplitter is used at right. Importantly notice that the positions of the solar cell and thermoelectric element are switched in the two designs. The left design is suggested in [33] while the right design is an important modification to be studied in this thesis.

beamsplitter to divide the solar spectrum into the different regions. A concentrator is used to focus the light onto a low-wavelength-pass beamsplitter, which transmits the short wavelengths onto the solar cell and reflects the long wavelengths onto the thermoelectric element as illustrated in Fig. 1.1a. The reason for applying a concentrator is that it is larger than the beamsplitter and is thereby able to collect light from a larger area, implying that more light is directed onto the beamsplitter, and in [33] the concentration ratio can be several hundreds. In addition the price of a concentrator per area is also lower than the price of a beamsplitter per area. A disadvantage in applying the concentrator is that some light is reflected or absorbed in it implying that not all the light is directed onto the beamsplitter, but the gain of receiving more light onto the beamsplitter is greater than the losses in the concentrator. With the design in Fig. 1.1a the solar cell and the thermoelectric element have to be spatially separated in contrast to one of the designs in [26], which is an advantage because present solar cells and thermoelectric elements can be put together as components in the hybrid system once a beamsplitter is constructed. As seen in the figure the incident angle varies across the beamsplitter and is chosen to be 45° in the center, and the deviation from 45° at the edges depends on the concentrator. An idea to yet another design of the hybrid system is found in [2] and is illustrated in Fig. 1.2. Instead on a concentrator as in Fig. 1.1 the sunlight is incident on a large parabolic

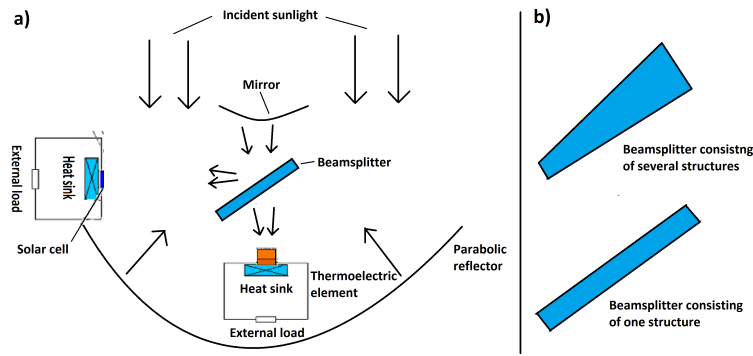
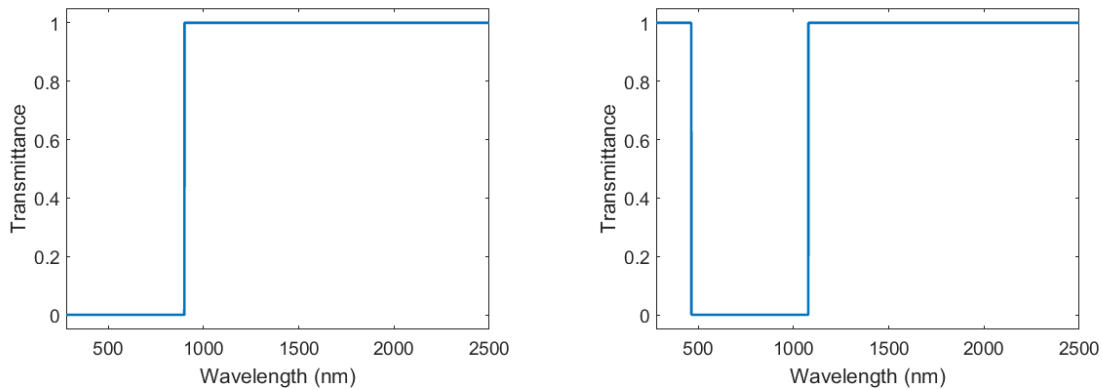


Figure 1.2: Left figure inspired by [2] shows another design of the hybrid system. Incident sunlight hits a large parabolic reflector which reflects the light onto a curved mirror directing it onto a high-wavelength-pass beamsplitter, that reflects the short wavelengths onto the solar cell and transmits the long wavelengths onto the thermoelectric element. Right figure shows two beamsplitters, in the upper one the structure changes across the beamsplitter, while the structure is the same across beamsplitter in the lower .

reflector, which reflects the light onto a curved mirror in the focal point of the reflector. The mirror reflects the light onto a high-wavelength-pass beamsplitter that reflects the short wavelengths onto the solar cell and transmits the long wavelengths onto the thermoelectric element. The advantage of this design is that the reflector is larger than the beamsplitter and is able to collect light that was otherwise not hitting the beamsplitter. A disadvantage of the design is that both the mirror, the beamsplitter, and the thermoelectric element shadow for the light that was intended to hit the reflector. But as before the advantage of applying the reflector is much greater than its disadvantage.

In [33] the structure of the beamsplitter itself is not considered, and is thus assumed to be perfect in that sense that it can transmit the short wavelengths and reflect the long with a perfectly sharp cut off. A solar cell of GaAs is applied and an optimized cut off wavelength is found to be 900 nm. In practice, such a beamsplitter consists of many alternating layers of different materials and can not have a perfectly sharp cut off wavelength. Some of the layers in the beamsplitter can be absorbing, especially for the short wavelengths, and with the design in Fig. 1.1a the short wavelengths have to pass through the entire beamsplitter before they are utilized in the solar cell. A way to avoid this problem is to construct a high-wavelength-pass beamsplitter, which instead reflects the short wavelengths and transmits the long, with the positions of the solar cell and the thermoelectric element switched as illustrated in Fig. 1.1b, which is a modification on the design suggested in [33].

Where [33] assumed a perfect beamsplitter with a perfectly sharp cut off, this thesis investigates theoretically how to construct the beamsplitter. Both designs in Fig. 1.1 are studied, starting with the high-wavelength-pass beamsplitter in Fig. 1.1b and considering a low-wavelength-pass beamsplitter in Sec. 7.5 where it is found that due to higher order band gaps it is impossible to construct. In the thesis first an ideal solar cell with a band gap wavelength of 900 nm is considered in the hybrid system, and later two more realistic solar cells, a microcrystalline and an amorphous, are studied. For the ideal solar cell the efficiency is linearly increasing for wavelengths below the band gap wavelength and zero otherwise, thus the optimal cut off wavelength for the beamsplitter is 900 nm like in [33], and the ideal transmittance is a step function being zero for wavelengths below 900 nm and one otherwise as seen in Fig. 1.3a. In the region where the transmittance is zero, the reflectance is ideally equal to one implying that no absorption is present



(a) Ideal transmittance for a high-wavelength-pass beamsplitter and an ideal solar cell. The wavelength interval from 280-2500 nm is divided into two regions, where the short wavelengths are directed onto the solar cell and the long wavelengths onto the thermoelectric element.

(b) Ideal transmittance for a high-wavelength-pass beamsplitter and a real solar cell. The wavelength interval from 280-2500 nm is divided into three regions, where the short wavelengths are directed onto the thermoelectric element, the medium long onto the solar cell and the long wavelengths onto the thermoelectric element.

Figure 1.3: Ideal transmittances for a high-wavelength-pass beamsplitter for an ideal and a real solar cell.

in an ideal beamsplitter. For real solar cells the efficiency is much lower than in the ideal case, especially for the short and long wavelengths, implying that for real solar cells, a region of small wavelengths where the efficiency is actually smaller than that of the thermoelectric element exists. For such a solar cell the ideal transmittance of the beamsplitter consists of three regions instead of two for the ideal solar cells. For the short wavelengths the transmittance is ideally one, for medium long wavelengths it is zero and for long wavelengths it is one again as illustrated in Fig. 1.3b.

The beamsplitter is constructed using more than 100 alternating layers of silicon nitride, Si_3N_4 , and silicon dioxide, SiO_2 deposited on glass with an outer layer of magnesium fluoride, MgF_2 . The thesis investigates how to choose the thicknesses of all these layers in order to maximize the efficiency of the hybrid system, leading to a huge optimization problem with more than 100 variables. It is furthermore studied how the number of layers in the beamsplitter affect the total efficiency and optimal beamsplitter structures are found for both solar cell types. The efficiency depends on the incident angle and is found when the angle varies from $35\text{-}55^\circ$ for a structure optimized to an angle of 45° . If the efficiency is strongly dependent on angle in that interval, an idea is to compose the beamsplitter of different structures optimized for different incident angles. This is illustrated in the upper part of Fig. 1.2b where the structure varies across the beamsplitter. If the efficiency is almost constant in that interval it is enough to use just one optimized structure for the entire beamsplitter as illustrated in the lower part of Fig. 1.2b, which turns out to be the case for the beamsplitter optimized in this thesis.

1.1 Overview

The thesis overall consists of three parts. The first part consists of chapter 2 to 5 and contains all the relevant theory in the thesis, while the second part in chapter 6 and 7 contains applications and results of the theory. The third part consists of two appendices with tables of optimized thicknesses and link to Matlab code.

In chapter 2 the beamsplitter is introduced as the most important part of the hybrid system. It is studied in detail and the occurrence of band gaps are explained for an infinite beamsplitter. Two equivalent transfer matrix methods dealing with a finite beamsplitter are derived, and they are shown to give the same results as the infinite beamsplitter when the number of layers is large enough. Furthermore the structure matrix for the beamsplitter considered in the thesis is introduced.

The solar cell is introduced in chapter 3 as another component of the hybrid system. First an ideal solar cell without any loss is considered and a theoretical limit of its efficiency is found. Afterwards limiting factors are introduced in order to describe a real solar cell and an expression for its efficiency derived.

In chapter 4 the thermoelectric element is introduced as the last component of the hybrid system. The basic principles behind thermoelectricity is explained and an expression for the efficiency of the thermoelectric element is derived.

Chapter 5 deals with the optimization problem where the initial guess is first presented. Afterwards three different optimization methods are studied in detail in order to solve the optimization problem.

Chapter 6 contains a Matlab implementation of the theory derived in chapter 2 to 5. The transfer matrix methods are implemented and verified and a solution of the optimization problem using the three optimization methods is given. The optimized structure is compared to that of the initial guess to assess the quality of the optimization, and the three optimization methods are compared based on their performance and time consumption.

In chapter 7 the important results in the thesis are presented, starting with the results for an ideal solar cell. The efficiency is found as a function of number of layers and incident angle, and the same is done for a microcrystalline and an amorphous solar cell. The orientation of the beamsplitter is considered, and the low-wavelength-pass beamsplitter is studied and is found to be impossible to construct due to higher order band gaps.

A conclusion of the thesis is found in chapter 8 and the two appendices are found at the end of the thesis.

2. The beamsplitter

In this chapter the beamsplitter is studied in detail as it is the most important component of the hybrid system. It is constructed of alternating layers of silicon nitride, Si_3N_4 , and silicon dioxide SiO_2 deposited on glass with an outer layer of magnesium fluoride, MgF_2 , to reduce the reflectance from air into the beamsplitter.

First the basic theory dealing with an infinite beamsplitter is explained, starting with Maxwell's equations and ending with a solution of the wave equation in the beamsplitter, and it is seen that band gaps occur. Two transfer matrix methods are introduced which are available for a finite beamsplitter. The first considers only the electric field but treats both its normal and tangential components, while the second considers both the electric and magnetic field but treats only the tangential component of the fields. The methods are equivalent and the first is called the electric field method while the second is called the admittance method. In Sec. 6.2 it will be investigated which method gives the fastest result when implemented in Matlab.

2.1 Maxwell's Equations and the Electromagnetic Wave Equations

The macroscopic Maxwell's equations are given by

$$\vec{\nabla} \times \vec{E}(\vec{r}, t) = -\frac{\partial \vec{B}(\vec{r}, t)}{\partial t}, \quad (2.1)$$

$$\vec{\nabla} \times \vec{H}(\vec{r}, t) = \frac{\partial \vec{D}(\vec{r}, t)}{\partial t} + \vec{J}(\vec{r}, t), \quad (2.2)$$

$$\vec{\nabla} \cdot \vec{D}(\vec{r}, t) = \rho(\vec{r}, t), \quad (2.3)$$

$$\vec{\nabla} \cdot \vec{B}(\vec{r}, t) = 0. \quad (2.4)$$

Here \vec{E} is the electric field, \vec{D} the electric displacement, \vec{H} the magnetic field, \vec{B} the magnetic induction, \vec{J} the current density and ρ the charge density, which are all functions of position \vec{r} and time t . Introducing the macroscopic polarization \vec{P} and magnetization \vec{M} the general constitutive relations which describe the properties of the medium under influence of the fields are given by

$$\vec{D}(\vec{r}, t) = \varepsilon_0 \vec{E}(\vec{r}, t) + \vec{P}(\vec{r}, t), \quad (2.5)$$

$$\vec{H}(\vec{r}, t) = \mu_0^{-1} \vec{B}(\vec{r}, t) - \vec{M}(\vec{r}, t), \quad (2.6)$$

where ε_0 is the permittivity of vacuum and μ_0 the permeability of vacuum. Throughout this thesis only non-magnetic materials are considered, i.e. $\vec{M}(\vec{r}, t) = \vec{0}$ such that $\vec{B}(\vec{r}, t) = \mu_0 \vec{H}(\vec{r}, t)$ and the relative permeabilities are $\mu(\vec{r}) = 1$ for all the considered materials. Furthermore, materials are assumed linear, local and isotropic, resulting in $\vec{D}(\vec{r}) = \varepsilon_0 \varepsilon(\vec{r}) \vec{E}(\vec{r})$ and the effect of induced charge and current densities are incorporated into the dielectric constants $\varepsilon(\vec{r})$ of the materials. [25] In addition only materials without free charges or free currents are studied.

Maxwell's equations in Eq. (2.1) to (2.4) are linear differential equations, where the operators $\vec{\nabla} \times$ and $\vec{\nabla} \cdot$ only work on the spatial part and $\frac{\partial}{\partial t}$ only works on the temporal part. Hence the solution of the equations can be split up into a product of a spatial and a temporal part. Working with monochromatic waves and $e^{-i\omega t}$ as the time dependence,

the fields can be expressed as

$$\vec{E}(\vec{r}, t) = \vec{E}(\vec{r})e^{-i\omega t} \quad \text{and} \quad \vec{H}(\vec{r}, t) = \vec{H}(\vec{r})e^{-i\omega t}. \quad (2.7)$$

The wave equations are derived using Maxwell's equations where all the fields vary as in Eq. (2.7). Taking the curl of Eq. (2.1) and substituting the expression for $\vec{\nabla} \times \vec{H}$ from Eq. (2.2) gives

$$\vec{\nabla} \times \vec{\nabla} \times \vec{E}(\vec{r}) - k_0^2 \varepsilon(\vec{r}) \vec{E}(\vec{r}) = \vec{0}, \quad (2.8)$$

where $k_0 = \omega/c$ is the wave number in vacuum and c is the speed of light in vacuum. Analogue calculations can be made for the magnetic field, which results in the wave equation [25]

$$\vec{\nabla} \times \frac{1}{\varepsilon(\vec{r})} \vec{\nabla} \times \vec{H}(\vec{r}) - k_0^2 \vec{H}(\vec{r}) = \vec{0}. \quad (2.9)$$

Applying the vector identity $\vec{\nabla} \times \vec{\nabla} \times = \vec{\nabla} \vec{\nabla} \cdot - \nabla^2$ from [16] and using that $\vec{\nabla} \cdot \vec{E} = 0$ because of no free charges, the wave equation in Eq. (2.8) can be written as

$$\nabla^2 \vec{E}(\vec{r}) + k_0^2 \varepsilon(\vec{r}) \vec{E}(\vec{r}) = \vec{0}. \quad (2.10)$$

Dividing this equation by $\varepsilon(\vec{r})$ an eigenvalue problem appears, where the operator $\frac{1}{\varepsilon(\vec{r})} \nabla^2$ works on the eigenfunctions $\vec{E}(\vec{r})$, giving rise to the eigenvalues $-k_0^2$. Similar Eq. (2.9) is an eigenvalue problem for the magnetic field. The primary focus will now be on solving these wave equations for the electric and magnetic field in the beamsplitter. But before this can be done it is necessary to know how the fields behave across all the interfaces in the beamsplitter, and therefore the next section deals with reflections and transmission at an interface.

2.2 Reflection and Transmission at an Interface

As mentioned the beamsplitter consists of alternating layers of materials with different refractive index. At each interface in the beamsplitter some light is reflected and some light is transmitted, and this happens in accordance with the following boundary conditions at an interface between material 1 and 2. [16]

$$E_{1t} = E_{2t}, \quad \varepsilon_1 E_{1n} = \varepsilon_2 E_{2n}, \quad H_{1t} = H_{2t}, \quad \mu_1 H_{1n} = \mu_2 H_{2n}, \quad (2.11)$$

where the number denotes the medium while t and n denotes the tangential and normal part of the fields, respectively.

When an arbitrarily polarized plane wave is incident at an interface, it can be split up into an s polarized plane wave and a p polarized plane wave. For s polarization the electric field is parallel to the interface, while for p polarization the magnetic field is parallel to the interface, as illustrated in Fig. 2.1 where only the electric fields are shown. The interface separates two media with dielectric constants ε_1 and ε_2 , which in general can be complex. The incident plane wave is given by $\vec{E}_1 e^{i(\vec{k}_1 \cdot \vec{r} - \omega t)}$, thus propagating in the direction of \vec{k}_1 which lies in the xz plane of the figures and $(\vec{k}_1, \vec{E}_1, \vec{H}_1)$ form a right handed set. The reflected wave is propagating in the direction of \vec{k}_{1r} whose z component is opposite to that of \vec{k}_1 . In order for $(\vec{k}_{1r}, \vec{E}_{1r}, \vec{H}_{1r})$ to be a right handed set either the tangential part of \vec{E}_{1r} or \vec{H}_{1r} must change sign compared to the incident wave. In [25] the sign change for p polarization occurs for the electric field while it occurs for the magnetic field in [19],

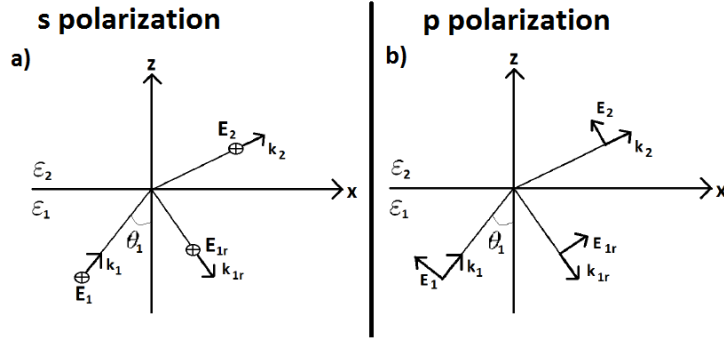


Figure 2.1: Reflection and transmission for *s* and *p* polarization. For *s* polarization the electric field is parallel to the interface thus along the *y* axis, while for *p* polarization the electric field is in the *xz* plane. Figure inspired by [25].

and for *s* polarization the sign change occurs for the magnetic field in both books. In this thesis it is chosen to stick to the convention in [25] as seen in Fig. 2.1. It is seen in the figures that the *x*-component of \vec{k}_1 must be conserved across the interface, while the *z*-component changes. The propagation directions in the two media are thus given by

$$\vec{k}_1 = (k_x, k_{z1}), \quad \vec{k}_2 = (k_x, k_{z2}), \quad (2.12)$$

where the norm of the vectors are $k_1 = |\vec{k}_1| = k_0 n_1$ and $k_2 = |\vec{k}_2| = k_0 n_2$, respectively, where $n = \sqrt{\epsilon}$ is the refractive index of the materials.

It is seen in the figures that the conserved *x*-component of the propagation direction is given by

$$k_x = k_1 \sin(\theta_1), \quad (2.13)$$

where θ_1 is the angle of incidence as illustrated in the figure. The *z*-components of the propagation directions are thus given by

$$k_{z1} = \sqrt{k_0^2 \epsilon_1 - k_x^2}, \quad k_{z2} = \sqrt{k_0^2 \epsilon_2 - k_x^2} \quad (2.14)$$

It is noticed that these two components in general can be complex thus describing evanescent waves, which is a wave propagating in one direction and exponentially damped in another direction. This happens when the argument of the square root in Eq. (2.14) becomes negative, i.e when $1 - n_1/n_2 \sin^2 \theta_1 < 0$. This is never fulfilled if $n_1 < n_2$, thus the transmitted wave is always propagating if the incident medium has a lower refractive index than the receiving medium. Thereby a propagating transmitted wave always exist when light is incident from air into any material. In the other case, $n_1 > n_2$, evanescent waves occur if the incident angle exceeds the critical angle given by $\theta_c = \sin^{-1}(n_2/n_1)$ and total internal reflection occurs.

The reflection and transmission depend on the polarization, and can be calculated using the Fresnel reflection and transmission coefficients which for *s* polarization can be written as [25]

$$\rho_{12}^s(\theta_1) = \frac{k_{z1} - k_{z2}}{k_{z1} + k_{z2}}, \quad \tau_{12}^s(\theta_1) = \frac{2\sqrt{k_{z1}k_{z2}}}{k_{z1} + k_{z2}}, \quad (2.15)$$

and for p polarization written as

$$\rho_{12}^p(\theta_1) = \frac{\varepsilon_2 k_{z1} - \varepsilon_1 k_{z2}}{\varepsilon_2 k_{z1} + \varepsilon_1 k_{z2}}, \quad \tau_{12}^p(\theta_1) = \frac{2n_1 n_2 \sqrt{k_{z1} k_{z2}}}{\varepsilon_2 k_{z1} + \varepsilon_1 k_{z2}}. \quad (2.16)$$

It is important to remember that these coefficients apply when the light is incident from medium 1 into medium 2 denoted by the subscript 12. Furthermore $\rho_{12} = -\rho_{21}$, $\tau_{12} = \tau_{21}$ and $|\rho_{12}|^2 + |\tau_{12}|^2 = 1$ for both polarizations. This is different from [25] where the condition is $|\rho_{12}|^2 + k_{z2}/k_{z1} |\tau_{12}|^2 = 1$, but the coefficients in Eq. (2.15) and (2.16) have the factor k_{z2}/k_{z1} incorporated. It is furthermore noticed that the condition $|\rho_{12}|^2 + |\tau_{12}|^2 = 1$ is only true when both k_{z1} and k_{z2} are real. Imaginary wave vectors can be due to either total internal reflection or imaginary refractive indices, and in both cases it is difficult to define transmittance. Any measurement of light intensity is hard to make in an absorbing media, as the intensity depends on the measurement position. The beamsplitter considered in this thesis is surrounded by air on both sides, hence it makes sense to define the transmittance as the ratio of light intensities transmitted and incident on the beamsplitter as both these intensities are measured in air, which is a non-absorbing medium.

The amplitude of the reflected and transmitted fields are for both polarizations given by

$$E_2(\vec{r}) = \tau_{12}(\theta_1) E_1(\vec{r}), \quad E_{1r}(\vec{r}) = \rho_{12}(\theta_1) E_1(\vec{r}). \quad (2.17)$$

It is noticed that all the coefficients depend on the incident angle θ_1 . This is due to the fact that k_x depends on θ_1 through Eq. (2.13), while k_{z1} and k_{z2} depends on k_x through Eq. (2.14) and hence also on θ_1 . It is possible to write down an explicit expression for the coefficients depending on θ_1 , but in practice the coefficients are applied as they are written now.

For p polarized light the Brewster angle θ_B is the angle of incidence where all the light is transmitted through the interface and no light is reflected. The physical understanding of this phenomena is due to the oscillating electric dipoles in the materials, which do not radiate at all in the direction of their dipole moments. [25] Hence when p polarized light is incident at an interface where the incident angle equals the Brewster angle, the dipole moments of the refracted light point in the same direction as the reflected light was supposed to. These dipoles do not radiate in this direction, and therefore no reflected light is found. This happens when $\theta_1 + \theta_2 = 90^\circ$, where θ_1 is the incident angle and θ_2 is the refracted angle, and from Snell's law $n_1 \sin \theta_1 = n_2 \sin \theta_2$ with $\theta_1 = \theta_B$ the Brewster angle is found to be [17]

$$\theta_B = \tan^{-1} \left(\frac{n_2}{n_1} \right). \quad (2.18)$$

It is noticed that the Brewster angle only exists for p polarization. For s polarization the electric field is parallel to the interface implying that all the dipole moments also are parallel to the interface, thus reflected light always exists.

With the achieved knowledge about how the fields and wave vectors behave across an interface, the next section deals with the beamsplitter, and analytic solutions of the wave equations in Eq. (2.9) and (2.10) are found.

2.3 Band Gaps in the Beamsplitter

In this section the beamsplitter is introduced, where it is assumed that it consists of infinitely many layers, and the origin of band gaps are explained. This is done by solving the wave equations in Eq. (2.9) and (2.10) by applying Bloch's theorem. Later in Sec. 2.4 a method dealing with a beamsplitter consisting of only a finite number of layers will be derived, and it is shown that if the number of layers is large enough, the same results are obtained as for the infinite structure.

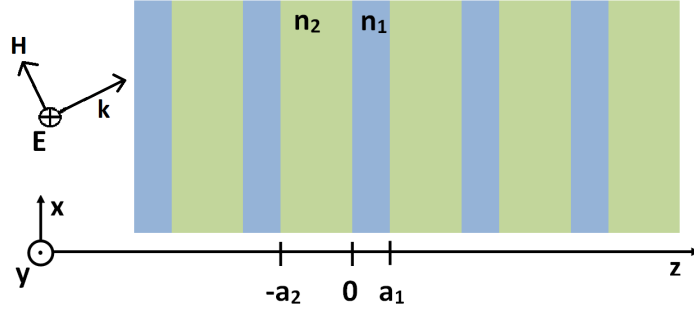


Figure 2.2: The beamsplitter consisting of two different materials. The blue regions describe material 1 with refractive index n_1 and thickness a_1 while the green regions describe material 2 with refractive index n_2 and thickness a_2 . In this section it is assumed that this structure is repeated infinitely many times. s polarized light with direction given by \vec{k} in the xz plane is incident on the beamsplitter, giving rise to an electric field parallel with all the interfaces. Figure inspired by [28].

The beamsplitter shown in Fig. 2.2 consists of two different materials and is periodic in the z direction and considered as infinite in the other directions. The blue regions describe material 1 with refractive index n_1 and thickness a_1 while the green regions describe material 2 with refractive index n_2 and thickness a_2 , and the total period is $\vec{\Lambda} = \Lambda \hat{z} = (a_1 + a_2) \hat{z}$. In the figure the light is s polarized and this case is studied in detail where the focus is on solving the wave equation for the electric field in Eq. (2.10), and similar calculations can be made for p polarized light for solving the wave equation for the magnetic field in Eq. (2.9). For the beamsplitter in Fig. 2.2 the wave equation in Eq. (2.10) is valid in both media, and can thus be written as [28]

$$\nabla^2 \vec{E}(\vec{r}) = \begin{cases} -k_1^2 \vec{E}(\vec{r}), & 0 < z < a_1 \\ -k_2^2 \vec{E}(\vec{r}), & -a_2 < z < 0. \end{cases} \quad (2.19)$$

k_x is conserved through the structure, hence a solution of Eq. (2.19) is given by [25]

$$\vec{E}(\vec{r}) = \begin{cases} (Ae^{ik_{z1}z} + Be^{-ik_{z1}z})e^{ik_x x} \hat{y}, & 0 < z < a_1 \\ (Ce^{ik_{z2}z} + De^{-ik_{z2}z})e^{ik_x x} \hat{y}, & -a_2 < z < 0, \end{cases} \quad (2.20)$$

where it is remembered from Eq. (2.12) that $k_x^2 + k_{zj}^2 = k_j^2$ for $j = \{1, 2\}$, and A, B, C and D are constants. In the rest of this section, only the magnitude $E(\vec{r})$ of the field in Eq. (2.20) is considered, where $\vec{E}(\vec{r}) = E(\vec{r}) \hat{y}$ and only a two dimensional position vector $\vec{r} = (x, z)$ is considered.

The solution in Eq. (2.20) is only valid inside one period from $-a_2$ to a_1 , and to find the

electric field outside this period Blochs theorem is used, which states that

$$E(\vec{r}) = e^{i\vec{k}_B \cdot \vec{r}} u_{\vec{k}_B}(z), \quad (2.21)$$

where $u_{\vec{k}_B}(z)$ is a function that is periodic in the z direction with same period Λ as the structure, and \vec{k}_B is a Bloch wave vector which is different from \vec{k}_1 and \vec{k}_2 . If the entire beamsplitter was made of material 1 the field will propagate with wave vector \vec{k}_1 , and similar with \vec{k}_2 if the entire beamsplitter was made of material 2. But when the two materials are put together to form the beamsplitter, the wave vector is not just alternating between \vec{k}_1 and \vec{k}_2 in the two materials. Reflection occurs at every interface giving rise to interference between the different waves which influences the propagation. Hence in the beamsplitter the electric field is propagating as a plane wave modulated by a periodic function with the same period as the structure. For a position outside the first period the field is found using Eq. (2.21)

$$E(\vec{r} + \vec{\Lambda}) = e^{ik_B \cdot (\vec{r} + \vec{\Lambda})} u_{\vec{k}_B}(z + \Lambda) = e^{ik_B \cdot \vec{r}} u_{\vec{k}_B}(z) e^{ik_{Bz}\Lambda} = E(\vec{r}) e^{ik_{Bz}\Lambda}, \quad (2.22)$$

where k_{Bz} is the z component of k_B . Because of the periodicity of the structure in the z direction it is enough to describe the field for Bloch wave vectors inside 1. Brillouin zone thus $-\pi/\Lambda \leq k_{Bz} \leq \pi/\Lambda$. Applying Eq. (2.22) the electric field can be calculated at an arbitrary position in the beamsplitter. [28]

2.3.1 Boundary Conditions

For the solution in Eq. (2.20) to describe a physical field it must fulfil the boundary conditions in Eq. (2.11). For s polarization the electric field is entirely tangential, so at the interface $z = 0$ the coefficients in Eq. (2.20) must satisfy

$$A + B = C + D, \quad (2.23)$$

From Maxwell's equations $\vec{\nabla} \times \vec{E} = i\omega\mu_0\vec{H}$, thus the tangential part of \vec{H} is $H_x = 1/i\omega\mu_0(\vec{\nabla} \times \vec{E})_x = 1/i\omega\mu_0 \frac{\partial E(\vec{r})}{\partial z}$. Thus differentiating the field in Eq. (2.20) with respect to z and inserting $z = 0$ yields

$$k_{z1}(A - B) = k_{z2}(C - D). \quad (2.24)$$

These two equations contain four unknowns, thus to solve them Blochs theorem as expressed in Eq. (2.22) is applied. At the interface $z = a_1$ the electric field must satisfy $E(x, a_1) = E(x, -a_2 + \Lambda) = E(x, -a_2) e^{ik_{Bz}\Lambda}$, yielding

$$Ae^{ik_{z1}a_1} + Be^{-ik_{z1}a_1} = (Ce^{-ik_{z2}a_2} + De^{ik_{z2}a_2}) e^{ik_{Bz}\Lambda}. \quad (2.25)$$

The same is done with the differentiated field at the interface $z = a_1$ yielding

$$k_{z1} (Ae^{ik_{z1}a_1} - Be^{-ik_{z1}a_1}) = k_{z2} (Ce^{-ik_{z2}a_2} - De^{ik_{z2}a_2}) e^{ik_{Bz}\Lambda}. \quad (2.26)$$

The four equations in Eq. (2.23) to (2.26) contain four unknowns and can thus be solved. Exactly the same can be done for p polarization where the wave equation for the magnetic field in Eq. (2.9) simplifies to

$$\nabla^2 \vec{H}(\vec{r}) = \begin{cases} -k_1^2 \vec{H}(\vec{r}), & 0 < z < a_1 \\ -k_2^2 \vec{H}(\vec{r}), & -a_2 < z < 0, \end{cases} \quad (2.27)$$

2.3. Band Gaps in the Beamsplitter

because $\varepsilon(\vec{r})$ is a constant in each layer and can thus be taken outside the curl operator in Eq. (2.9). Hence it is seen that Eq. (2.27) is similar to Eq. (2.19) with \vec{H} replaced by \vec{E} . Four equations with four unknowns are found and it can be shown that the non-trivial solution occurs when the following equation is satisfied

$$\cos(k_B \Lambda) = \cos(a_1 k_{z1}) \cos(a_2 k_{z2}) - \frac{1}{2} \left(p_m + \frac{1}{p_m} \right) \sin(a_1 k_{z1}) \sin(a_2 k_{z2}), \quad (2.28)$$

where p_m depends on the polarization like

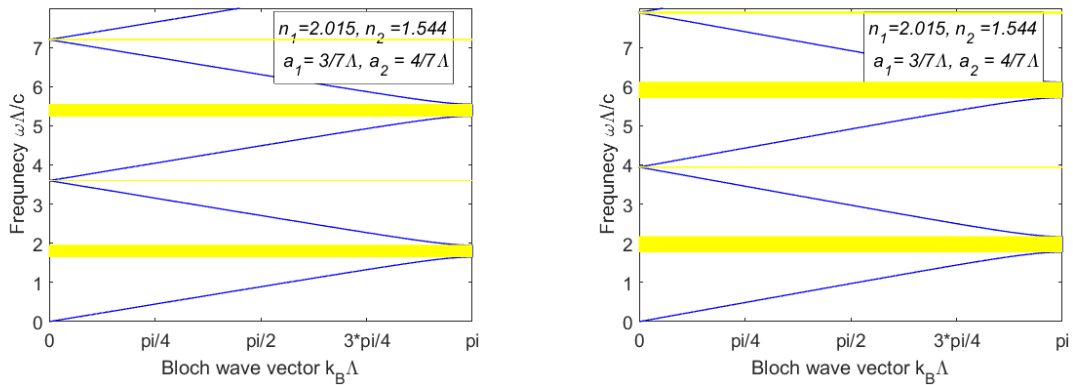
$$p_m = \begin{cases} \frac{k_{z2}}{k_{z1}}, & \text{for s polarization} \\ \frac{k_{z2} \varepsilon_1}{k_{z1} \varepsilon_2}, & \text{for p polarization.} \end{cases} \quad (2.29)$$

Since $\cos(k_B \Lambda)$ is always between -1 and 1 for a real k_B , solutions to Eq. (2.28) only exist when the absolute value of its right hand side does not exceed unity. Otherwise the Bloch wave vector k_B becomes imaginary and the wave becomes exponentially damped, which in an infinite beamsplitter means that it can not propagate. Hence there are some frequencies where no waves can propagate through the beamsplitter, and these frequencies are called band gaps and can be seen on a dispersion relation. [25] When sine and cosine are periodic functions, the right hand side of Eq. (2.28) becomes periodic, implying that band gaps also occur at higher frequencies. These are called higher order band gaps and will be further explained in Sec. 7.5.1.

The sizes of the band gaps depend on the refractive indices and the thicknesses of the materials, and greater difference between the refractive indices results in larger band gaps. A way to choose the thicknesses of the materials to maximize the band gap is to make the structure as quarter wave layers, where the idea is to achieve constructive interference between the beams reflected from the front and back of each interface. The phase change for a reflection at an interface from low refractive index to higher refractive index is π , and to achieve constructive interference, the phase shift from propagating in one direction in every medium must be $\pi/2$. It can be shown that this occurs when the thicknesses are given by [17]

$$a_1 = \frac{\lambda_0}{4n_1 \cos \theta_1} \quad \text{and} \quad a_2 = \frac{\lambda_0}{4n_2 \cos \theta_2} \quad (2.30)$$

where θ_1 and θ_2 are the propagation angles in the respective materials, and can be calculated using Snell's law and λ_0 is the design wavelength at which the band gap is desired. Two examples of dispersion relations are shown in Fig. 2.3 where the refractive indices are $n_1 = 2.015$ and $n_2 = 1.544$ and the light is s polarized. To have a maximal band gap around 600 nm the structure must consist a quarter wave layers in accordance with Eq. (2.30), thus the thicknesses are chosen to be $a_1 = 75$ nm and $a_2 = 100$ nm for an incident angle of 0° . The band gaps are marked with yellow rectangles and are seen to be periodic. For a quarter wave structure the small band gaps disappear, and the reason for those in the figures is that the structure is only close to a quarter wave structure, this will be elaborated in Sec. 7.5.1. These figures are further developments of [23], which is the authors 4th semester project at Aalborg University, and only considered the band gaps in photonic crystals with light incident perpendicular to the structure. This is the case in Fig. 2.3a while the incident angle is 45° in Fig. 2.3b. The thicknesses of the materials are the same in the two figures and are almost quarter wave layers for an incident angle of 0° , and the thicknesses will change if the angle was 45° . In the figures the band gaps are seen to occur at a higher frequency for 45° than for 0° . Notice that these figures are only valid for s polarization, and similar figures can be made for p polarization.



(a) Dispersion relation for an incident angle of 0° , where the yellow rectangles mark the band gaps.

(b) Dispersion relation for an incident angle of 45° , where the yellow rectangles mark the band gaps.

Figure 2.3: Dispersion relations for incident angles of 0° and 45° . Notice that the band gaps occur at higher frequency for 45° than for 0° .

The wave equations in Eq. (2.9) and (2.10) are scale invariant with respect to length, and it can thus be shown that the size of the band gap $\Delta\lambda$ scales linear with the thicknesses of the materials when their refractive indices are kept constant. The middle of the band gap, λ_m scales linear too, and the gap-midgap ratio $\Delta\lambda/\lambda_m$ becomes independent of the thicknesses, and is a more useful characterization than the band gap size. [15] Due to the scale invariance it is convenient to work with dimensionless units in the dispersion relation, which is achieved by normalising the thicknesses of the individual layers by the total period. Similar the frequency and the Bloch wave vector are normalised resulting in [28]

$$d_1 = \frac{a_1}{\Lambda}, \quad d_2 = \frac{a_2}{\Lambda} \quad (2.31)$$

$$K = k_B\Lambda, \quad \Omega = k_0\Lambda = \frac{\omega}{c}\Lambda \quad (2.32)$$

With these thicknesses the period is $\Lambda = 175\text{nm}$ and the dimensionless thicknesses become $d_1 = \frac{3}{7}$ and $d_2 = \frac{4}{7}$, and these thicknesses are used in the dispersion relations in Fig. 2.3.

2.4 The Electric Field Transfer Matrix Method

Until now only an infinite beamsplitter has been studied and the occurrence of band gaps have been explained. A way to deal with a finite beamsplitter is by transfer matrix methods, which describe how the field changes through the structure. It is difficult to measure the band gaps directly, and a way to deal with this problem is to consider the transmittance through the crystal, which is defined as the ratio of the intensity of the light that has passed through the crystal and the intensity of the incident light. If the transmittance is zero at some frequency no light can propagate and a band gap exists at that frequency. Therefore in this section based on [17] it is shown how to calculate the transmittance through a beamsplitter by using the electric field transfer matrix method. Throughout this section light is incident from left and any measurement must take place to the right of the crystal. In Sec. 2.4.1 reciprocity is studied where light is incident from right and a measurement takes place at left of the crystal.

2.4. The Electric Field Transfer Matrix Method

As mentioned in Sec. 2.2 a part of the light is reflected at every interface and another part transmitted. Hence in each layer there are forward and backward propagating waves which is also seen in the solution of the electric field in Eq. (2.20). Inside a material the magnitude of the electric field can be written as

$$E(\vec{r}) = (E^+ e^{ik_z z} + E^- e^{-ik_z z}) e^{ik_x x}, \quad (2.33)$$

where E^+ and E^- describe the fields propagating forth and back, respectively. The case of a single medium with refractive index n and thickness a is illustrated in Fig. 2.4, where light is incident perpendicular to the medium to simplify the figure which is the case for all figures in this section. The incident angle is incorporated into k_z , see Eq. (2.13) and

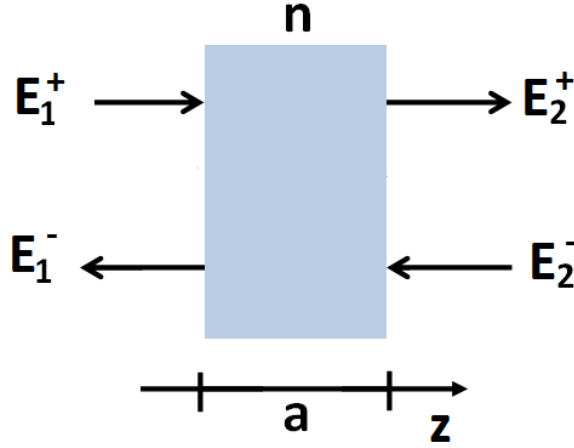


Figure 2.4: Propagation in a medium with refractive index n and thickness a . Figure from [23].

(2.14). The propagation in the medium is described by the matrix

$$\overset{\leftrightarrow}{T} = \begin{pmatrix} e^{ik_z a} & 0 \\ 0 & e^{-ik_z a} \end{pmatrix}. \quad (2.34)$$

Hence the field after propagation through the material is given by

$$\begin{pmatrix} E_2^+ \\ E_2^- \end{pmatrix} = \overset{\leftrightarrow}{T} \begin{pmatrix} E_1^+ \\ E_1^- \end{pmatrix}, \quad (2.35)$$

where the field changes from (E_1^+, E_1^-) to (E_2^+, E_2^-) . It is noticed that Eq. (2.35) gives the fields after propagation in terms of the incident fields. This is opposite to e.g [17] where the incident field is given in terms of the propagated fields, thus described by

$$\begin{pmatrix} E_1^+ \\ E_1^- \end{pmatrix} = \overset{\leftrightarrow}{S} \begin{pmatrix} E_2^+ \\ E_2^- \end{pmatrix}, \quad (2.36)$$

where $\overset{\leftrightarrow}{S} = \overset{\leftrightarrow}{T}^{-1}$. The procedure of the transfer matrix method considered in this thesis is different from [17], because the methods consider the structure from different sides but the results are shown to be equivalent.

At an interface between materials with refractive indices n_1 and n_2 both reflection and transmission occur as explained in Sec. 2.3.1, and is illustrated in Fig. 2.5. It can be shown that the interface is described by the matrix

$$\overset{\leftrightarrow}{T}_{12} = \frac{1}{\tau_{21}} \begin{pmatrix} 1 & -\rho_{12} \\ -\rho_{12} & 1 \end{pmatrix}, \quad (2.37)$$

where ρ_{12} and τ_{21} are the reflection and transmission coefficients in Eq. (2.15) and (2.16), and it is remembered that $\tau_{12} = \tau_{21}$. Hence the field after the interface is given by

$$\begin{pmatrix} E_2^+ \\ E_2^- \end{pmatrix} = \overset{\leftrightarrow}{T}_{12} \begin{pmatrix} E_1^+ \\ E_1^- \end{pmatrix}. \quad (2.38)$$

This is again opposite to [17] where

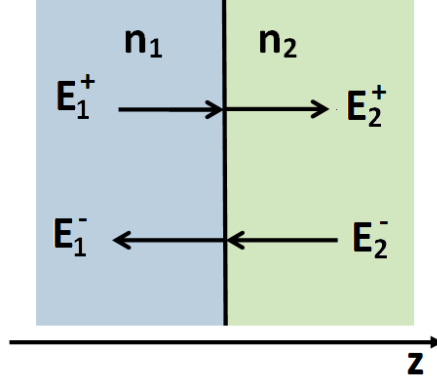


Figure 2.5: Interface between two media with refractive indices n_1 and n_2 . Figure from [23].

$$\begin{pmatrix} E_1^+ \\ E_1^- \end{pmatrix} = \frac{1}{\tau_{12}} \begin{pmatrix} 1 & \rho_{12} \\ \rho_{12} & 1 \end{pmatrix} \begin{pmatrix} E_2^+ \\ E_2^- \end{pmatrix}. \quad (2.39)$$

It can be shown that $\overset{\leftrightarrow}{T}_{12} = \overset{\leftrightarrow}{T}_{21}^{-1}$, hence Eq. (2.38) and (2.39) are equivalent.

The two kinds of matrices in Eq. (2.34) and (2.37) serve as building blocks in the electric field transfer matrix method, because any beamsplitter can be described by appropriate multiplications of these matrices. For the beamsplitter in Fig. 2.2 a unit cell can be defined as the smallest possible structure that is repeated, and is illustrated in Fig. 2.6. First the field is refracted into the cell, then it propagates a distance a_1 in material 1, then it is refracted at an interface and propagates a distance a_2 in material 2. The dotted line at the right of the figure is not included in the unit cell, because it is equivalent to the most left line and must not be included twice.

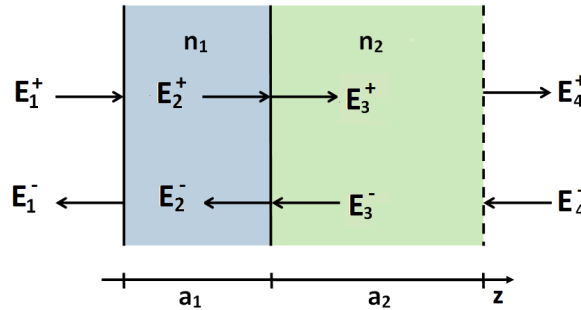


Figure 2.6: Unit cell where the field first is refracted into the structure, then it propagates a distance a_1 in material 1, then it is refracted at an interface and propagates a distance a_2 in material 2. The dotted line at the right of the figure is not included in the unit cell. Figure from [23].

The unit cell can be described by the matrix

$$\begin{pmatrix} E_4^+ \\ E_4^- \end{pmatrix} = \overset{\leftrightarrow}{T}_2 \overset{\leftrightarrow}{T}_{12} \overset{\leftrightarrow}{T}_1 \overset{\leftrightarrow}{T}_{21} \begin{pmatrix} E_1^+ \\ E_1^- \end{pmatrix} = \overset{\leftrightarrow}{T}_u \begin{pmatrix} E_1^+ \\ E_1^- \end{pmatrix}, \quad (2.40)$$

where matrices with one subscript describes propagation in that particular medium, matrices with two subscripts describe reflection and transmission at an interface and subscript u means unit cell. From the unit cell matrix it is possible to construct a matrix describing a structure consisting of K unit cells given by

$$\overset{\leftrightarrow}{T}_s = \overset{\leftrightarrow}{T}_u^K = \begin{pmatrix} T_{11} & T_{12} \\ T_{21} & T_{22} \end{pmatrix}, \quad (2.41)$$

where the subscript s means structure. All the information about the structure is built into the structure matrix $\overset{\leftrightarrow}{T}_s$ including all the multiple reflections, and it only depends on the number of unit cells, the thicknesses and refractive indices of the materials.

It is noticed that the determinants of the matrices in Eq. (2.34) and (2.37) both equal 1, hence the determinant of $\overset{\leftrightarrow}{T}_s$ also equals 1. As explained earlier every layer of the beamsplitter contains a wave propagating forth and back, but the boundary conditions require that there is no wave propagating back after passage of the entire beamsplitter as illustrated in Fig. 2.7. After passage of the entire beamsplitter the field is given by

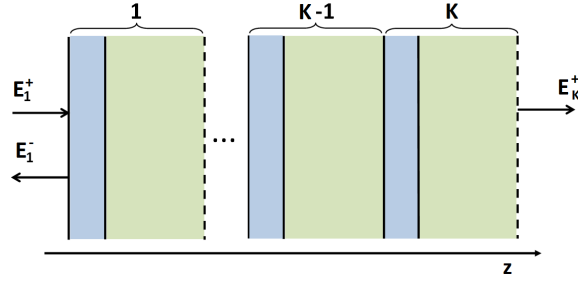


Figure 2.7: Beamsplitter consisting of K unit cells. To the right of the beamsplitter there is no light propagating back. Figure from [23].

$$\begin{pmatrix} E_K^+ \\ E_K^- \end{pmatrix} = \begin{pmatrix} E_K^+ \\ 0 \end{pmatrix} = \begin{pmatrix} T_{11} & T_{12} \\ T_{21} & T_{22} \end{pmatrix} \begin{pmatrix} E_1^+ \\ E_1^- \end{pmatrix} \quad (2.42)$$

Utilizing that the determinant of the structure matrix is 1 it can be shown that the reflectance $R = |\rho|^2$ and transmittance $T = |\tau|^2$ are given by

$$R = \left| \frac{T_{21}}{T_{22}} \right|^2; \quad T = \frac{1}{|T_{22}|^2}. \quad (2.43)$$

According to [17] the incident field is given in terms of the transmitted field through the entire structure, which with the same boundary conditions as in Fig. 2.7 yields

$$\begin{pmatrix} E_1^+ \\ E_1^- \end{pmatrix} = \begin{pmatrix} S_{11} & S_{12} \\ S_{21} & S_{22} \end{pmatrix} \begin{pmatrix} E_K^+ \\ 0 \end{pmatrix}. \quad (2.44)$$

When $\overset{\leftrightarrow}{S}_1 = \overset{\leftrightarrow}{T}_1^{-1}$, $\overset{\leftrightarrow}{S}_2 = \overset{\leftrightarrow}{T}_2^{-1}$ and $\overset{\leftrightarrow}{S}_{ij} = \overset{\leftrightarrow}{T}_{ij}^{-1}$ for every matrix in the structure, then $\overset{\leftrightarrow}{S}_s = \overset{\leftrightarrow}{T}_s^{-1}$ for the entire structure as well and the determinant of $\overset{\leftrightarrow}{S}_s$ also equals 1. Hence

$$\overset{\leftrightarrow}{S}_s = \begin{pmatrix} S_{11} & S_{12} \\ S_{21} & S_{22} \end{pmatrix} = \begin{pmatrix} T_{22} & -T_{12} \\ -T_{21} & T_{11} \end{pmatrix}. \quad (2.45)$$

Combining Eq. (2.44) and (2.45) it can be shown that the reflectance and transmittance are given by

$$R = \left| \frac{S_{21}}{S_{11}} \right|^2 = \left| \frac{T_{21}}{T_{22}} \right|^2; \quad T = \frac{1}{|S_{11}|^2} = \frac{1}{|T_{22}|^2}. \quad (2.46)$$

This is the same as the reflectance and transmittance in Eq. (2.43) showing that the two procedures of the transfer matrix method give the same results.

With the transfer matrix method derived it is possible to calculate the transmittance through the beamsplitter. [17]

2.4.1 Reciprocity

In this subsection the reciprocity principle is explained briefly.

Lorentz' reciprocity theorem states that the electric field at right of a structure when light is incident from left is equivalent to the field at left of the structure when light is incident from right. [25] The principle of the theorem is illustrated in Fig. 2.8 where situation 1 considers light incident from left and observation at right and opposite in situation 2.

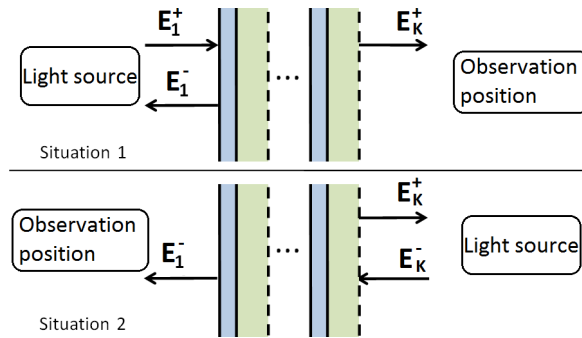


Figure 2.8: Lorentz' reciprocity theorem states that the electric field at the right of a structure when light is incident from left is equivalent to the field at left of the structure when light is incident from right. Hence the two situations in the figure are equivalent. Figure from [23].

The light that passes through the entire beamsplitter is determined by the transmittance $T = 1/|T_{22}|^2$. Hence the transmittance must be the same as if light was incident from right. This is not the case for the reflected field due to possible absorption in the beamsplitter. When at least one of the refractive indices have a non-zero imaginary part a portion of the incident field is absorbed. The orientation of the beamsplitter has an impact on the reflectance and absorbance, because there is difference between whether the light is reflected or absorbed first as illustrated in Fig. 2.9. Here a simple structure consisting of a metal film deposited on glass is considered, and the orientation of the structure is studied where it is assumed that absorption only occurs in the metal. The transmittance is shown by the horizontal arrow and the reflectance by the vertical arrow. The transmittance is independent of the orientation while the left figure has the highest reflectance. [19]

In section 7.4 it will be shown that the reciprocity principle is valid for the optimized beamsplitter and the optimal orientation of it will be found.

2.5. The Admittance Transfer Matrix Method

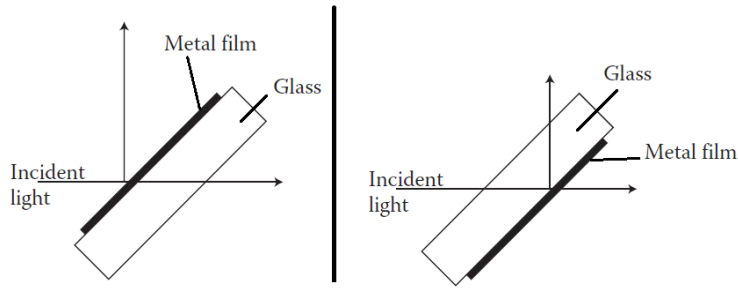


Figure 2.9: A simple structure consisting of a metal film deposited on glass where it is assumed that absorption only takes place in the metal. Light is incident from left in both cases but the structure is reversed. The transmittance is the same in both cases but the reflectance is higher in the left figure where the light enters the metal before the glass. Figure from [19].

2.5 The Admittance Transfer Matrix Method

In this section another transfer matrix method based on admittance is studied. The method in Sec. 2.4 considers only the electric field of the light but treats both its normal and tangential components. The admittance method studied in this section considers both the electric and magnetic field of the light but treats only the tangential components of the fields denoted \mathcal{E} and \mathcal{H} . Hence both methods study two kinds of fields and are thereby equivalent, but the advantage of the admittance method is that according to Eq. (2.11) the tangential components of the fields are conserved across an interface. Hence propagation matrices corresponding to Eq. (2.34) are the only building blocks in the admittance method, and it is therefore expected that this method is faster computationally than the electric field transfer matrix method. Whether this is the case will be investigated in Sec. 6.2. In this section light is always incident from left.

The optical admittance is defined by

$$\eta = \frac{\mathcal{H}}{\mathcal{E}}. \quad (2.47)$$

In free space the admittance is $\eta_0 = \sqrt{\varepsilon_0/\mu_0}$ while it is $\eta = n\eta_0$ in a material with refractive index n . Notice that η_0 is the reciprocal of the vacuum impedance $Z_0 = \sqrt{\mu_0/\varepsilon_0}$. Consider p polarized light incident on a material of refractive index n and thickness a as seen in Fig. 2.10. The material is surrounded by air and its interfaces are denoted α and β . As in Sec. 2.4 the electric field of the forward propagating light is denoted \vec{E}^+ and the backward propagating denoted \vec{E}^- . The positive z direction is into the structure which is opposite of [19]. The tangential components of \vec{E}^+ and \vec{E}^- are opposite and are at interface β given by

$$\mathcal{E}_\beta^+ = E^+ \cos \theta', \quad \mathcal{E}_\beta^- = -E^- \cos \theta', \quad (2.48)$$

where E^+ is the magnitude of \vec{E}^+ and similar for E^- , and θ' is the propagation angle in the material as seen in Fig. 2.10 which can be calculated using Snell's law. At every position the electric field consists of a forward and backward propagating wave, thus

$$\mathcal{E}_\beta = \mathcal{E}_\beta^+ + \mathcal{E}_\beta^-. \quad (2.49)$$

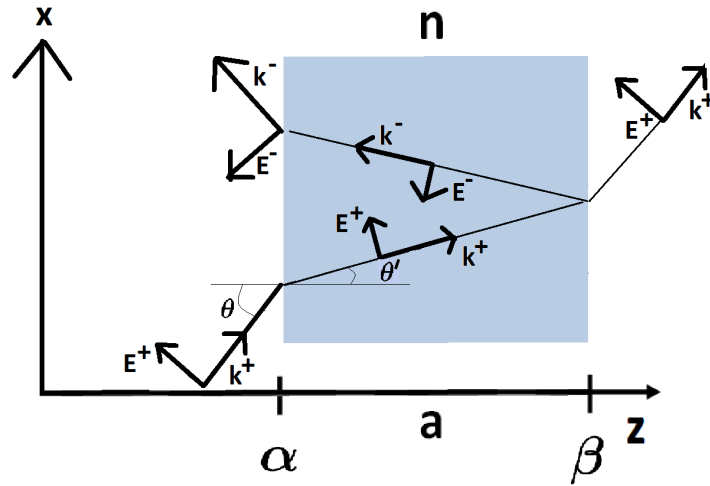


Figure 2.10: Propagation in a medium with refractive index n and thickness a where the interfaces are denoted α and β . The incident light is described by k^+ at left of the layer with E^+ related. The tangential components of the electric fields are calculated along the positive x direction and all magnetic fields point out of the plane. The incident angle is θ while the refracted angle is θ' . Figure inspired by [19].

From Maxwell's equations it is found that $\vec{H} = 1/(\omega\mu_0)\vec{k} \times \vec{E}$ and for p polarization \vec{H} is entirely tangential thus $\mathcal{H} = \vec{H}$. Calculating \mathcal{H} as the sum of the magnetic field for the forward and backward propagating wave yields

$$\mathcal{H} = \frac{k}{\omega\mu_0}(E^+ + E^-) \quad (2.50)$$

where $k = |\vec{k}| = nk_0$. Combining Eq. (2.48) and (2.50) gives the tangential magnetic field at interface β

$$\mathcal{H}_\beta = \frac{k}{\omega\mu_0 \cos \theta'}(\mathcal{E}_\beta^+ - \mathcal{E}_\beta^-). \quad (2.51)$$

Similar can be done for s polarization and the general result is written as

$$\mathcal{H}_\beta = \eta(\mathcal{E}_\beta^+ - \mathcal{E}_\beta^-), \quad (2.52)$$

where the admittance is given by

$$\eta = \begin{cases} k/(\omega\mu_0 \cos \theta') & \text{for p polarization} \\ k \cos \theta'/(\omega\mu_0) & \text{for s polarization.} \end{cases} \quad (2.53)$$

For absorbing media it is convenient to work with wave vectors instead of angles, where $\cos \theta' = k_z/k$ and k_z depends on the incident angle θ from Eq. (2.14). Hence the admittance in Eq. (2.53) is written

$$\eta = \begin{cases} \eta_0 n^2 k_0 / k_z & \text{for p polarization} \\ \eta_0 k_z / k_0 & \text{for s polarization.} \end{cases} \quad (2.54)$$

2.5. The Admittance Transfer Matrix Method

With this way of defining the directions of \vec{E} and \vec{H} the Eqs. (2.49) and (2.52) are the same as obtained in [19] and the remaining part of this section follows the calculations there. Adding and subtracting Eq. (2.49) and (2.52) yields

$$\mathcal{E}_\beta^+ = \frac{1}{2}(\mathcal{H}_\beta/\eta + \mathcal{E}_\beta) \quad (2.55)$$

$$\mathcal{E}_\beta^- = \frac{1}{2}(-\mathcal{H}_\beta/\eta_1 + \mathcal{E}_\beta). \quad (2.56)$$

The fields at α is found in terms of the fields at β by the phase shifts

$$\mathcal{E}_\alpha^+ = \mathcal{E}_\beta^+ e^{-i\delta} \quad (2.57)$$

$$\mathcal{E}_\alpha^- = \mathcal{E}_\beta^- e^{i\delta}, \quad (2.58)$$

where $\delta = k_z a$. At interface α the field can be shown to be

$$\mathcal{E}_\alpha = \mathcal{E}_\alpha^+ + \mathcal{E}_\alpha^- = \mathcal{E}_\beta \cos \delta - \frac{i \sin \delta}{\eta} \mathcal{H}_\beta. \quad (2.59)$$

Analogue calculations can be made for the magnetic field, and in combination with Eq. (2.59) the result is

$$\begin{pmatrix} \mathcal{E}_\alpha \\ \mathcal{H}_\alpha \end{pmatrix} = \overset{\leftrightarrow}{T}_1 \begin{pmatrix} \mathcal{E}_\beta \\ \mathcal{H}_\beta \end{pmatrix}, \quad (2.60)$$

where

$$\overset{\leftrightarrow}{T}_1 = \begin{pmatrix} \cos \delta & -i \sin \delta / \eta \\ -i \eta \sin \delta & \cos \delta \end{pmatrix}. \quad (2.61)$$

The matrix $\overset{\leftrightarrow}{T}_1$ is called the characteristic matrix of the layer and its determinant equals 1. It is found in [19] by changing the sign on δ due to the opposite z direction. It relates the tangential components \mathcal{E} and \mathcal{H} at the incident interface with \mathcal{E} and \mathcal{H} after transmission through the layer. $\overset{\leftrightarrow}{T}_1$ describes propagation in a material with refractive index n and thickness a and corresponds to Eq. (2.34). It serves as the only building block in the admittance method since no interface matrices corresponding to Eq. (2.37) are needed because no changes occur in the tangential components of the fields across an interface. For a beamsplitter consisting of many layers it is easy to generalise the admittance method. The unit cell is the same as in Fig. 2.6 and described by

$$\begin{pmatrix} \mathcal{E}_\alpha \\ \mathcal{H}_\alpha \end{pmatrix} = \overset{\leftrightarrow}{T}_1 \overset{\leftrightarrow}{T}_2 \begin{pmatrix} \mathcal{E}_\gamma \\ \mathcal{H}_\gamma \end{pmatrix} = \overset{\leftrightarrow}{T}_u \begin{pmatrix} \mathcal{E}_\gamma \\ \mathcal{H}_\gamma \end{pmatrix}, \quad (2.62)$$

where γ is the last interface in the unit cell similar to the dotted line in Fig. 2.6. For a beamsplitter consisting of K unit cells the final interface is called Ω and the structure matrix of the beamsplitter is

$$\overset{\leftrightarrow}{T}_s = \overset{\leftrightarrow}{T}_u^K. \quad (2.63)$$

The incident field is given in terms of the final transmitted field $(\mathcal{E}_\Omega, \mathcal{H}_\Omega)$ by

$$\begin{pmatrix} \mathcal{E}_\alpha \\ \mathcal{H}_\alpha \end{pmatrix} = \overset{\leftrightarrow}{T}_s \begin{pmatrix} \mathcal{E}_\Omega \\ \mathcal{H}_\Omega \end{pmatrix}. \quad (2.64)$$

Notice that this is opposite to Sec. 2.4 where the transmitted field was given in terms of the incident field, but as it was also shown in the section the two procedures give the same result. The determinant of $\overset{\leftrightarrow}{T}_s$ equals 1 as it is the product of matrices with determinants of 1. Eq. (2.64) is normalized by dividing by \mathcal{E}_Ω yielding

$$\begin{pmatrix} \mathcal{E}_\alpha/\mathcal{E}_\Omega \\ \mathcal{H}_\alpha/\mathcal{E}_\Omega \end{pmatrix} := \begin{pmatrix} B \\ C \end{pmatrix} = \overset{\leftrightarrow}{T}_s \begin{pmatrix} 1 \\ \eta_0 \end{pmatrix}, \quad (2.65)$$

where η_0 occurs because there is air at right of the structure. Define the input optical admittance by

$$Y = \frac{\mathcal{H}_\alpha}{\mathcal{E}_\alpha}. \quad (2.66)$$

Combining Eqs. (2.65) and (2.66) gives $Y = C/B$ which is calculated from $\overset{\leftrightarrow}{T}_s$ and η_0 . The reflection coefficient for the structure can be shown to be

$$\rho = \frac{\eta_0 - Y}{\eta_0 + Y}, \quad (2.67)$$

where η_0 is the admittance of the incident medium which depends on the polarization according to Eq. (2.54). The reflectance is the absolute square of the coefficient in Eq. (2.67) and yields

$$R = \left| \frac{\eta_0 B - C}{\eta_0 B + C} \right|^2. \quad (2.68)$$

The transmittance and absorbance is calculated in the next subsection. [19]

2.5.1 Transmittance in the Admittance Method

Calculating the transmittance in the admittance method is more complicated than in the electric field method. The intensity of the light described by the Poynting vector is calculated before and after the structure, and the transmittance is the ratio of these intensities. The structure is equivalent to the one in Fig. 2.7 where the first interface is called α and the final interface called Ω .

The Poynting vector is defined as

$$\vec{S} = \vec{E} \times \vec{H}, \quad (2.69)$$

and describes an energy flux density where the fields are entire fields, not the tangential parts. Often the time averaged energy flux density is more interesting and for time harmonic fields its mean value is

$$\langle \vec{S} \rangle = \frac{1}{2} \text{Re}(\vec{E} \times \vec{H}^*), \quad (2.70)$$

where $*$ denotes complex conjugated. The intensity of light flowing into a volume V is an integral of the normal component of the time averaged Poynting vector over the boundary of V .

$$I = \int_{\delta V} \langle \vec{S} \rangle \cdot \hat{n} \, dA, \quad (2.71)$$

where \hat{n} is a normal vector and dA is an area element at the boundary of V . [25] The intensity of the incident light is calculated as the integral in Eq. (2.71) over the

2.6. Structure Matrices for the Beamsplitter

interface α in Fig. 2.10. Similar the intensity of the transmitted light is calculated at the final interface called Ω . At the first interface \vec{E} and \vec{H} are the forward propagating waves and $\hat{n} = -\hat{z}$, hence

$$\langle \vec{S}_\alpha \rangle \cdot \hat{n} = \frac{1}{2} \text{Re}(E_\alpha^+ H_\alpha^{+*} \cos \theta') = \frac{1}{2} \text{Re}(\mathcal{E}_\alpha^+ \mathcal{H}_\alpha^{+*}), \quad (2.72)$$

where \mathcal{E}_α and \mathcal{H}_α are the tangential parts as earlier. The fields at interface α is given in terms of the fields at Ω from Eq. (2.65), thus $\mathcal{E}_\alpha = B\mathcal{E}_\Omega$ and $\mathcal{H}_\alpha = C\mathcal{E}_\Omega$. Inserting $\mathcal{E}_\alpha^+ = 1/2(\mathcal{E}_\alpha + \mathcal{H}_\alpha/\eta_0)$ and $\mathcal{H}_\alpha = \eta_0\mathcal{E}_\alpha$ gives

$$\langle \vec{S}_\alpha \rangle \cdot \hat{n} = \frac{1}{8\eta_0} |\mathcal{E}_\Omega|^2 |\eta_0 B + C|^2, \quad (2.73)$$

where η_0 is the admittance of air as it is the material left of the structure. At interface Ω the intensity is

$$\langle \vec{S}_\Omega \rangle \cdot \hat{n} = \frac{1}{2} \text{Re}(\mathcal{E}_\Omega \mathcal{H}_\Omega) = \frac{1}{2} \text{Re}(\eta_{air}) |\mathcal{E}_\Omega|^2. \quad (2.74)$$

The intensities are found by integrating Eq. (2.73) and (2.74) over the interfaces along x in Fig. 2.10. The structure is considered infinite in the x direction and none of the integrands depend on x . The ratio of the intensities is therefore the same as the ratio of Eq. (2.73) and (2.74), thus giving the transmittance

$$T = \frac{4\eta_0 \text{Re}(\eta_{air})}{|\eta_0 B + C|^2}. \quad (2.75)$$

The absorbance is $A = 1 - R - T$ and applying R and T in Eq. (2.68) and (2.75) gives

$$A = \frac{4\eta_0 \text{Re}(BC^* - \eta_{air})}{|\eta_0 B + C|^2}. \quad (2.76)$$

In Eq. (2.75) and (2.76) η_0 and η_{air} are the same because there is air on both sides of the structure. If the structure is placed on a substrate, replace η_{air} by $\eta_{substrate}$.

It is now possible to calculate the reflectance, transmittance and absorbance using the admittance method. [19]

2.6 Structure Matrices for the Beamsplitter

In this section the structure matrices for the considered beamsplitter are found.

In both transfer matrix methods studied so far the structure consisted of two alternating materials with air on both sides. When fabricating the beamsplitter the layers have to be deposited on glass. The material Si_3N_4 has a higher refractive index than SiO_2 , why it is suggested to put SiO_2 on both sides of the crystal. Furthermore MgF_2 has a lower real part of the refractive index than SiO_2 , and to reduce the reflectance into the structure the outermost layer is MgF_2 . A structure consisting of 3 unit cells is illustrated in Fig. 2.11. The electric field transfer matrix method considers the transmitted field in terms of the incident field, hence the matrices have to multiplied from right to left in the figure giving the structure matrix

$$\overleftrightarrow{T}_s = \overleftrightarrow{T}_{g,a} \overleftrightarrow{T}_g \overleftrightarrow{T}_g \overleftrightarrow{T}_{2g} \overleftrightarrow{T}_u \overleftrightarrow{T}_u^{K-1} \overleftrightarrow{T}_2 \overleftrightarrow{T}_{32} \overleftrightarrow{T}_3 \overleftrightarrow{T}_{a,3}, \quad (2.77)$$

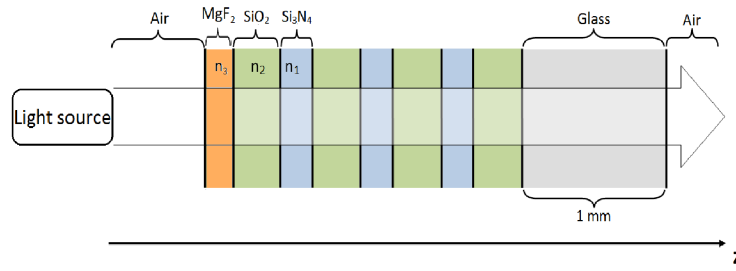


Figure 2.11: Beamsplitter consisting of 3 unit cells with an extra front layer of MgF_2 and extra rear layer of SiO_2 deposited on glass. Figure inspired by [23].

where g is glass and a is air and matrices like \overleftrightarrow{T}_j is propagation in material j described by Eq. (2.34), and matrices like $\overleftrightarrow{T}_{ij}$ describe interfaces between material i and j described by Eq. (2.37), and the unit cell matrix \overleftrightarrow{T}_u is given in Eq. (2.40).

The admittance transfer matrix method considers the incident field in terms of the transmitted field, hence the matrices have to be multiplied from left to right in the figure giving the structure matrix

$$\overleftrightarrow{T}_s = \overleftrightarrow{T}_3 \overleftrightarrow{T}_2 \overleftrightarrow{T}_u^K \overleftrightarrow{T}_g, \quad (2.78)$$

where the propagation matrices \overleftrightarrow{T}_j are given in Eq. (2.61) and the unit cell matrix in Eq. (2.62).

The structure matrix looks simpler for the admittance method but its building blocks are more complicated than the electric field method. In addition the expressions for the reflectance and transmittance in Eq. (2.68) and (2.75) for the admittance are also more complicated compared to Eq. (2.43). The two methods are equivalent but maybe one is faster computationally which will be investigated in section 6.2.

2.7 Band Gaps described by the Transfer Matrix Methods

In this section it will be shown how to find the band gaps using one of the transfer matrix methods, and that the methods give the same result as found in Sec. 2.3 where an infinite beamsplitter was studied.

As mentioned earlier a band gap is characterized by that no light can propagate at that frequency, which means that the transmittance is zero. To compare a transfer matrix method with the method of infinite structures a large number of unit cells has to be chosen, which in the calculations is set to $K = 1000$. Hence a beamsplitter with the same dimensions and refractive indices as in Fig. 2.3 is considered consisting of 1000 unit cells. The transmittance is calculated using Eq. (2.43) or Eq. (2.75), depending on which transfer matrix method to apply for every frequency in some region and is plotted in Fig. 2.12a for $\theta = 0^\circ$ and Fig. 2.12b for $\theta = 45^\circ$. It is seen in both figures that there are four band gaps and they are seen to occur at the same frequencies as in the dispersion relations in Fig. 2.3. Hence it is shown that the two methods give the same result. Notice that the band gaps occur at higher frequencies when the incident angle is 45° compared to 0° , which was also seen in the dispersion relations in Fig. 2.3. The fact that the position of the band gaps depend on the incident angle will further be explained and utilized in Sec. 7.1.2, where the angular dependence of the total efficiency of the hybrid system is studied in detail.

2.7. Band Gaps described by the Transfer Matrix Methods

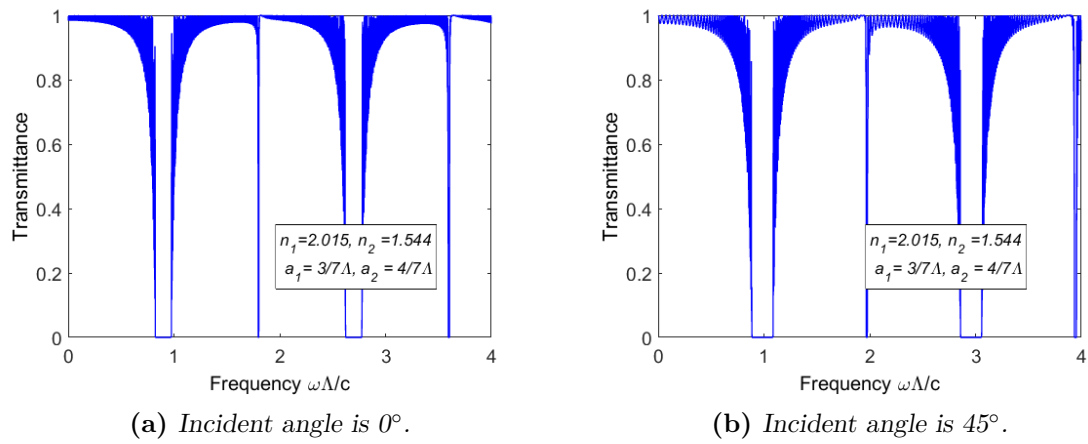


Figure 2.12: Transmittances for incident angles of 0° and 45° . Notice that the band gaps occur at higher frequency for 45° in correspondence with Fig. 2.3.

3. Efficiency of Solar Cells

In this chapter the basic ideas behind solar cells are explained and expressions for the efficiency are derived. First this is done for an ideal solar cell without any losses and a theoretical limit for its efficiency is found. Afterwards limiting factors are introduced and the efficiency found for more realistic solar cells and this efficiency is much less than the theoretical limit. In the Matlab implementation in Chapter 6 first the efficiency of an ideal solar cell is used, and the optimization processes are tested on this. Later in Sec. 7.2 and 7.3 the efficiencies of more realistic solar cells are applied in the optimization process and it is studied how much the efficiency of the hybrid system exceeds that of a single solar cell.

3.1 Efficiency of an Ideal Solar Cell

In this section an ideal solar cell without any losses is described and its efficiency derived. A solar cell is basically an electronic device that converts sunlight into electricity. When sunlight is incident on a solar cell it gives rise to a current and a voltage thus generating an output power. A solar cell is illustrated in Fig. 3.1 and consists of several parts to be described. The front layer is antireflection coating which reduces the reflection from air into the solar cell. For a solar cell of silicon with a refractive index of 3.4 the reflectance from air for light incident perpendicular is approximately 30%. If glass with refractive index 1.5 is deposited on top of the silicon, the reflectance from air into the silicon can be reduced to approximately 18% depending on the glass thickness.

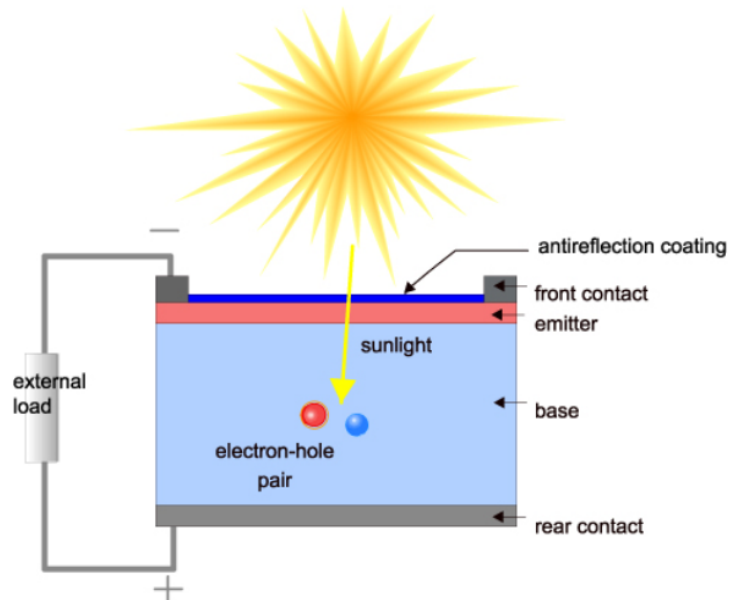


Figure 3.1: Illustration of a solar cell. The antireflection coating reduces reflection from air into the solar cell. The emitter layer consists of an n -doped semiconductor and the base layer of a p -doped semiconductor, hence the interface between emitter and base is a pn junction. Electron-hole pairs are generated in the depletion layer of the pn junction and the electrons dissipate their power in the external load. Figure from [11]

If a material with refractive index $\sqrt{1.5 \cdot 3.4} \approx 2.25$ is deposited between the glass and silicon the reflectance is further reduced. [11] In general the reflectance depends strongly on the wavelength, and appropriate thicknesses of the glass and the antireflection layer can further decrease the reflectance in a desired wavelength interval. In [13] antireflection coating is deposited using ZnO, TiO₂ and SiO₂ with refractive indices in the visible region of approximately 2, 2.6 and 1.45, respectively [1]. In the wavelength interval 420-600 nm the reflectance is reduced to approximately 4%, but exceeds 15% for wavelengths above 700 nm. In the case of an ideal solar cell considered here, the reflectance is neglected and it is assumed that all the light is directed into the solar cell.

The next two parts of the solar cell in Fig. 3.1 are the emitter and base layers. The emitter is an n -doped semiconductor while the base is the same semiconductor that is p -doped, and the interface between the two layers forms a pn junction. When brought together electrons diffuse from the n -doped material into the p -doped while holes diffuse in opposite direction. It is assumed that the diffused electrons from the n -doped material all settle in a layer of width W_p in the p -doped region, where no free electrons are present. Similar the diffused holes form a layer of width W_n with no free holes. Hence an electric field is generated in the direction that prevents the diffusion, and a stationary depletion layer with thickness $W = W_n + W_p$ arises. [28] The doped materials outside the depletion layer contain many free charges, but no electric field is present here. Hence the charges move in random direction with no net motion, thus not contributing to a current in the external loop. The same applies if more electrons are excited into the conduction band in the regions outside the depletion layer. Inside the depletion layer, on the other hand, there are no free charges but an electric field is present. Hence when an electron-hole pair is generated, the presence of the electric field implies that electrons and holes are separated, and that the electrons move in a net direction and generate a current. [11]

The external loop with a load resistance is connected to a front and a rear contact, and when a voltage is present the electrons in the loop dissipate a power in the load resistance, thereby lowering their energy and entering the solar cell again in the emitter layer. The design of the front contacts has an impact on the efficiency, as the metal contact reflects almost all the light in the interesting wavelength interval. Hence a large contact overshadows a part of the solar cell, reducing the amount of photons to be absorbed. On the other hand, a small contact implies a high series resistance of the front electrode, and the design of the contact is a balance between these two competing factors. If the solar cell has area A_{tot} and the contact has area A_c the coverage factor is $1 - A_c/A_{tot}$ and contributes to a reduction of the efficiency. When assuming that the solar cell is ideal the area of the contact is neglected and the coverage factor equals 1. [34]

The generation of an electron-hole pair requires the absorption of a photon, whose energy is at least E_g which is the band gap energy of the semiconductor. If the photon energy is less than E_g it cannot be absorbed and is just transmitted through the entire solar cell without any contribution to the power generation and thereby efficiency. If the energy of the photon is equal to E_g it is absorbed and an electron is excited from the top of the valence band into the bottom of the conduction band, thus utilizing all the energy of the photon. When the photon has an energy higher than the band gap, it is still absorbed but the electron is excited to a higher state in the conduction band, from where it loses its excess energy to heat and falls down to the conduction band edge. Hence the usable energy is the band gap energy and the ideal efficiency η_{ideal} , as a function of the photon

3.1. Efficiency of an Ideal Solar Cell

energy can be expressed as [28]

$$\eta_{\text{ideal}}(E) = \begin{cases} 0 & \text{for } E < E_g \\ E_g/E & \text{for } E \geq E_g, \end{cases} \quad (3.1)$$

or equivalently as a function of wavelength as $E = hc/\lambda$

$$\eta_{\text{ideal}}(\lambda) = \begin{cases} 0 & \text{for } \lambda > \lambda_g \\ \lambda/\lambda_g & \text{for } \lambda \leq \lambda_g, \end{cases} \quad (3.2)$$

where λ_g is the band gap wavelength.

3.1.1 The Solar Spectrum

In this subsection the solar spectrum is presented.

The sun can be approximated as a black body with surface temperature 5800 K, whose energy density is given by the Planck distribution [27]

$$u(\omega) = \frac{\hbar}{\pi^2 c^3} \frac{\omega^3}{e^{\hbar\omega/kT} - 1}, \quad (3.3)$$

where \hbar is the reduced Planck's constant and k is Boltzmann's constant. Eq. (3.3) gives the energy density outside the atmosphere of the Earth and this spectrum is called AM0. A part of the radiation is absorbed by the atmosphere, where ozone and oxygen absorb radiation in the UV region and gasses like CO₂, N₂O and CH₄ absorb radiation in the IR region and the absorption depends on the thickness of the atmosphere and the incident angle. The spectrum on the surface of the Earth for normal incidence is called AM1, and for moderate climates where the incident angle is about 48° the spectrum is called AM1.5. [32] The spectrum as a function of wavelength instead of energy is called $F(\lambda)$ and is shown in Fig. 3.2 from [8] where the irradiance is given in a wavelength interval from 280-4000 nm. At wavelengths above 2500 nm the irradiance is negligible, therefore only wavelengths from 280-2500 nm will be considered in this thesis. The irradiance decreases

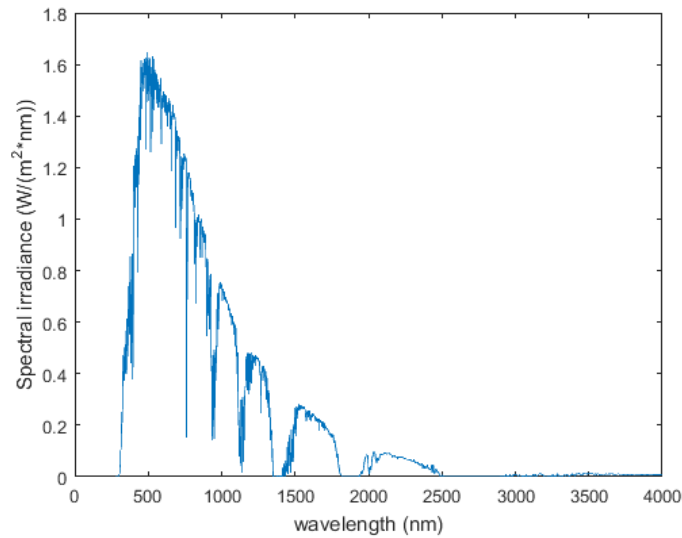


Figure 3.2: AM1.5 Solar spectrum. The irradiance decreases at some wavelengths due to absorption in the atmosphere of the Earth. Figure from [8].

at some wavelengths caused by absorption in the atmosphere. Integrating the irradiance from 280-2500 nm gives an intensity of 992 W/m^2 , which is the incident intensity from the sun onto the earth, but unfortunately not all this intensity can be utilized by solar cells. As explained in the previous section, the band gap equals the usable energy, and if it is too large only a small fraction of the solar spectrum can be utilized. On the other hand, if the band gap is too small much of the solar spectrum can be utilized but the usable energy for all the wavelengths is small. The efficiency as a function of the band gap energy for an ideal solar cell is seen in Fig. 3.3 for both the Planck distribution and the measured AM1.5 solar spectrum. The maximal efficiency is found to be approximately 48% for a band gap around 1.1 eV, which is almost the same as the value in silicon. The ideal efficiency as a function of wavelength was given in Eq. (3.2), and the overall efficiency for an ideal solar cell is found by integrating this efficiency weighted with the solar spectrum in Fig. 3.2, yielding

$$\eta_{\text{ideal}} = \frac{\int_{280}^{\lambda_g} F(\lambda) \lambda / \lambda_g d\lambda}{\int_{280}^{2500} F(\lambda) d\lambda}. \quad (3.4)$$

The utilized intensity is the numerator in Eq. (3.4) which for a band gap wavelength of 900 nm is found to be 464 W/m^2 , and when the denominator was 992 W/m^2 the efficiency of the ideal solar cell becomes 46.76%. Same number can be found from Fig. 3.3 when it is used that a band gap wavelength of 900 nm gives a band gap of 1.49 eV.

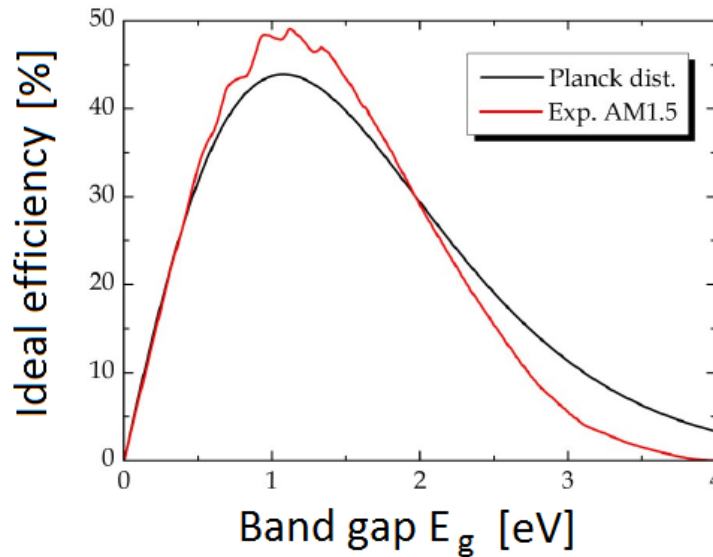


Figure 3.3: Efficiency for an ideal solar cell as a function of the band gap energy. The black line is for the Planck distribution while the red line is for the measured AM 1.5 solar spectrum. Figure from [28]

3.2 Efficiency of a Solar Cell with Limiting Factors

While the previous section considered the efficiency of an ideal solar cell, this section takes into account several limiting factors that reduce the efficiency to a more realistic level.

3.2.1 Quantum Efficiencies

In this subsection the external quantum efficiency is introduced as a limiting factor. To have a more realistic expression for the solar cell efficiency it is no longer assumed that

3.2. Efficiency of a Solar Cell with Limiting Factors

all the photons with an energy larger than E_g are absorbed. Due to a limited thickness of the solar cell, some photons travel through the entire cell without being absorbed. This incomplete absorption can be described by an internal optical quantum efficiency IQE_{op} , describing the probability that an incident photon is absorbed somewhere in the solar cell, and of course this probability is zero if the photon energy is less than the band gap energy. When a photon is absorbed in the solar cell it generates an electron-hole pair, but in itself this does not contribute to a current. For if the electron-hole pair is generated outside the depletion layer where no electric field is present, they will recombine with no contribution to the current. The internal electrical quantum efficiency IQE_{el} is the probability that an electron excited by a photon is collected and contributes to the current. The product $\text{IQE} = \text{IQE}_{op} \cdot \text{IQE}_{el}$ is the internal quantum efficiency and describes the probability that a photon is absorbed and the excited electron contributes to the current. [34]

As mentioned in Sec. 3.1 reflection from air into the solar cell occurs, and also from the interfaces inside the solar cell and from its back side. Collecting all these reflections in a total reflectance R and taking the coverage factor into account the external quantum efficiency $\text{EQE} = (1 - R)(1 - A_c/A_{tot})\text{IQE}$ gives the probability that a photon incident on a solar cell is absorbed and the excited electron is collected, and is seen in Fig. 3.4 as a function of wavelength. For an ideal solar cell all the incident photons with an energy above the band gap are utilized, thus the EQE is unity for wavelengths below λ_g and zero otherwise as illustrated by the brown curve in the figure. For a real solar cell of e.g silicon the imaginary part of the refractive index is higher for the short wavelengths and zero for wavelengths above approximately 1100 nm [1]. Hence the material absorbs much light for the short wavelengths, but the absorption mostly takes place in the front layer of the cell where the light first enters. In that region the electrons are not properly collected, implying that the EQE is low for the short wavelengths. For the long wavelengths only a small part of the photons are absorbed in the solar cell due to its limited thickness, implying that the EQE is also low for the long wavelengths. [11]

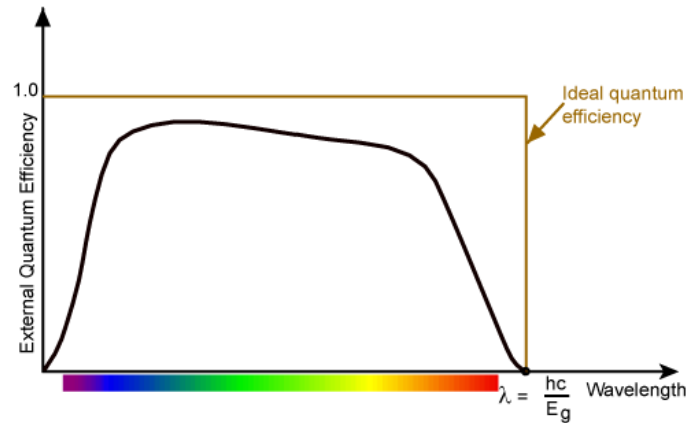


Figure 3.4: The external quantum efficiency describes the probability that an incident photon is absorbed and the excited electron collected. For the short wavelengths most of the photons are absorbed in the front layer where the excited electrons are not collected, why EQE is low in that wavelength region. For the long wavelengths the imaginary part of the refractive index is low, thus few photons are absorbed implying that EQE is also low for the long wavelengths. Figure from [11]

3.2.2 The Fill Factor

In this subsection the fill factor is explained.

As explained in Sec. 3.1 the solar cell contains a pn junction, where an electric field exists in the depletion layer. When photons are absorbed in that layer a photocurrent density J_L is produced in the reverse-bias direction. The forward-bias voltage V in the external loop creates a current density J_F in the opposite direction of J_L . The net current density in the reverse-bias direction is then

$$J(V) = J_L - J_F = J_L - J_0 \left(e^{eV/kT} - 1 \right), \quad (3.5)$$

where it has been assumed that the pn junction satisfies the ideal diode equation and where J_0 is a constant related to the electric properties of the materials. The J-V characteristic is seen as the red curve in Fig. 3.5, and two limiting cases are of special interest. The short circuit current density J_{sc} is the maximal current density in the loop and occurs when no voltage is applied corresponding to a circuit with no resistance. On the other hand, if the resistance goes to infinity the circuit is open, there is no current and the voltage is the open circuit voltage V_{oc} found by setting $J(V) = 0$ in Eq. (3.5) and solve for V [22]

$$V_{oc} = \frac{kT}{e} \ln \left(1 + \frac{J_L}{J_0} \right). \quad (3.6)$$

For crystalline solar cells the maximal short circuit current density is 46mA/cm² and the open circuit voltage is up to 720mV, while it is about 17mA/cm² and 850mV for amorphous solar cells. [13] and [34]

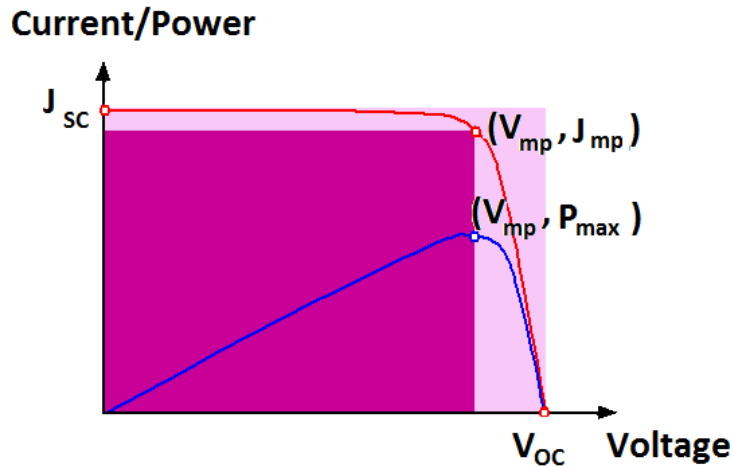


Figure 3.5: *J-V characteristic for a solar cell shown as the red curve and generated power as the blue curve. The maximal generated power is the purple area which equals the fill factor times the lighter purple area. Figure from [11].*

In both these two limiting cases no power P is generated as it is the product of current and voltage. The power is seen as the blue curve in Fig. 3.5 and has a maximum P_{max} when the voltage is V_{mp} , which cannot be expressed as a simple analytic expression. The current density corresponding to that voltage is J_{mp} and the maximum power is the purple area in the figure, which is expressed by the fill factor FF defined by

$$FF = \frac{J_{mp} V_{mp}}{J_{sc} V_{oc}}, \quad (3.7)$$

3.2. Efficiency of a Solar Cell with Limiting Factors

expressing the ratio between the purple area and the lighter purple area, and the value of the fill factor is typical between 0.7 and 0.8, while it equals 1 in the ideal case. [22]

With all these limiting factors explained the solar cell efficiency as function of wavelength can be found as the utilized intensity divided by the incident intensity

$$\eta_{\text{solar}}(\lambda) = \frac{I(\lambda)}{I_{\text{incident}}(\lambda)} = \eta_{\text{ideal}}(\lambda)EQE(\lambda)FF, \quad (3.8)$$

where $\eta_{\text{ideal}}(\lambda)$ is the efficiency from Eq. (3.2) and $EQE(\lambda)$ is the wavelength dependent external quantum efficiency from Fig. 3.4. In Sec. 7.1 and 7.2 the efficiency as a function of wavelength will be shown for an amorphous and microcrystalline solar cell.

Like in the ideal case in Sec. 3.1.1 the total utilized intensity is found by integrating the efficiency in Eq. (3.8) multiplied by the solar spectrum, and the solar cell efficiency is found by dividing that intensity with the incident intensity, yielding

$$\eta_{\text{solar}} = \frac{FF \int_{280}^{\lambda_g} F(\lambda)EQE(\lambda)\lambda/\lambda_g d\lambda}{\int_{280}^{2500} F(\lambda) d\lambda}. \quad (3.9)$$

The only difference between this efficiency and the ideal one in Eq. (3.4) are the factors $EQE(\lambda)$ and FF in the numerator of Eq. (3.9), where FF does not depend on wavelength and therefore are outside the integral. As seen in Fig. 3.4 the EQE in the ideal case is 1 in the entire interval and FF also equals 1 in the ideal case. Hence the ideal efficiency in Eq. (3.4) is just a special case of the solar cell efficiency in Eq. (3.9).

4. Efficiency of Thermoelectric Elements

In this chapter primarily based on [10] the basic concepts of thermoelectricity will be introduced and an expression for the efficiency of the thermoelectric element derived. First two thermoelectric effects will be described and the relations between them explained. These effects are the foundations of thermoelectric refrigerators and heat pumps, where energy is put into the system to achieve a temperature difference. The reverse effect is found in thermoelectric generators where energy is extracted from the system when a temperature difference is present, and such a device is used as the thermoelectric element in the hybrid system. Lastly an expression for the efficiency of the hybrid system is presented as a combination of the thermoelectric efficiency derived in this chapter and the solar cell efficiency derived in the previous chapter.

4.1 Thermoelectric effects

The first thermoelectric effect was discovered by Seebeck in 1821. To demonstrate the effect two different electric conductors are used which are assumed to be isotropic. They are put together to form a junction in one end, while the other ends of the conductors are connected to a galvanometer as seen in Fig. 4.1, and they are said to form a thermocouple with the conductors as its legs. Seebeck found that heating the junction results in an

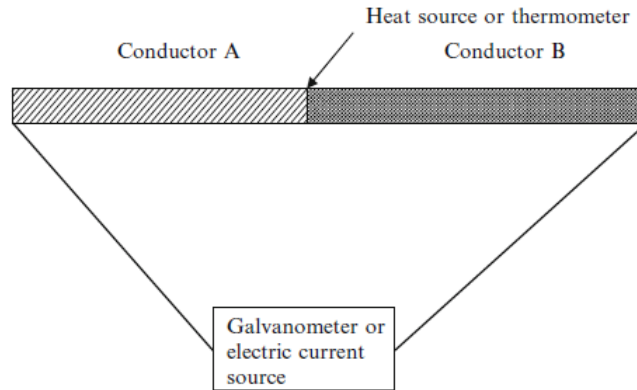


Figure 4.1: *Experimental setup to demonstrate the Seebeck and Peltier effects. To demonstrate the Seebeck effect a heat source and a galvanometer is used, while using a thermometer and an electric current source shows the Peltier effect. Figure from [10].*

electromotive force V which is proportional to the temperature difference ΔT between the junction and the galvanometer. The proportionality constant is the Seebeck coefficient defined by

$$\alpha_{AB} = \frac{V}{\Delta T}, \quad (4.1)$$

with unit V/K . It is positive if the electromotive force causes a current to flow through conductor A from the hot junction to the galvanometer, i.e in clockwise direction in the circuit. In general the Seebeck coefficient can have a strong temperature dependence, and it is furthermore noticed that the Seebeck coefficient is only defined for a pair of materials.

The Seebeck effect can be explained quantum mechanically where an electric current consists of moving electrons having different energies in different materials. When a junction is heated and the electrons receive thermal energy they are allowed to pass from the material having lowest energy into the high energy material, thus giving rise to an electromotive force. If the two materials are the same, no electromotive force will arise and $\alpha_{AA} = 0$.

The second thermoelectric effect was discovered by Peltier in 1834 and is the reverse of the Seebeck effect. He found that when a current passes through a thermocouple it results in a heating or cooling of the junction, depending on the direction of the current. This is explained by a current that runs through the junction increases or decreases the energy of the electrons, depending on the direction of the current, and this energy change results in heating or cooling. The setup is also seen in Fig. 4.1, where an electric current source and a thermometer is applied. Peltier found that the power, P , of heating or cooling is proportional to the applied current I , where the proportionality constant is the Peltier coefficient defined by

$$\pi_{AB} = \frac{P}{I}, \quad (4.2)$$

with unit V . It is positive if the junction where the current runs into conductor A is heated. Like the Seebeck coefficient, the Peltier coefficient can also depend on the temperature. In practice doped semiconductors are used nowadays in thermoelectric generators because they have larger Peltier coefficients than metals.

Unfortunately it is difficult to measure the Peltier coefficient. This is due to the fact that when a current passes through the thermocouple irreversible Joule heating occurs, where $P = I^2R$ is the power delivered to the thermocouple having resistance R , and typically this Joule heating overshadows the Peltier effect. A way to measure the Peltier coefficient is to measure the change in temperature for both directions of the current. Then it is possible to observe that heating or cooling actually occurs, though overshadowed by the Joule heating.

These two effects describe the relation between heat and electricity. About the same time as Seebeck and Peltier, Danish H.C Ørsted discovered that current passing through an electric conductor generates a magnetic field. Later Faraday discovered the reverse effect, namely that the change of a magnetic field in a coil results in a current which is now known as magnetic induction. These two discoveries began the study of electromagnetism which was later fully described by Maxwells equations. [16] Hence the Seebeck and Peltier effects are the thermoelectric versions of the electromagnetic laws regarding the relations between electric and magnetic fields. To fulfil the relations between heat, electricity and magnetism, the thermomagnetic effects was discovered by Nernst and Ettinghausen, and describe how the thermoelectric effects are affected by the presence of a magnetic field. However, these thermomagnetic effects will not be considered in this thesis.

In 1855 Thomson realized that the Seebeck and Peltier effects are connected and he found the following relation between the Seebeck- and Peltier coefficients

$$\pi_{AB} = \alpha_{AB}T. \quad (4.3)$$

From this relation it is possible to find the Peltier coefficient, which itself is difficult to measure, based on the Seebeck coefficient which is easier to measure.

4.2 Thermoelectric refrigerators

In this section it is shown how the thermoelectric effects introduced in the previous section are applied in the theory of thermoelectric refrigerators. A simple model for a refrigerator is presented and it is shown how to maximize its cooling power. Furthermore, the figure of merit is introduced as a measurable quantity describing the performance of a refrigerator and a thermoelectric generator, and it is shown that a specific geometric design of the thermocouple results in the optimal figure of merit.

The simple model considered here is based on the thermocouple in Fig. 4.2 consisting of n - and p -doped semiconductors as the two legs, which are connected electric in series and thermal in parallel. It only consists of one thermocouple, but it is possible to generalize the theory to a system consisting of multiple thermocouples. The model contains the following assumptions: The only way heat can flow between the heat source and sink is through the thermocouple, and heat can flow freely from the thermocouple into the source and sink, meaning that the gray shaded areas in the figure have no thermal resistance. Hence thermal radiation and losses from heat convection are neglected. Furthermore the two legs have constant cross sectional area A_p and A_n .

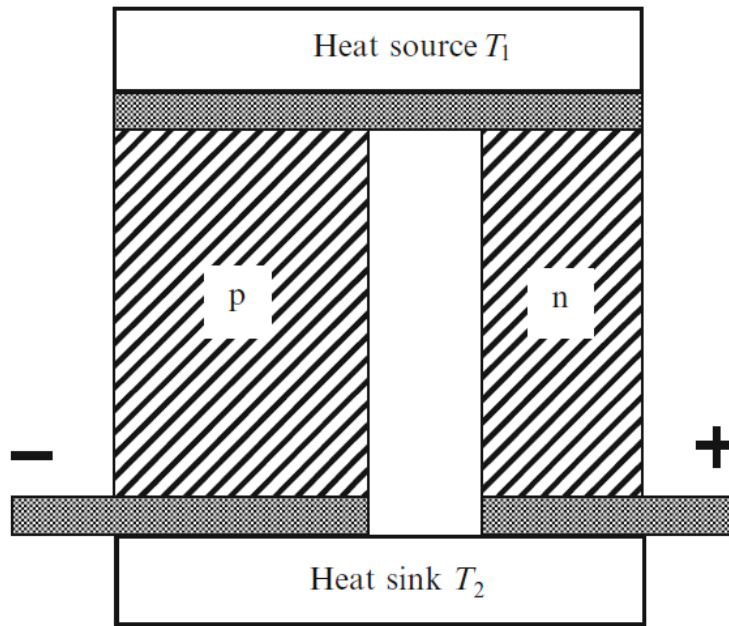


Figure 4.2: Thermoelectric refrigerator consisting of a thermocouple where the two legs are n - and p -doped semiconductors. When a current is applied from $+$ to $-$ heat is extracted from the heat source, thus $T_2 > T_1$. Heat only flows between the source and the sink through the thermocouple, and the gray shaded areas are assumed to have no thermal resistance. Figure from [10].

A current is passing through the thermocouple from $+$ to $-$, which results in Peltier cooling at the heat source and a temperature difference $\Delta T = T_2 - T_1 > 0$. The power of the Peltier cooling at the heat source is $(\alpha_p - \alpha_n)IT_1$, which is found by combining the Eqs. (4.2) and (4.3) where the two thermocouple legs have the Seebeck coefficients $\alpha_p > 0$ and $\alpha_n < 0$. However, the cooling effect is opposed by two heating effects. The first is Joule heating in the thermocouple and occurs with the power $I^2(R_p + R_n)/2$ where R_p and R_n

are the electric resistances of the legs. The factor of one half is because the Joule heating splits up equally into the heat source and heat sink. The second effect is heat conduction from the heat sink to the colder heat source, which occurs with the power $(K_p + K_n)\Delta T$ where K_p and K_n are the thermal conductances of the legs. The total cooling power is then given by

$$P_{\text{cooling}} = (\alpha_p - \alpha_n)IT_1 - I^2(R_p + R_n)/2 - (K_p + K_n)\Delta T. \quad (4.4)$$

The power of electric energy to the refrigerator consists of two terms. The first is $(\alpha_p - \alpha_n)I\Delta T$, which comes from work to overcome the thermoelectric voltage, while the second is pure loss in the resistances, hence the total power of electric energy is given by

$$P_{\text{electric}} = (\alpha_p - \alpha_n)I\Delta T + I^2(R_p + R_n). \quad (4.5)$$

The coefficient of performance (COP) of the refrigerator is the ratio of these two powers

$$\Phi = \frac{P_{\text{cooling}}}{P_{\text{electric}}} = \frac{(\alpha_p - \alpha_n)IT_1 - I^2(R_p + R_n)/2 - (K_p + K_n)\Delta T}{(\alpha_p - \alpha_n)I\Delta T + I^2(R_p + R_n)}. \quad (4.6)$$

The current I that maximizes the cooling power in Eq. (4.4) is of special interest and is studied in the next subsection.

4.2.1 Maximal Cooling Power

In this subsection the maximal cooling power is studied in details.

It is seen in Eq. (4.4) that the cooling power is a second order polynomial in I with negative leading coefficient. Hence the cooling power has a maximum in $I_{\text{max}} = (\alpha_p - \alpha_n)T_1/(R_p + R_n)$. At this current the COP is found to be

$$\Phi' = \Phi|_{I=I_{\text{max}}} = \frac{\frac{1}{2}ZT_1^2 - \Delta T}{ZT_1T_2}, \quad (4.7)$$

where the figure of merit has been introduced as

$$Z = \frac{(\alpha_p - \alpha_n)^2}{(K_p + K_n)(R_p + R_n)}. \quad (4.8)$$

The figure of merit is a measure of the goodness of the refrigerator and is measured in K^{-1} , but often it is convenient to treat as the dimensionless number ZT at some temperature T which often is chosen to be room temperature.

It can be shown that $\frac{\partial \Phi'}{\partial Z} = \frac{\Delta T}{Z^2 T_1} > 0$, hence Φ' is a strictly increasing function of Z . Thus to have a high COP it is preferred to have Z as high as possible, showing why exactly this quantity is a good measure of a refrigerator. The best Φ' is thus found letting $Z \rightarrow \infty$ in Eq. (4.7) giving $\Phi'_{\text{max}} = \frac{T_1}{2T_2}$.

From Z in Eq. (4.8) it is seen that higher absolute values of the Seebeck coefficients results in higher Z , which is in agreement with the Seebeck and Peltier effects considered in Sec. 4.1. If $\alpha_p = \alpha_n = 0$, then $Z = 0$ and there would be no cooling power at all. Another way of maximizing Z is to minimize the denominator $(K_p + K_n)(R_p + R_n)$. The thermal conductance and electric resistance are given by [12]

$$K = \lambda \frac{A}{L}, \quad R = \rho \frac{L}{A}, \quad (4.9)$$

4.3. Thermoelectric Generators

where A and L are the area and length of a thermocouple leg, while λ and ρ are the thermal conductivity and electric resistivity, respectively, which are both material constants. The product in the denominator of Z can then be written as

$$(K_p + K_n)(R_p + R_n) = \lambda_n \rho_p \frac{A_n L_p}{A_p L_n} + \lambda_p \rho_n \frac{A_p L_n}{A_n L_p} + \lambda_p \rho_p + \lambda_n \rho_n \quad (4.10)$$

The last two terms in this expression are constants, but the first two terms contain A and L which can be varied. It is seen that choosing

$$\frac{A_n L_p}{A_p L_n} = \sqrt{\frac{\lambda_p \rho_n}{\lambda_n \rho_p}}, \quad (4.11)$$

leads to the minimal value $(K_p + K_n)(R_p + R_n) = (\sqrt{\lambda_p \rho_p} + \sqrt{\lambda_n \rho_n})^2$, and the maximal Z of

$$Z = \frac{(\alpha_p - \alpha_n)^2}{(\sqrt{\lambda_p \rho_p} + \sqrt{\lambda_n \rho_n})^2}. \quad (4.12)$$

This is normally the value of Z that is meant when discussing the figure of merit for a thermoelectric refrigerator and now it only consists of different material constants. Hence optimizing the figure of merit considers the challenge of finding or fabricating materials with high Seebeck coefficients and small thermal conductivity and electrical resistance at the same time. Today a thermoelectric device is considered as good if $ZT = 1$ at room temperature, but the use of nano-scale micro structures such as high quality 2D quantum superlattice with nano scale thin films based on p-Bi₂Te₃/Sb₂Te₃ having $ZT = 2.4$ at room temperature has been achieved. Another option is a nanostructured material with quantum dots based on PbSeTe where $ZT = 2.0$ has been found as reported in [26] from 2006. Further research in the topic will probably in near future lead to fabricated materials with even better figure of merit.

Hence in practice when building a thermocouple of two materials with known conductivities and resistivities, the dimensions of the thermocouple legs must be in agreement with Eq. (4.11) in order to best exploit the thermocouple. A simple practical idea could be to make the two legs of the same length, then the ratio of the areas is the only variable to match with the optimal value.

4.3 Thermoelectric Generators

In the preceding section a refrigerator model was considered and it was shown how to gain a cooling power when a current was applied. In this section a thermoelectric generator is considered where the idea is to achieve an output power when a temperature difference is present. A heat source and sink are kept at different temperatures and the Seebeck effect generates an electromotive force, which makes it possible to gain electric energy from the generator. The efficiency of the generator will be found which again depends on the figure of merit.

The model of a thermoelectric generator is seen in Fig. 4.3. The upper part looks similar to the refrigerator in Fig. 4.2, but now instead of applying a current to cool the heat source, the thermocouple is connected to a variable load resistance R_L . The heat source is warmed by an external source like the sun or waste heat from machines, while the heat sink is kept at a lower temperature. Notice that it is the opposite case compared to the refrigerator.

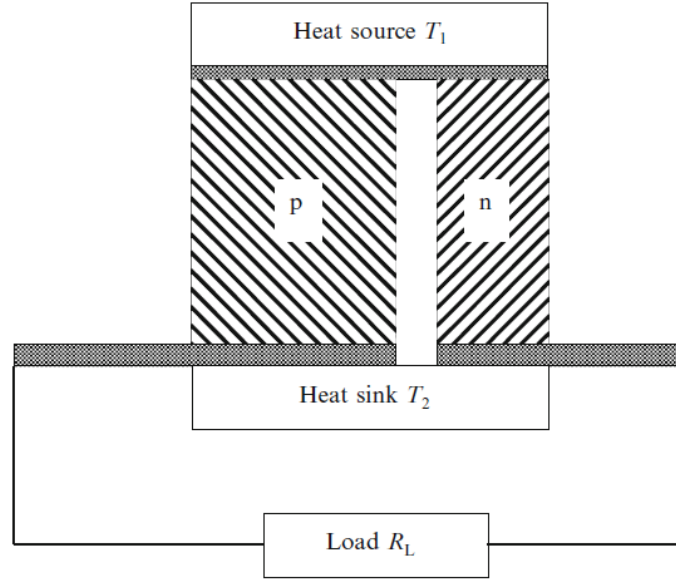


Figure 4.3: Thermoelectric generator consisting of a thermocouple connected to a variable load resistance R_L . The heat source is warmed, while the heat sink is kept at a lower temperature, thus $T_1 > T_2$. Figure from [10].

Hence a temperature difference $\Delta T = T_1 - T_2 > 0$ is present, resulting in an electromotive force $V = (\alpha_p - \alpha_n)\Delta T$ from Eq. (4.1). The total resistance in the circuit is $R_p + R_n + R_L$, which results in the current and power delivered in the load given by

$$I = \frac{(\alpha_p - \alpha_n)\Delta T}{R_p + R_n + R_L}, \quad (4.13)$$

$$P_{\text{load}} = I^2 R_L = \left(\frac{(\alpha_p - \alpha_n)\Delta T}{R_p + R_n + R_L} \right)^2 R_L. \quad (4.14)$$

It can be shown that this power is highest when $R_L = R_p + R_n$, hence only half of the total power is delivered to the load, the other half being delivered in the thermocouple resistances.

To calculate the efficiency of the thermoelectric generator, it is also necessary to know the value of the heat extracted from the heat source. As explained in Sec. 4.2 the current in the circuit gives rise to Peltier cooling at the heat source with the power $(\alpha_p - \alpha_n)IT_1$, hence first heat needs to be extracted from the source in order to balance this cooling. In addition there is thermal conduction from the hot heat source to the colder sink, which occurs with the power $(K_p + K_n)\Delta T$. Hence the total extracted heat from the source is

$$P_{\text{extracted}} = (\alpha_p - \alpha_n)IT_1 + (K_p + K_n)\Delta T. \quad (4.15)$$

The efficiency of the thermoelectric generator is the ratio of these two powers

$$\eta_{TE} = \frac{P_{\text{load}}}{P_{\text{extracted}}} = \frac{\left(\frac{(\alpha_p - \alpha_n)\Delta T}{R_p + R_n + R_L} \right)^2 R_L}{(\alpha_p - \alpha_n)IT_1 + (K_p + K_n)\Delta T} \quad (4.16)$$

The efficiency is a complicated function of the resistances, and it can be shown to be a maximum when the ratio of the resistances is given by

$$M = \frac{R_L}{R_p + R_n} = \sqrt{1 + ZT_m}, \quad (4.17)$$

4.4. Efficiency of the Hybrid System

where the figure of merit Z is the same as in Eq. (4.12) and $T_m = (T_1 + T_2)/2$ is the average temperature of the source and sink. When the ratio of the resistances is the optimal value in Eq. (4.17), the efficiency of the thermoelectric element can be found to be

$$\eta_{TE} = \frac{\Delta T}{T_1} \frac{M - 1}{M + T_2/T_1}, \quad (4.18)$$

where $\Delta T/T_1$ is the efficiency of a Carnot cycle, [12] and it is seen that the efficiency of the thermoelectric generator is always less than that of a Carnot cycle. It is remarked that if the Seebeck coefficients both were 0, then $Z = 0$, $M = 1$ and $\eta_{TE} = 0$, illustrating that the Seebeck coefficients are essential in thermoelectric generators. If the value of Z could be very high, the efficiency would reach that of the Carnot cycle which is high when the temperature difference is large.

A great advantage of a thermoelectric generator compared to a Carnot cycle is the cm size of the generator, and the fact that once installed correctly it can last for many years. Thermoelectric generators have been used in many space missions where they successfully operated for more than 20 years. [7] Different types of thermoelectric generators are found and are typical divided into categories based on their maximal operating temperature, which can span from below 500 K to above 900 K. [26] A Carnot cycle, on the other hand, consists of an ideal gas in a cylinder undergoing many cycles of isothermal and adiabatic compression and expansion. [12] The compressor to control these cycles are typical bigger than thermoelectric generators and will break down at some time. Hence even the Carnot cycle has better efficiency than thermoelectric generators the generators have clear advantages.

The efficiency of a specific thermoelectric generator has been measured to 4%, and based on recent progress in the research on thermoelectric materials, an efficiency of 8% is also considered in [4]. Therefore these two values for the efficiency η_{TE} are applied in the thesis when calculating the efficiency of the hybrid system. It is important to notice that the thermoelectric efficiency is independent of the kind of heat that it is exposed to, as the external heat source can be e.g the sun or waste heat from machines. In this thesis the thermoelectric element serves as a component of the hybrid system that converts sunlight into electricity, thus the sun is the external heat source for the thermoelectric element. Being independent of the kind of heat, implies that its efficiency is independent of the wavelengths of light, which is totally opposite of the solar cell efficiency studied in the previous chapter, where its efficiency was strongly wavelength dependent. The efficiency of the solar cell is zero for wavelengths above the band gap wavelength, but these wavelengths can still be utilized by the thermoelectric element, which is the basic idea behind the hybrid system.

4.4 Efficiency of the Hybrid System

With the derived efficiency of the thermoelectric element in this chapter and the solar cell efficiency in the previous chapter, the efficiency of the hybrid system is found by combining these and is as a function of wavelength given by

$$\eta_{\text{hybrid}}(\lambda) = \begin{cases} \eta_{TE} & \text{for } 280 \leq \lambda < \lambda_{c,1} \\ \eta_{\text{solar}}(\lambda) & \text{for } \lambda_{c,1} \leq \lambda \leq \lambda_{c,2} \\ \eta_{TE} & \text{for } \lambda_{c,2} < \lambda \leq 2500, \end{cases} \quad (4.19)$$

where η_{TE} is the thermoelectric efficiency chosen to 4% or 8%, $\eta_{\text{solar}}(\lambda)$ is the solar cell efficiency from Eq. (3.8) and $\lambda_{c,1}$ and $\lambda_{c,2}$ are the lower and upper cut off wavelengths as

illustrated in Fig. 1.3b. For an ideal solar cell the optimal transmittance is seen in Fig. 1.3a and has only one cut off wavelength at 900 nm, and the first case of the efficiency in Eq. (4.19) disappears, and the efficiency of the hybrid system is the solar efficiency for wavelengths below 900 nm and the thermoelectric efficiency for wavelengths above 900 nm. The overall efficiency of the hybrid system is found by integrating the efficiency in Eq. (4.19) weighted with the solar spectrum and the transmittance or reflectance, yielding [4]

$$\eta_{\text{hybrid}} = \frac{\int_{280}^{\lambda_{c,1}} \eta_{TE} F(\lambda) T(\lambda) d\lambda + \int_{\lambda_{c,1}}^{\lambda_{c,2}} \eta_{\text{solar}}(\lambda) F(\lambda) R(\lambda) d\lambda + \int_{\lambda_{c,2}}^{2500} \eta_{TE} F(\lambda) T(\lambda) d\lambda}{\int_{280}^{2500} F(\lambda) d\lambda}. \quad (4.20)$$

Here $R(\lambda)$ is the reflectance and $T(\lambda)$ is the transmittance for the beamsplitter, and in calculating the efficiency in Eq. (4.20) it is utilized that the reflected light from the beamsplitter is directed onto the solar cell and the transmitted light onto the thermoelectric element, which is the case for a high-wavelength-pass beamsplitter. For an ideal solar cell the first term in the numerator disappears as only one cut off wavelength exists. If a low-wavelength-pass beamsplitter is used R and T has to be interchanged. This efficiency has to be maximized and the next chapter introduces the optimization problem and presents three optimization methods to maximize the efficiency.

5. The Optimization Problem

This chapter considers the largest challenge in the thesis, namely that of optimizing the beamsplitter resulting in the highest possible efficiency of the hybrid system. The efficiency to be optimized is given in Eq. (4.20) and is for a specific thermoelectric element and specific solar cell only a function of the transmittance T and reflectance R for the beamsplitter. These two quantities are calculated for some thicknesses and refractive indices for all the layers using one of the transfer matrix methods, and keeping the refractive indices constant implying that the transmittance and reflectance only depend on all the layer thicknesses. Putting these things together the efficiency is found as a function of all the layer thicknesses, hence the function to be optimized is a real-valued function mapping from N positive numbers into a positive number. Denoting $V = \mathbb{R}_{\geq 0} \times \cdots \times \mathbb{R}_{\geq 0}$ as the N -dimensional domain, the function is given by $f : V \rightarrow \mathbb{R}_{\geq 0}$. The function to be optimized in this thesis maps from N thicknesses with units of nm into a positive real number, but to avoid confusion about the units all thicknesses are chosen to be dimensionless during the optimization. In general the function expression is extremely complicated, as the product of several hundreds matrices has to be calculated in order to give the efficiency, and thereby it is impossible to solve $\vec{\nabla} f = \vec{0}$ analytically. Instead the methods presented in this chapter are iterative algorithms generating convergent sequences.

Any solution of an optimization problem begins with an initial guess, and in the next section two different methods of choosing it are presented. Afterwards three different optimization methods are presented and in chapter 6 they are implemented in Matlab and used to solve the optimization problem.

5.1 The Initial Guess

In this subsection two different methods of choosing the initial guess are briefly introduced. The focus here is on the theory behind the guesses while Sec. 6.2.1 considers the practical implementation of the guesses in Matlab. An ideal solar cell is considered when constructing the initial guess, and the method is easily generalized to handle real solar cells which will be the topic from Sec. 7.2 and forward.

As explained in Sec. 2.7 band gaps occur at wavelengths where the transmittance is zero. Given some thicknesses, refractive indices and incident angle one or more band gaps occur in some wavelength interval as seen in Fig. 2.12. Here a quarter wave structure is considered resulting in relative small band gaps compared to the ideal band gap from 280-900nm as seen in Fig. 1.3a. The idea in constructing such a wide band gap is to use quarter wave layers given different band gaps as building blocks, and successively put these blocks together in a composite structure. [31] A block is understood as a number of identical unit cells consisting of the materials 1 and 2 as seen in Fig. 2.6. A composite structure of M blocks is illustrated in Fig. 5.1 where each block consists of 3 unit cells with light incident from left. The thicknesses of the two front layers of material 2 and 3 are taken to be quarter wave layers for the wavelength 280nm, while the thicknesses of the blocks increase through the structure due to the increase in desired band gap wavelength. The two methods of choosing the initial guess are closely related and are based on quarter wave structures as explained in Sec. 2.3.1. To have a band gap at a certain design wavelength λ_0 the thicknesses must be $a_i = \lambda_0 / (4n_i \cos \theta_i)$ from Eq. (2.30) with $i = \{1, 2\}$, where θ_i is the angle of propagation in material i with refractive index n_i .

In both methods the idea is to construct the blocks in such a way that they give rise to a

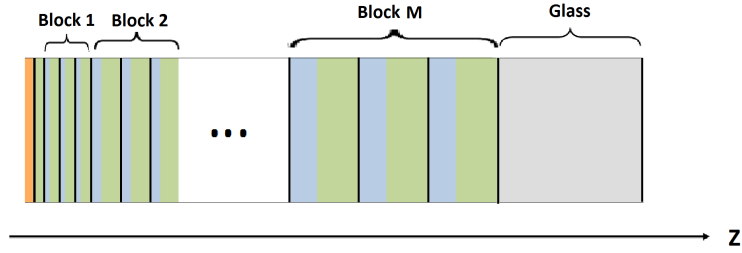


Figure 5.1: Illustration of a block structure with M blocks and 3 unit cells in each block, where light is incident from left. The thicknesses of the two front layers of material 2 and 3 are taken to be quarter wave layers for the wavelength 280nm, and the thicknesses of the blocks increase through the structure.

band gap in different wavelength intervals. The idea of the first method is to calculate the thicknesses of the individual blocks creating some individual band gaps, and to compose these blocks to form the structure in Fig. 5.1. For a given incident angle the band gap sizes of the individuals blocks are investigated to find out how many blocks are needed, and if there should be a small overlap between the blocks to avoid holes in the total band gap. For the second method of choosing the initial guess the idea is to construct quarter wave layers only for first and last block, giving band gaps around 280nm and 900nm, and to use these thicknesses to calculate the thicknesses of the intermediate blocks using linear interpolation. In Sec. 6.2.1 it is shown how the two guesses are implemented and that they give almost the same result.

5.2 The Optimization Methods

In this section three different optimization methods are presented and studied in detail, where the focus is on minimizing a function, where it is utilized that a function f is maximized if $-f$ is minimized. [3] The function to be minimized is $f = -\eta_{\text{hybrid}}$ from Eq. (4.20) and the minimum of this function gives the maximal efficiency of the hybrid system. All three optimization methods only find local minima as it is almost impossible to guarantee that a found minimum of such a complicated function as considered here should be the global minimum.

The first two methods are based on the gradient and uses different ways of choosing the step length and the last method is a simplex derivative-free method. The methods have different stopping criteria and in order to compare them a common criteria must be applied. In chapter 6 the methods are compared based on their performance and time consumption.

5.2.1 The Gradient Methods

In this subsection the gradient methods are presented.

In general the iteration formula for the optimization algorithms are given by

$$\vec{x}_{k+1} = \vec{x}_k + \mu_k \Delta \vec{x}_k, \quad (5.1)$$

where \vec{x}_k and \vec{x}_{k+1} are in the domain of f , $\Delta \vec{x}_k$ is the descent direction, k is the iteration number and μ_k is the step length. The general steepest descent method is given by

Algorithm 5.1 General steepest descent method ([3])

Given an initial guess $\vec{x} \in V$
Repeat
(i). Determine a descent direction $\Delta\vec{x}$.
(ii). Line search. Choose a step length $\mu > 0$.
(iii). Update. $\vec{x} := \vec{x} + \mu\Delta\vec{x}$.
Until a stopping criterion is satisfied.

In the algorithm there are two things to be determined in every iteration: A descent direction and a step length. The descent direction is determined to be minus the gradient, as the function decreases the most in that direction, hence $\Delta\vec{x}_k = -\vec{\nabla}f(\vec{x}_k)$. A minimum is found when the function becomes appropriately flat, hence the stopping criteria $\|\vec{\nabla}f(\vec{x})\|_2 < \tilde{\varepsilon}$ is applied, where $\|\cdot\|_2$ is the Euclidean norm and $\tilde{\varepsilon} > 0$ is some threshold value. The line search can be done in two different ways, exact and inexact, which are presented individually in the next two subsections. [3]

Exact Line Search

Once the descent direction is determined, the problem of determining the step length reduces to a minimization with respect to μ of a one-dimensional function along the descent direction. Hence the optimal step length is given by

$$\mu_k = \min_{\mu > 0} f(\vec{x}_k - \mu\vec{\nabla}f(\vec{x}_k)). \quad (5.2)$$

In some cases this can be solved analytically. When this is not the case the solution of Eq. (5.2) becomes an optimization problem in itself to be solved with numerical methods which can be time consuming. Exact line search is therefore preferable in situations where the calculation of the gradient is hard and a solution of Eq. (5.2) is easier. [3]

In this thesis the function to be optimized depends on the transmittance and reflectance calculated by one of the transfer matrix methods. The quantities are in both cases found by calculating the products of more than hundred 2x2 matrices. It is actually possible to write down an explicit expression for the transmittance and reflectance but it gets extremely complicated when many matrices are present. Instead the function to be optimized is calculated numerically and the same applies for the gradient. The first partial derivative is given by

$$\frac{\partial f(\vec{x}_k)}{\partial x_{k1}} = \lim_{\Delta x \rightarrow 0} \frac{f(x_{k1} + \Delta x, x_{k2}, \dots, x_{kN}) - f(x_{k1}, x_{k2}, \dots, x_{kN})}{\Delta x}, \quad (5.3)$$

and similar for the remaining $N - 1$ parameters where x_{ki} is the i 'th component of the vector \vec{x}_k . Calculating partial derivatives in this way a term like $f(x_{k1} + \Delta x, x_{k2}, \dots, x_{kN})$ has to be evaluated every time. Such an evaluation in itself calculates the product of all the 2x2 matrices and is thus said to be a function call. Hence one partial derivative uses one function call, and it therefore costs N function calls to calculate the gradient in one point. When the gradient is calculated the step length is found using Eq. (5.2) where a number of steps, N_{step} , is chosen. Now, $\mu = \{1, 2, \dots, N_{step}\}$ is chosen and $f(\vec{x}_k - \mu\vec{\nabla}f(\vec{x}_k))$ calculated, giving N_{step} function values. The minimum of these is found and the corresponding μ is chosen as the step length. If $\mu = N_{step}$ is found it could indicate that the function is still decreasing in the point $\vec{x}_k - N_{step}\vec{\nabla}f(\vec{x}_k)$ in the direction of $-\vec{\nabla}f(\vec{x}_k)$, and it is continued to search for a smaller minimum in that direction. It

is chosen to set $\mu = \{N_{step} + 1, N_{step} + 2, \dots, 2N_{step}\}$ and repeat the procedure until a minimum is found that is not the last point in the given iteration. Once such a minimum is found the point \vec{x}_{k+1} is calculated using Eq. (5.1), and the algorithm is repeated.

This way of choosing the step length does not find μ in Eq. (5.2) precisely, because a minimum could occur between two integral values of μ . A way of making it more precise is to apply a finer resolution on μ resulting in more function calls. But if the initial guess is far from the minimum it takes a long time getting close to that, and a small step length results in many function calls on the way towards the minimum. In such a case, it would be convenient to choose a rougher resolution on μ in order to get larger step lengths. [24] When implementing the algorithm it works fine with a resolution of 1 and $N_{step} = 10$, and other choices have therefore not been examined.

A theorem gives that the gradient method converges to a minimum if the function is continuously differentiable on a bounded sublevel set $S = \{\vec{x} \in V : f(\vec{x}) \leq f(\vec{x}_0)\}$, where $\vec{x}_0 \in V$ is the initial guess. The sequence is given by Eq. (5.1) where the step length μ_k is determined by exact line search. A proof of the theorem can be found in [9]. Even without an analytic expression for the function f it is assumed to be continuously differentiable, and the theorem can be applied. In chapter 6 the performance of the method and its time consumption will be investigated and compared with the other two methods.

Inexact Line Search

An inexact line search method finds a step length that is sufficient under certain conditions. The Armijo condition states that the function must decrease sufficiently when taking a step in the direction of $-\vec{\nabla}f(\vec{x}_k)$, and is formulated as

$$f(\vec{x}_k - \mu_k \vec{\nabla}f(\vec{x}_k)) \leq f(\vec{x}_k) - c_1 \mu_k \|\vec{\nabla}f(\vec{x}_k)\|^2, \quad (5.4)$$

where $c_1 \in (0, 1)$ is a constant to choose. The one-dimensional function to minimize along the search direction is defined as $\varphi(\mu_k) = f(\vec{x}_k - \mu_k \vec{\nabla}f(\vec{x}_k))$, and the Armijo condition in Eq. (5.4) can be written

$$\varphi(\mu_k) \leq \varphi(0) + c_1 \mu_k \varphi'(0). \quad (5.5)$$

Denoting the right hand side of Eq. (5.5) by $l(\mu_k)$ the Armijo condition is illustrated in Fig. 5.2. For the function $\varphi(\mu_k)$ to decrease sufficiently the step length μ_k must be chosen such that $\varphi(\mu_k)$ is under the straight line $l(\mu_k)$, which in the figure happens in the two acceptable regions. The slope of the line is negative, given by $c_1 \varphi'(0)$, thus scaling linearly with the chosen value c_1 . In practice, often a small value of c_1 is chosen in order to obtain a flat negative slope of $l(\mu_k)$. The Armijo condition is always satisfied for very small values of μ_k , thus another condition is imposed to guarantee that the found step length is not too short. The curvature condition states that

$$\vec{\nabla}f(\vec{x}_k - \mu_k \vec{\nabla}f(\vec{x}_k))^T \vec{\nabla}f(\vec{x}_k) \leq c_2 \|\vec{\nabla}f(\vec{x}_k)\|^2, \quad (5.6)$$

where $c_2 \in (c_1, 1)$ is another constant to choose. Applying $\varphi(\mu_k)$ the condition in Eq. (5.6) can be written as

$$\varphi'(\mu_k) \geq c_2 \varphi'(0). \quad (5.7)$$

The conditions in Eq. (5.5) and (5.7) are collectively known as the Wolfe conditions. The condition in Eq. (5.7) states that the slope of $\varphi(\mu_k)$ is a constant times larger than the slope of $\varphi(0)$, and is illustrated in Fig. 5.3. For a step length to be accepted both Wolfe

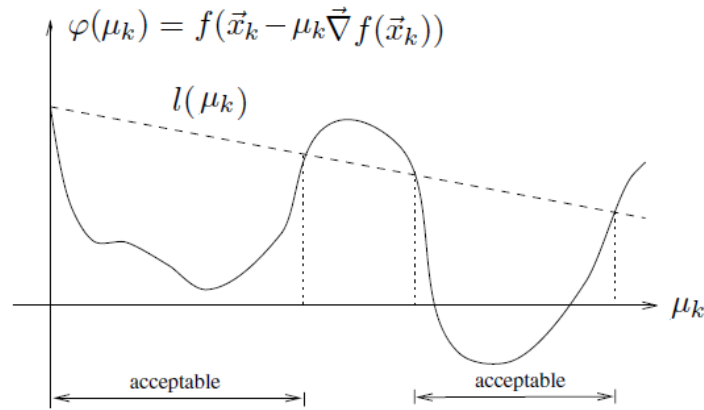


Figure 5.2: The Armijo condition is satisfied when a sufficient decrease in $\varphi(\mu_k)$ is achieved which happens in the acceptable regions. Figure from [24].

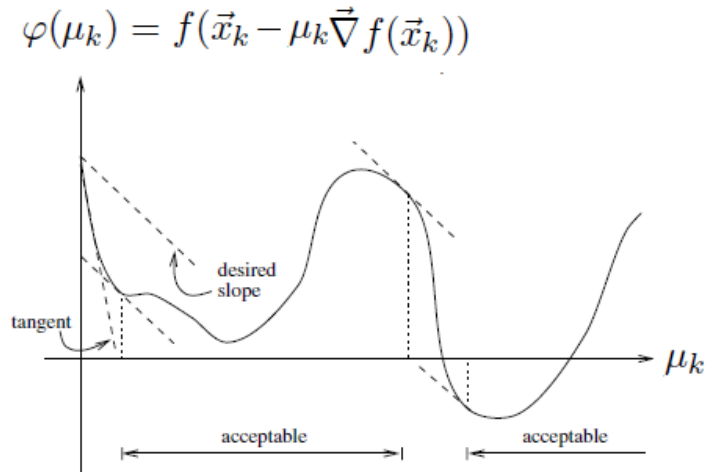


Figure 5.3: The curvature condition is satisfied when the slope of $\varphi(\mu_k)$ is a constant times larger than the slope of $\varphi(0)$ which happens in the two acceptable regions. Figure from [24].

conditions must be satisfied, hence it must be in a region that is acceptable in Fig. 5.2 and 5.3 at the same time.

Another way of ensuring that the step length is not too small is by backtracking line search. A step length $\mu_{start} > 0$ and $\alpha, \beta \in (0, 1)$ are chosen, and it is checked whether the Armijo condition in Eq. (5.5) is satisfied with $c_1 = \alpha$. If it is satisfied μ_{start} is an acceptable step length. If not, the step length is reduced by multiplying by β and it is checked if the condition is satisfied with the new shorter step length, and the procedure is repeated until an acceptable step length is found. With this method the step length is not too short, as the acceptable step length is μ_k/β where μ_k was violating the Armijo condition. In practice it is an idea to choose μ_{start} relatively long to avoid a too short step length, and if μ_{start} was chosen wrong it is reduced by backtracking. The backtracking line search is described in Algorithm 5.2. [24]

A theorem states that backtracking line search converges when the function $f : V \rightarrow \mathbb{R}$ is bounded below and continuously differentiable, and where the step length is found using

Algorithm 5.2 Backtracking line search ([24])

Choose $\mu_{\text{start}} > 0$, $\alpha \in (0, 1)$ og $\beta \in (0, 1)$, and let $\mu := \mu_{\text{start}}$.
while $f(\vec{x}_k - \mu \vec{\nabla} f(\vec{x}_k)) > f(\vec{x}_k) - \alpha \mu \|\vec{\nabla} f(\vec{x}_k)\|^2$ **do**
 $\mu := \beta \mu$
end while
 $\mu_k := \mu$

backtracking line search. The proof of the theorem can be found in [29].

Both these methods to choose the step length uses the gradient as an important part of the iterations, and it costs N function calls to calculate the gradient in every point. The line search can also cost several function calls, thus many function calls are needed when using a gradient method to solve an optimization problem. Another type of optimization methods that does not use the gradient is the simplex algorithms and such an algorithm is studied in the next subsection.

5.2.2 The Nelder-Mead Method

In this subsection based on [20] the Nelder-Mead optimization method is presented where the focus is to explain the method in words while the original source code for the algorithm can be found in [21] and a modified version in the file `fminsearch2` from [30]. First the method is explained without any boundaries for the variables, and afterwards it is showed how to transform a bounded problem into an unbounded problem. Lastly the convergence of the method is analysed.

The basic idea in the Nelder-Mead method is very different from the gradient methods studied in the previous subsection. It is a derivative-free simplex method using direct search that it effective in optimizing a function of several variables. To keep it as simple as possible, a function of two variables will be considered and the method explained based on this while the concept is generalizable to several variables.

A simplex in two dimensions is a triangle and the idea behind the Nelder-Mead simplex algorithm is to compute the function values in every vertex of the triangle. The vertex with the highest value is rejected and replaced by another point, thus constructing a new triangle. The algorithm generates a sequence of triangles where the function values in the vertices gets smaller and smaller. The size of the triangle is possibly reduced until the coordinates of the minimum is found when some stopping criterion is satisfied.

Like the other optimization methods the algorithm needs an initial guess \vec{x}_0 , and it begins by constructing an initial triangle by adding 5% of both components $x_0(i)$ to \vec{x}_0 , thus constructing two new points. If a component of \vec{x}_0 is zero, the component of the new point is by default set to 0.00025. These two points together with \vec{x}_0 forms the initial triangle, and similar is done when several variables are present, constructing a simplex with $N + 1$ vertices in N -dimensional space. The function values are evaluated in each vertex of the initial triangle and the vertices are sorted according to their function values. To keep the notation simple the vertices are called **B**, **G** and **W** to denote the best, good and worst vertex. To find the minimum several processes are needed, which now will be examined.

The processes apply the midpoint of the good side, i.e. the line segment joining **B** and **G** and the midpoint is called **M** and given by $\mathbf{M} = (\mathbf{B} + \mathbf{G})/2$ as the average of **B** and **G**, and the distance from **M** to **W** is called d as illustrated in Fig. 5.4A). As the function decreases on the line from **W** to **B** and from **W** to **G**, it is investigated whether the function takes on smaller values on the other side of the line **BG**. A reflection point **R** is

constructed by reflecting the triangle BGW in the line BG , thus R is a distance d from BG , see Fig. 5.4A). In vector notation the coordinates of R are given by

$$\mathbf{R} = \mathbf{M} + (\mathbf{M} - \mathbf{W}) = 2\mathbf{M} - \mathbf{W}. \quad (5.8)$$

The function value in R is calculated and compared to those in B , G and W . If R is a

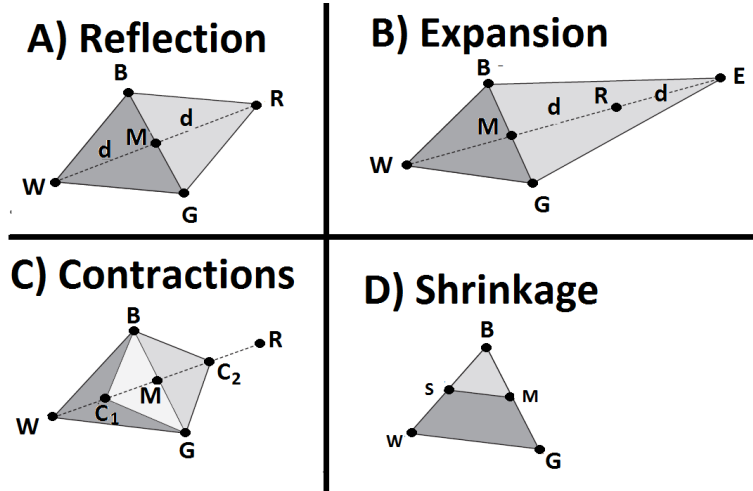


Figure 5.4: Illustration of the four processes in the Nelder-Mead method where D is a shrinkage shown for an inside contraction. In all cases the initial triangle is the most gray, while the new triangle is lighter gray. Figure from [20].

better point than B , i.e. $f(\mathbf{R}) < f(\mathbf{B})$, it could indicate that the function decreases further in the direction of $\mathbf{M} - \mathbf{R}$, and an expansion point E is constructed by extending the line segment RW with the distance d , see Fig. 5.4B). In vector notation the coordinates of E are given by

$$\mathbf{E} = \mathbf{R} + (\mathbf{R} - \mathbf{M}) = 2\mathbf{R} - \mathbf{M}. \quad (5.9)$$

The function value is calculated in E and if $f(\mathbf{E}) < f(\mathbf{R})$ the point E is accepted and replaces R in the triangle, which now becomes BGE . If $f(\mathbf{E}) \geq f(\mathbf{R})$ the point E is rejected and R accepted and the triangle becomes BGR .

If R was not better than B it could still be better than G , and this case is considered now. If R is better than G , the point R is accepted and the triangle becomes BGR . If R is not better than G the triangle is reduced by performing a contraction or a shrinkage. If $f(\mathbf{R}) \geq f(\mathbf{W})$ the contraction is made in the direction of W , which is called an inside contraction constructing the point

$$\mathbf{C}_1 = \mathbf{M} + \frac{\mathbf{W} - \mathbf{M}}{2} \quad (5.10)$$

see Fig. 5.4C). If C_1 is better than W the point C_1 is accepted and the triangle becomes BGC_1 . If C_1 is not better than W the triangle is shrunk towards B by replacing G by M and W by S , which is the midpoint of the line BW , see in Fig. 5.4D) On the other hand, if $f(\mathbf{R}) < f(\mathbf{W})$, the contraction is made in the direction of R , which is called an outside contraction giving the point

$$\mathbf{C}_2 = \mathbf{M} + \frac{\mathbf{R} - \mathbf{M}}{2}. \quad (5.11)$$

Like for the inside contraction the point C_2 is accepted if and only if it is better than R . If this is not the case the triangle is again shrunk towards B replacing G by M and R by S , which now is the midpoint of the line BR . A common term for the two contraction points is called C .

A great advantage of the Nelder-Mead method is the fact that it does not use any derivative of the function. As explained in Sec. 5.2.1 the calculation of the gradient costs N function calls, thus very expensive. The Nelder-Mead uses fewer function calls as it only calls the function when necessary, for example a reflection only costs one function call, an expansion costs two, a contraction costs two but a shrink costs $N - 1$ function calls, but is also very rare to occur. [14] In Sec. 6.4.3 it will be shown that the Nelder-Mead method is much faster than the gradient methods. In each of the cases in Fig. 5.4 a new triangle is constructed and the procedure is repeated until a stopping criteria is met which is considered in the following subsection. [20] and [21].

To exemplify the algorithm, consider the function $f(x, y) = x^2 - 4x + y^2 - y - xy$ and the three starting vertices: $V_1 = (0, 0)$, $V_2 = (1.2, 0)$ and $V_3 = (0, 0.8)$. It is found that V_2 is best, V_3 is good and V_1 is worst. The triangle is first expanded, and the 10 first iterations are seen in Fig. 5.5 where the method converges to the minimum in $(3, 2)$. [20]

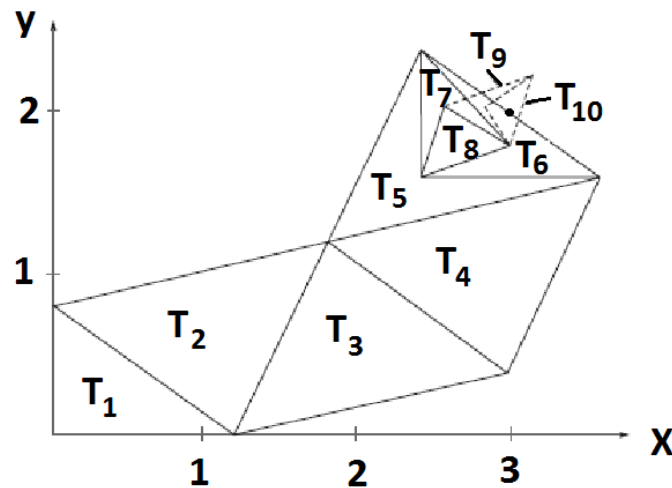


Figure 5.5: Example of optimizing the function $f(x, y) = x^2 - 4x + y^2 - y - xy$ using the Nelder-Mead method where the initial triangle consists of the points $V_1 = (0, 0)$, $V_2 = (1.2, 0)$ and $V_3 = (0, 0.8)$. After 10 iterations the minimum is found in $(3, 2)$. Figure from [20].

The Nelder-Mead Method with Bounds

Until now it has been assumed that there are no boundaries for any of the variables in the function, implying that negative layer thicknesses are allowed. Of course this has no physical meaning and this subsection based on [5] introduces a method to transform a bounded problem into an unbounded problem, which can be solved by the Nelder-Mead method.

Four different types of constraints exist for a bounded problem: The variables can have a lower bound, upper bound, dual bounds or some variables can be fixed. In this thesis the optimization problem finds the optimal thicknesses of all the layers in the beamsplitter, and all these thicknesses must be non-negative with no upper bounds. Hence all the variables

are bounded below by the N -dimensional zero vector, denoted LB. The transformation is quadratic for a single bound and a sine transformation for dual bounds, and only the quadratic transformation will be examined in this thesis.

First the initial values $x_0(i)$ are transformed into their unconstrained substitutes, denoted by tilded coordinates, by the transformation

$$\tilde{x}_0(i) = \begin{cases} 0 & , x_0(i) \leq \text{LB}(i) \\ \sqrt{x_0(i) - \text{LB}(i)} & , x_0(i) > \text{LB}(i) \end{cases}, \text{ for } i = 1, \dots, N. \quad (5.12)$$

When $\text{LB}(i) = 0$ for all $i = 1 \dots, N$ and all the initial values $x_0(i)$ are positive the transformation in Eq. (5.12) simplifies to $\tilde{x}_0(i) = \sqrt{x_0(i)}$.

The Nelder-Mead method is now applied with \tilde{x}_0 as the initial guess. The function values for every iteration are calculated using the original coordinates, and the corresponding tilded coordinates of the final point, \tilde{x}_{final} is transformed into the original coordinates by the inverse transformation, thus $x_{\text{final}}(i) = \tilde{x}_{\text{final}}(i)^2$. Notice that some components of \tilde{x}_{final} can be negative, but the inverse transformation secures that all components of \tilde{x}_{final} are non-negative.

From now on the Nelder-Mead method always refers to the bounded Nelder-Mead method, where the optimization problem is solved by transforming it into an unbounded problem, that is solved and transformed back again. The original Matlab code for the transformation is found in [5], and the code applied in this thesis is found in the file `fminsearchbnd2` from [30].

Convergence of the Nelder-Mead Algorithm

In the Nelder-Mead source code from Matlab, the algorithm continues until two conditions are satisfied at the same time. The first condition is that

$$\max(\| \mathbf{V}_2 - \mathbf{V}_1 \|_\infty, \| \mathbf{V}_3 - \mathbf{V}_1 \|_\infty, \dots, \| \mathbf{V}_{N+1} - \mathbf{V}_1 \|_\infty) \leq \text{TolX}, \quad (5.13)$$

where TolX is a specified threshold value and $\| \cdot \|_\infty$ is the infinity norm which for a vector $\vec{x} = (x_1, x_2, \dots, x_N)$ is defined as [3]

$$\| \vec{x} \|_\infty = \max(|x_1|, |x_2|, \dots, |x_N|). \quad (5.14)$$

In Eq. (5.13) \mathbf{V}_1 is the current best point, \mathbf{V}_2 is the next best point and so on. Hence the criterion demands that the distance between the points must be smaller than some tolerance value, which by default in Matlab is $\text{TolX}=10^{-4}$. The second criteria is that the belonging function values at the vertices must also be smaller than some threshold value, which also by default in Matlab is $\text{TolFun}=10^{-4}$, and the criteria is formulated as

$$\max(|f(\mathbf{V}_1) - f(\mathbf{V}_2)|, |f(\mathbf{V}_1) - f(\mathbf{V}_3)|, \dots, |f(\mathbf{V}_1) - f(\mathbf{V}_{N+1})|) \leq \text{TolFun}. \quad (5.15)$$

The points are already sorted before testing for convergence, hence it should be sufficient to test if $|f(\mathbf{V}_1) - f(\mathbf{V}_{N+1})| \leq \text{TolFun}$ instead of testing Eq. (5.15) as $f(\mathbf{V}_{N+1})$ is the worst point.

In [14] the convergence properties of the Nelder-Mead method is discussed. The method is widely used in many areas of science, but no general theoretical results about its convergence have actually been proved except for a strictly convex function in 1 and 2 dimensions. But if $f : V \rightarrow \mathbb{R}$ is bounded below, then the sequence of function values belonging to the best vertex in every iteration is convergent even for non-convex functions. Furthermore at every non-shrink step in the algorithm, the function values belonging to any vertex

decreases for every iteration, see Lemma 3.3 in [14]. The function to be optimized in this thesis is of hundreds of variables and it is very unlikely to be convex. Hence to ensure convergence of the Nelder-Mead method the conditions in Eq. (5.13) and Eq. (5.15) are rejected, as the algorithm is found to be non-convergent when applying these stopping criteria. Denoting the function value in the best point in the k 'th iteration by $f(\mathbf{V}_1^k)$, the applied stopping criteria is

$$|f(\mathbf{V}_1^{k+1}) - f(\mathbf{V}_1^k)| < \varepsilon, \quad (5.16)$$

where ε is a threshold value similar to $\tilde{\varepsilon}$ used in the gradient methods. The iteration number k is only updated when a new best point is found which can take hundreds of processes to achieve, especially in the iteration from the best point in the initial simplex to a new best point. Hence the k in the Nelder-Mead method is not comparable to the k in the gradient methods, and in Sec. 6.4.3 a way to compare the methods are found.

6. Matlab Implementation

With the necessary theory regarding the hybrid system derived in chapter 2 to 4 and the optimization problem described in the previous chapter this chapter deals with the implementation of the theory.

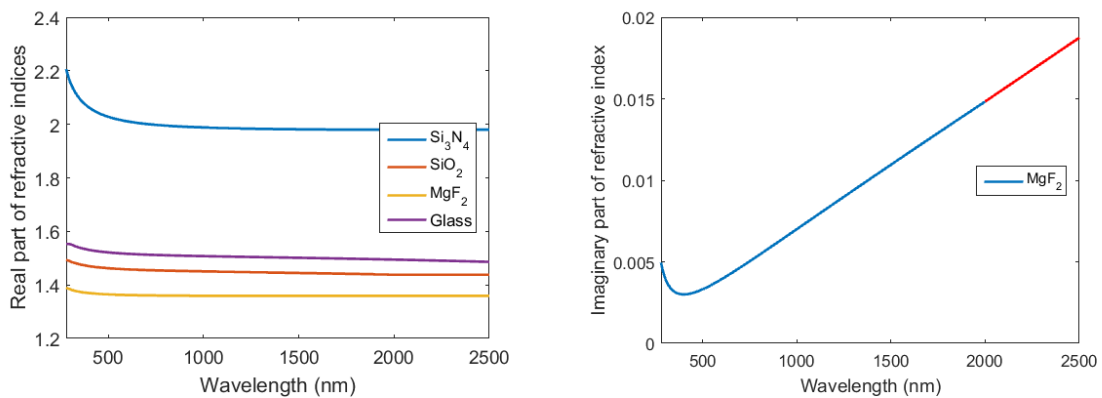
Before implementing the optimization methods it is important to verify the two transfer matrix methods derived in chapter 2, and in Sec. 6.1 it is shown that the two methods are equivalent. As mentioned in chapter 5 an initial guess is needed in order to solve the optimization problem and Sec. 6.2.1 serves as the implementation of the initial guess. Then the three optimization methods are implemented and it is shown how to compare them based on their performance and time consumption.

All the calculations in this chapter are performed for a high-wavelength-pass beamsplitter and an ideal solar while the results for a microcrystalline and amorphous solar cell are found in Sec. 7.2 and 7.3, and the results for a low-wavelength-pass beamsplitter are found in Sec. 7.5.

6.1 Applied Data and Verification of the Transfer Matrix Methods

In this section the applied data for the refractive indices is presented and it is verified that the two transfer matrix methods are equivalent.

The applied materials for constructing the beamsplitter is silicon nitride, Si_3N_4 , silicon dioxide SiO_2 and magnesium fluoride, MgF_2 , deposited on BK7 glass. Hence the refractive indices of these materials must be specified. All the data is from [18] except the real part of glass which is from [1]. The refractive indices are found for different wavelengths and some of them are below 280nm which is the lowest wavelength in the solar spectrum in Fig. 3.2. The data is therefore interpolated to the same wavelengths in the interval 280-2500nm using linear interpolation. The real parts of the refractive indices all decreases with the wavelength as shown in Fig. 6.1a and the imaginary parts are shown in Fig. 6.1b. Both SiO_2 and glass have no imaginary part and Si_3N_4 only has an imaginary part for



(a) Real part of the refractive indices.

(b) Imaginary part of the refractive indices.

Figure 6.1: Refractive indices for the materials applied in the beamsplitter. The red points in the figure at right are constructed using the slope from 1000-2000 nm.

wavelengths below 300nm which is chosen not to include in Fig. 6.1b. The imaginary part of MgF_2 increases almost linear from 500nm, but the data from [18] only goes to 2000nm

where it is still increasing. If it is assumed that it increases with the same slope in the interval 2000-2500nm the red points in Fig. 6.1b give the imaginary refractive index in that interval. If the beamsplitter optimized in this thesis is to be fabricated, an idea is to measure the refractive indices of all the applied materials in the range 280-2500nm and apply these values as the data.

With the relevant data for the refractive indices applied to construct the beamsplitter given in Fig. 6.1, the two transfer matrix methods can be used to calculate the transmittance, reflectance, and absorbance for any structure. The two methods have been implemented independently of each other and their results are found to be the same. This applies for both polarizations of the light, for arbitrarily incident angles and for complex refractive indices.

As explained in Sec. 2.4.1 reciprocity causes that the transmittance through the beamsplitter is independent of its orientation while the reflectance and absorbance are not. By reversing the structure and calculating the transmittance, reflectance, and absorbance it is found that the reciprocity principle is satisfied for a simple structure consisting of five unit cells. In Sec. 7.4 it is verified that the reciprocity principle is also satisfied for the optimized beamsplitter consisting of more than 100 layers and the optimal orientation of the beamsplitter is found.

6.2 Implementation of the Transfer Matrix Method

With the transfer matrix methods verified in the previous section this section shows how the functions are implemented in Matlab.

Many different input parameters are needed in the program, like the wavelength interval and the refractive indices of all the materials, and in addition some parameters determine which part of the program to run. `transfer_method` determines which of the transfer methods to use and accepts the inputs 'Admittance' or 'E field' while `optimize_method` determines which optimization method to use and accept the inputs 'Exact', 'Backtracking' or 'Nelder-Mead'. The parameter `solar_cell` specifies which solar cell type to use and accepts the inputs 'Ideal', 'Microcrystalline' or 'Amorphous', and at last the parameter `Beamsplitter` determines which kind of beamsplitter to use and accepts the inputs 'High-pass' or 'Low-pass'. All these parameters are used when running the program, and the idea in the implementation is to make the code as general as possible, and to do that it is convenient to store all these parameters in a data cell

$$\text{data}=\text{cell}(1,27), \quad (6.1)$$

with 27 different parameters in total which can be numbers, vectors or strings.

The transmittance, reflectance, and absorbance are calculated using one of the two transfer matrix methods, and depend on the thicknesses of all the layers, their refractive indices and the incident angle. All these parameters are stored in `data`, thus it is convenient to give the whole `data` as input instead of just a sub cell containing the relevant data. The following function is written in Matlab in order to calculate the transmittance, reflectance, and absorbance and can be found in [30].

$$\text{function} [\text{Trans},\text{Ref},\text{Abs}] = \text{trans_ref_function}(\text{A},\text{data}), \quad (6.2)$$

where `A` is a vector containing the thicknesses of all the materials in the structure, and the function starts by extracting only the relevant parameters from `data`. The function calculates the transmittance `Trans` and reflectance `Ref` from Eq. (2.43) if the electric field transfer matrix method is applied and from Eq. (2.68) and (2.75) if the admittance

6.2. Implementation of the Transfer Matrix Method

method is applied and in both cases the absorbance `Abs` is calculated as `Abs=1-Trans-Ref` as it is faster than using Eq. (2.76). The transmittance, reflectance, and absorbance all depend on the polarization, hence the `trans_ref_function` could also take polarization as an input. The radiance from the sun consists of many different polarizations but can as a good approximation be described as the average of s- and p polarization. [32] The `trans_ref_function` therefore calculates the transmittance, reflectance, and absorbance for both polarizations and returns their averages.

The two transfer matrix methods are equivalent, thus the result is independent of `transfer_method`. To examine whether one of the methods is computationally faster than the other, the two methods are tested on the same code and their time consumption compared. It is found that the admittance method is approximately 1.5 times faster than the electric field method, which must be due to the fact that only half as many matrices have to be multiplied in this method, and this method is therefore applied from now on.

6.2.1 Implementation of the Initial Guess

Applying the `trans_ref_function` to calculate the transmittance, the purpose is to find the thicknesses that give a transmittance as close as possible to the ideal transmittance in Fig. 1.3a. The initial guess is found by applying the ideas explained in Sec. 5.1 and this subsection serves as the implementation of these ideas.

The following thicknesses are all calculated for an incident angle of 45° . From the refractive indices of the materials in Fig. 6.1a the angle of propagation θ_i in material i is calculated using Snell's law and are found to be $\theta_1 = 19^\circ$, $\theta_2 = 28^\circ$ and $\theta_3 = 31^\circ$ when the wavelength is 280 nm. It has been chosen to let Si_3N_4 be material 1, SiO_2 be material 2 and MgF_2 be material 3 which is the case throughout the thesis. In the first method of choosing the initial guess from Sec. 5.1, the first block must have a band gap around 280nm and from the refractive indices and propagation angles the thicknesses $a_1 = 33\text{nm}$ and $a_2 = 53\text{nm}$ are found using Eq. (2.30). Here the real parts of the refractive indices have been applied in order to get real thicknesses. With these thicknesses the band gap size is found to be approximately 65nm, hence the next block is constructed to have a band gap around 345nm, giving the thicknesses $a_1 = 44\text{nm}$ and $a_2 = 66\text{nm}$, where the propagation angles have been calculated for the new wavelength. This process is repeated until a band gap around 900nm is found giving 10 blocks in total, where the thicknesses of the last block are $a_1 = 116\text{nm}$ and $a_2 = 169\text{nm}$. The front layer of MgF_2 is constructed to be a quarter wave layer for the wavelength 280nm, giving the thickness 58nm, and the next outer layer of SiO_2 is taken to be of same thickness as a_2 in the first block, e.i 53nm.

The next issue is to determine the number of unit cells in the individual blocks. To make the initial guess as simple as possible, it is chosen that every block consists of the same number of unit cells. If there are too few unit cells in the blocks, the band gap is not complete as non-negligible transmittance occurs below 900nm, and the cut off between transmittance and reflectance becomes too smooth. On the other hand, a large number of unit cells in the blocks does not improve the initial guess but adds unnecessary extra parameters and it is chosen here to let 8 unit cells in the blocks be optimal. In Sec. 7.1.1 the total efficiency is studied as a function of number of layers, and considers other numbers of unit cells in each block. Hence the structure considered here consists of 10 blocks with 8 unit cells in each, and with the extra front layers of SiO_2 and MgF_2 it gives 162 layers in total. The thicknesses of all the blocks are seen in Table 6.1.

The transmittance, reflectance, and absorbance are calculated for this structure and are seen in Fig. 6.2, where it is remembered that the quantities are the average of s- and p polarization. The band gap is almost complete as the transmittance is very small

Block number	Thickness of Si ₃ N ₄ in nm	Thickness of SiO ₂ in nm
1	33	53
2	44	66
3	53	79
4	62	92
5	71	105
6	80	118
7	89	131
8	98	143
9	107	156
10	116	169

Table 6.1: Thicknesses of the materials for the first method of choosing the initial guess. All the blocks consist of 8 unit cells.

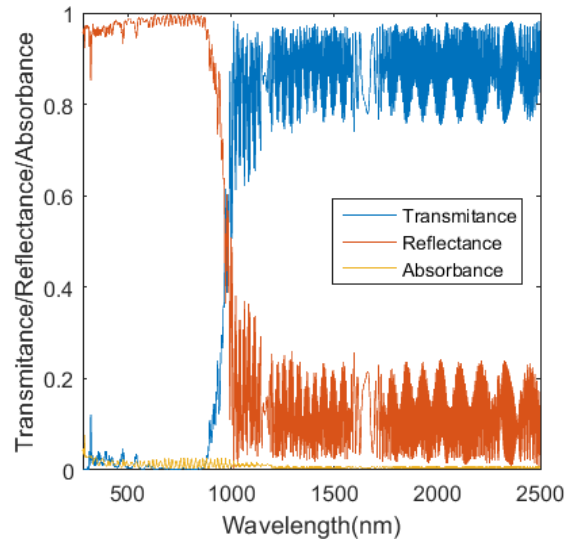


Figure 6.2: transmittance, reflectance, and absorbance for the initial guess consisting of 162 layers.

below 900nm. The cut off is very close to 900nm but above this value large oscillations in transmittance and reflectance occur, which is caused by multiple reflections in the 1mm glass layer used as the substrate. In the figure the transmittance, reflectance, and absorbance are calculated at every integer wavelength in the interval 280-2500nm, but this resolution seems not good enough above 900nm, as all the oscillations are not caught. A way to deal with this problem is to apply a smaller sampling wavelength of e.g 0.1nm, but this would lead to 10 times more calculations, thus slowing the program a lot. Another way to deal with the problem is to apply a thinner layer of glass in the calculations. It is found that a glass thickness of 2.5 μ m, the same as the largest wavelength, gives rise to sinusoidal oscillations caught by the sampling wavelength of 1nm. This thickness is therefore applied in the following figures, where the only difference is the amount of oscillations above 900nm. When fabricating the beamsplitter the structure really has to be deposited on 1mm glass, so the oscillations in Fig. 6.2 describe the physics of the oscillations correctly, and it is important to remember that the thinner glass layer is only applied to lower the number of computations in the program. But when measuring the

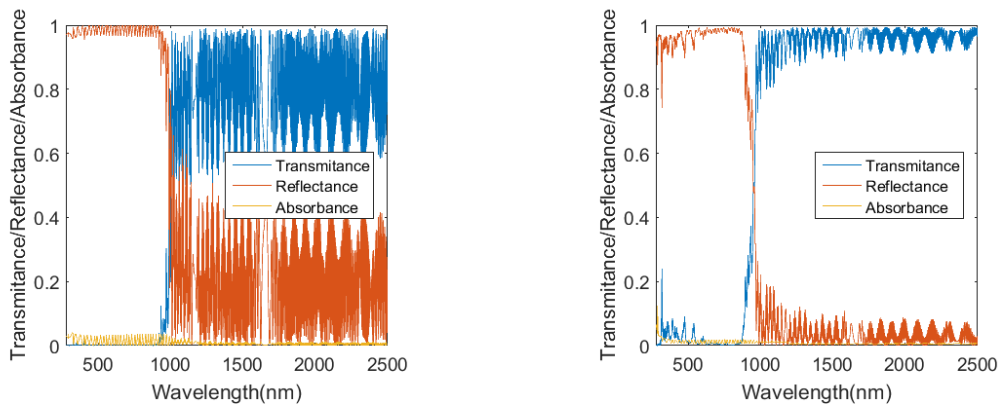
6.2. Implementation of the Transfer Matrix Method

transmittance in a spectrometer, maybe it is not possible to catch all the oscillations anyway as some spectrometers give the transmittance as an average in some interval, and the measured transmittance becomes more smooth without the large oscillations.

Furthermore, it is noticed that absorbance is present in the entire wavelength interval from 280-2500nm due to the non-zero imaginary part of the refractive index of MgF_2 as seen in Fig. 6.1b, but its values are small compared to the transmittance and reflectance.

To see the difference between s- and p polarization, the transmittance, reflectance, and absorbance are calculated for both polarizations and are seen in Fig. 6.3. The two figures have in common that band gaps exist for wavelengths below 900 nm, but the band gap is complete for s polarization while non-negligible transmittance occurs below 600 nm for p polarization. However, at wavelengths above 900 nm huge oscillations occur for s polarization while the oscillations are much smaller for p polarization. The Brewster angle from Eq. (2.18) for the interface between Si_3N_4 and SiO_2 is 36° and in Si_3N_4 the propagating angle for wavelengths above 900 nm is 20° , thus relatively close to the Brewster angle giving rise to the small reflectance and small oscillations.

Even it is possible to split the transmittance, reflectance, and absorbance into s- and p polarizations, all further figures will consider the average of the two polarizations as sunlight consists of a mixture of these two.



(a) transmittance, reflectance, and absorbance for s polarization.

(b) transmittance, reflectance, and absorbance for p polarization.

Figure 6.3: transmittance, reflectance, and absorbance for s- and p polarization for the initial guess consisting of 162 layers.

For the second method of choosing the initial guess from Sec. 5.1 it is found that the optimal structure again results in 10 blocks with 8 unit cells in each. The thicknesses of the blocks are seen in Table 6.2, and are almost the same as for the first initial guess in Table 6.1. By comparing the tables it is found that the maximal difference in thickness is about 2nm occurring in block 2 for Si_3N_4 . When the transmittance, reflectance, and absorbance are calculated with this initial guess, they are almost the same as in Fig. 6.2. In Sec. 6.4.2 it will be investigated whether the optimization converges to the same point given the two initial guesses, and in Sec. 6.4.3 if one of the methods is faster than the other.

The method of choosing the initial guess is written as a function in Matlab and depends on the types of beamsplitter, solar cell, thermoelectric efficiency and number of unit cells in each block. All these parameters are incorporated in `data` and the function is written

Block number	Thickness of Si ₃ N ₄ in nm	Thickness of SiO ₂ in nm
1	33	53
2	42	66
3	52	79
4	61	92
5	70	105
6	79	118
7	88	131
8	98	144
9	107	157
10	116	170

Table 6.2: Thicknesses of the materials for the second method of choosing the initial guess. All the blocks consist of 8 unit cells.

as

$$\text{function [Astart,N,lambda_step,lambda_cut,eff] = initial_guess_function(data),} \quad (6.3)$$

where `Astart` is the initial guess stored in a vector, `N=length(Astart)` is the number of layers, `lambda_step` is the band gap size for the individual blocks, `lambda_cut` is the cut off wavelengths of the beamsplitter and `eff` is the solar cell efficiency η_{solar} from Eq. (3.8). The Matlab code for `initial_guess_function` is found in [30].

6.3 Implementation and overview of the Main Program in Matlab

The `trans_ref_function` explained in the previous section calculates the transmittance, reflectance, and absorbance given some thicknesses `A` and `data`. In this short section a function calculating the efficiency is implemented and an overview of the Matlab program is presented.

From Eq. 4.20 the efficiency of the hybrid system depends on the transmittance and reflectance and is written as the following function in Matlab.

$$\text{function [eta] = eta_function(A,data),} \quad (6.4)$$

where the `eta_function` calculates `eta` from Eq. 4.20 by calling the `trans_ref_function` and can be found in [30]. The efficiency is to be optimized and is called by one of the three optimization functions: Exact line search, backtracking line search or bounded Nelder-Mead, where all the thicknesses are bounded to be non-negative. By a coordinate transformation the bounded problem is turned into an unbounded optimization problem solved by the unbounded Nelder-Mead method as explained in Sec. 5.2.2. The implementation of the optimization methods from chapter 5 is basically just to write the methods as Matlab functions, and will not be further explained here. A main program is written in Matlab to perform the optimization and an overview of the program is illustrated in Fig. 6.4. The program is found as `MAIN_FILE` in [30]. When running the program it has to be specified which transfer matrix method and which optimization method to apply.

The general flow of the main program is first to specify `data` which contains all the relevant input parameters. From `data` an initial guess is constructed, which is used to calculate the transmittance and reflectance, which is again used to calculate the efficiency belonging to the initial guess. The optimization methods optimize the efficiency and return the

6.4. Solution of the Optimization Problem

optimal thicknesses and optimal efficiency as indicated by the red arrows in Fig. 6.4, and the optimal thicknesses are used to calculate the optimal transmittance, reflectance, and absorbance as indicated by the blue arrow. The result is independent of the transfer matrix method but whether it depends on the optimization method will be examined in Sec. 6.4.3.

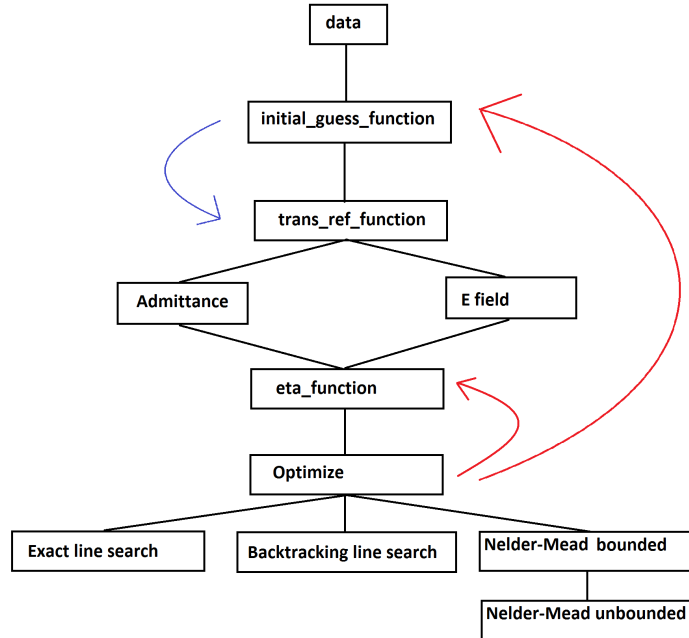


Figure 6.4: Overview of the Matlab code. *data* is given as input and an initial guess is constructed and used to calculate the transmittance, reflectance and efficiency, which is optimized using one of the three optimization methods. The optimization returns optimized thicknesses and efficiency as indicated by the red arrows, while the optimized transmittance, reflectance, and absorbance are calculated from these thicknesses as indicated by the blue arrow. Code available from [30].

6.4 Solution of the Optimization Problem

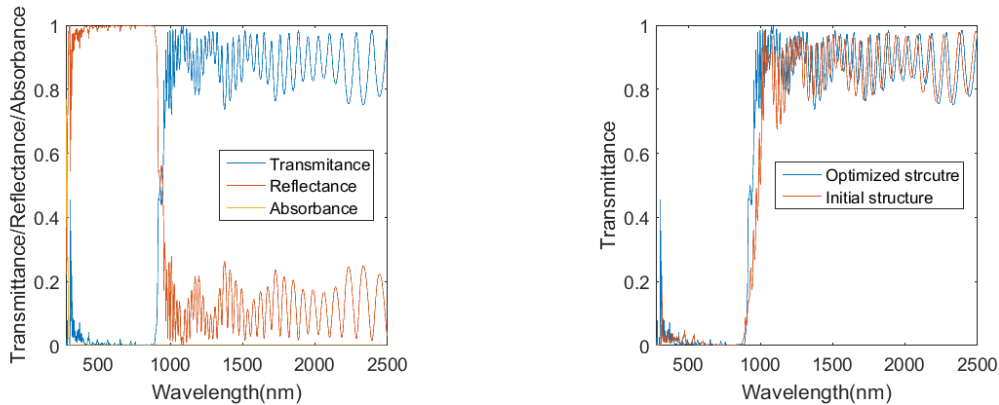
With the three optimization methods explained in Sec. 5.2 this section considers the implementation and results of the methods. First the optimized structure is compared to the initial one to assess the quality of the optimization process. As seen in the tables 6.1 and 6.2 the two initial guesses are close to each other, and it is therefore examined whether the methods converge to the same point for the two initial guesses. Then the three optimizations methods are compared based on their performance and time consumption. As mentioned in chapter 4 the efficiency of the thermoelectric element is chosen to be 4% or 8%. The principles of solving the optimization problem does not depend on this efficiency, and in this section it has been chosen to apply $\eta_{TE} = 4\%$. In chapter 7 it is studied how η_{TE} influences the total efficiency of the hybrid system.

6.4.1 Comparison of Initial and Optimized Structure

In this subsection the transmittance, reflectance, and absorbance belonging to the optimized structure are compared to the same quantities for the initial structure and the improvement during the optimization process is assessed.

First the Nelder-Mead method is applied and as mentioned in Sec. 5.2.2 the convergence of the method is not proved in general, and using the original built-in Nelder-Mead function no convergence is found. The algorithm is called `fminsearch` in Matlab and is found by typing `fminsearch` in a Matlab document, right click and open `fminsearch`. By changing the stopping criteria to the one in Eq. (5.16) the algorithm is found to converge, and the modified algorithm is found as `fminsearch2` in [30]. Setting $\varepsilon = 10^{-4}$ as the stopping criteria and applying the first initial guess where 162 layers are present gives the transmittance, reflectance, and absorbance in Fig. 6.5a where the incident angle is 45° which will be the case for all figures in this section.

To assess whether the quantities for the optimized structure is improved compared to those for the initial structure in Fig. 6.2, the transmittance for the two structures are plotted in the same figure in Fig. 6.5b. From this figure it is clear that the transmittance for the optimized structure is improved compared to the initial one as the cut off is sharper and the optimized transmittance is more close to the ideal transmittance in Fig. 1.3a. Below the band gap wavelength at 900 nm the transmittance is almost identically zero as in the ideal transmittance, but above 900 nm oscillations due to the glass layer cause that the transmittance is not totally ideal. A way to avoid this problem could be to deposit some layers serving as antireflection coating at the backside of the glass layer, where the thicknesses and refractive indices of the layers are optimized to reduce the reflectance. As explained in Sec. 6.2.1 the transmittance is now calculated where the glass thickness



(a) transmittance, reflectance, and absorbance for the optimized structure using the Nelder-Mead method with the first initial guess.

(b) Transmittance for the initial and final structure.

Figure 6.5: Comparison of transmittance for the initial and optimized structure when 162 layers are present.

is only $2.5\mu\text{m}$. This is done in Fig. 6.5 where the oscillations above 900nm are smaller compared to Fig. 6.2 and are sinusoidal. To calculate the efficiency of the thermoelectric element it is necessary to integrate the transmittance from 900-2500 nm, thus in the range where the oscillations are found. It is assumed that the large oscillations in Fig. 6.2 with 1 mm glass have the same average as the smaller oscillations in Fig. 6.5a with $2.5\mu\text{m}$ glass. The values of their integrals are thus assumed to be equal, and all the calculations are therefore performed when the glass thickness is $2.5\mu\text{m}$.

6.4. Solution of the Optimization Problem

After the optimization process the block structure from the initial guess is dissolved as it is no longer assumed that any thicknesses are the same. Hence the function to optimize is mapping from a subset of \mathbb{R}^{162} into the real positive numbers. The layer thicknesses for the optimized structure is changed compared to the initial structure as seen in Fig. 6.6, where the block structure for the initial guess is illustrated by the two staircases in blue and black. The optimized thicknesses in green and red are distributed around the staircases, as some thicknesses increase while others decrease. The lower staircase is the thicknesses of Si_3N_4 as material 1, while the upper staircase is for SiO_2 as material 2. The slopes of the staircases are different as they are quarter wave layers whose thicknesses are given by $a_i = \lambda_0 / (4n_i \cos \theta_i)$ for $i = \{1, 2\}$. Higher layer number corresponds to larger wavelength, hence the slope of the staircase is proportional to $1 / (n_i \cos \theta_i)$, and with the refractive indices from Fig. 6.1a it is found that $n_1 \cos \theta_1 \approx 1.5n_2 \cos \theta_2$, thus the slope of the upper staircase is approximately 1.5 times the slope of the lower staircase as seen in Fig. 6.6. It

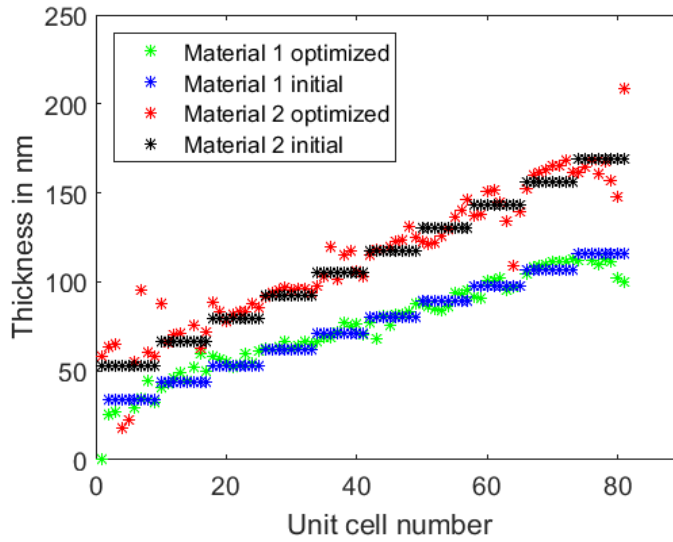


Figure 6.6: Thicknesses of all the layers for the initial and optimized structure. The initial structure consists of 10 blocks as seen by the staircases, while the optimized thicknesses are distributed around them. Material 1 is Si_3N_4 and material 2 is SiO_2 , but the first layer of material 1 is MgF_2

is found that the front layer of MgF_2 almost disappears during the optimization process, as seen by the first green point in the figure which corresponds to a thickness of 0.03nm, and the average change in thickness between the initial and optimized structure is found to be 6.3 nm. The reason for adding the front layer of MgF_2 was to reduce reflection from the front of the beamsplitter, because the real part of the refractive index for MgF_2 is smaller than that of SiO_2 as seen in Fig. 6.1a. But the refractive index of MgF_2 has an increasing imaginary part whereas SiO_2 has no imaginary part, as seen in Fig. 6.1b, and it turns out that the effect of smaller real part is cancelled out by the higher imaginary part and the optimized layer thickness of MgF_2 is found to be 0.03nm, thus extremely close to the lower bound at 0.

Applying the same optimization method with the second initial guess results in transmittance, reflectance, and absorbance very similar to Fig. 6.5a and the next subsection examines whether the optimized thicknesses for the two initial guesses are the same.

6.4.2 Test of Convergence of the two Initial Guesses

In this subsection it is examined whether the two initial guesses converge to the same point.

The transmittance, reflectance, and absorbance of the optimized structure for the first initial guess was seen in Fig. 6.5a and the optimized thicknesses seen as the red and green points in Fig. 6.6. The thicknesses are also calculated for the second initial guess, and is found to be different from the first initial guess, showing that the two initial guesses converge to different points. The optimized layer thicknesses for the two methods are seen in Fig. 6.7, where the green and blue points are the optimized thicknesses for Si_3N_4 as material 1, and the red and black points are for SiO_2 as material 2. The deviation for the two guesses is small for material 1, as all the green and blue points are close to each other, while the red and black points are more spaced. For the very last layer of material SiO_2 the difference is remarkable, as it is found to be 208 nm for the first initial guess and only 119 nm for the second guess. Besides the last layer, the difference in optimized layer difference is found to be small, as the difference exceeds $\pm 10\text{nm}$ in only 20 of 162 cases and the mean in -0.92nm . The difference in the two initial guesses is small and it is found that the difference in optimized thicknesses are greater than for the initial guesses but inside an acceptable difference, as the transmittance, reflectance, and absorbance corresponding to the two optimized structures are very similar. Hence two different local minima of the function f is found given the two different initial guesses, but the minima are relatively close to each other and have approximately the same function values which will be elaborated in the next subsection.

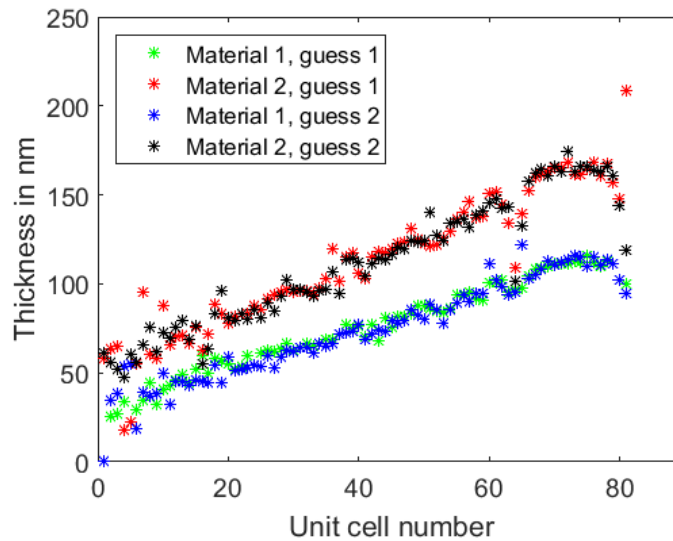


Figure 6.7: Layer thicknesses for the optimized structures using the two initial guesses. Material 1 is Si_3N_4 and material 2 is SiO_2 .

The same is done for the two gradient methods, and it is found that the two initial guesses converge to points closer to each other compared to the Nelder-Mead method. For the exact line search, the maximal difference between the two optimized points is 1.4nm, and the mean is 0.08nm, and for backtracking the numbers are 1.4nm and 0.06nm. The fact that the optimization processes given the two initial guesses converge to points close to each other and with approximately same function values indicates a robustness of the optimization processes. It is thus concluded that the two initial guesses converge to points

acceptable close to each other.

6.4.3 Comparison of the Optimization Methods

In this subsection a comparison of the three optimization methods based on their performance and time consumption is found. Firstly the performance is analysed for the Nelder-Mead method, and the gradient methods are compared to this performance.

As explained in Sec. 5.2.2 a new best point is found in every iteration of the Nelder-Mead method, see e.g Lemma 3.3 in [14], thus the function $f = -\eta_{\text{hybrid}}$ is a decreasing sequence implying that the total efficiency of the hybrid system is an increasing sequence. By some additions to the built-in Matlab function `fminsearch` it is possible to get the efficiency after each iteration which is seen in Fig. 6.8 plotted against the number of function calls for the first initial guess. The efficiency is 46.76% for the initial guess and increases to 47.57% for the optimized structure, hence an improvement of 0.81 percentage points is achieved during the optimization process. The first point in the figure is the initial guess calculated after just 1 function call. Setting up the initial simplex takes additional N function calls, thus the next point occurs after 163 function calls. Then the initial simplex is reflected many times without a further increase in the best point until an expansion is found after 654 function calls implying a desired increase in the efficiency. From 1000-3000 function calls the efficiency is almost linearly increasing and flattens out after approximately 3000 function calls until the stopping criterion is finally met after 5055 function calls and the algorithm stops. The same is done for the second initial guess and the efficiency is nearly the same as in Fig. 6.8, but terminates after 5031 function calls with an efficiency for the optimized structure of 47.54%. Hence it is found that the two initial guesses give almost the same result where the first initial guess is slightly better and is therefore applied from now on.

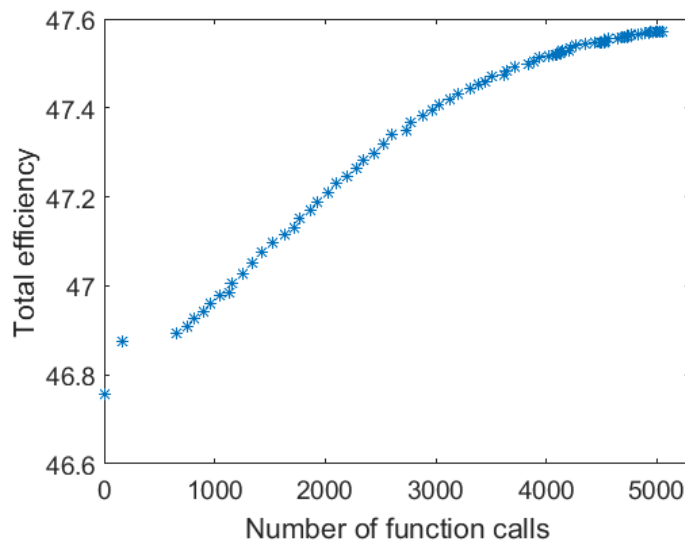


Figure 6.8: Total efficiency of the hybrid system plotted against the number of function calls in the Nelder-Mead method for the first initial guess.

The optimization methods have different stopping criteria, the gradient methods stop when $\|\vec{\nabla} f(\vec{x}_k)\|_2 < \tilde{\varepsilon}$ and the Nelder-Mead method stops when $|f(\mathbf{V}_1^{k+1}) - f(\mathbf{V}_1^k)| < \varepsilon$ from Eq. (5.16) where $f(\mathbf{V}_1)$ is the function value for the best point in a given iteration. As the Nelder-Mead method is derivative-free the gradient is not calculated, and can thus not

be used to compare the methods. The fact that the norm of the gradient becomes small implies that the difference in function values decreases too, thus an idea is to reformulate the stopping criteria for the gradient methods as $|f(\vec{x}_{k+1}) - f(\vec{x}_k)| < \varepsilon$, where ε is the same threshold as for the Nelder-Mead method, thus the methods should be comparable. But as mentioned in Sec. 5.2.2 the iteration number k can not be compared for the two methods. For the gradient methods, k is updated after every step as seen in point (iii) in Algorithm 5.1, thus after calculation of the gradient and determination of the step length. For the Nelder-Mead method k is updated when a new best point \mathbf{V}_1 is found, and this can take many reflections to achieve, especially when many parameters are present. Another way to compare the methods is to force them to use the same number of function calls and compare the output. The reason of using function calls instead of computational time to compare the methods is that the latter strongly depends on which computer is used while the number of function calls is the same for all computers. It was found that the Nelder-Mead method for the first initial guess used 5055 function calls before termination. The gradient methods are therefore run without other criteria than to stop when the number of function calls exceeds 5055. For the backtracking line search method with $\mu_{start} = 20, \alpha = 0.01$ and $\beta = 0.6$ the efficiency is seen in Fig. 6.9a and increases from 46.76% to 46.87%, thus only 0.11 percentage points. Notice that the efficiency is still increasing after 5000 function calls, and the difference in function value between the last and second last point is found to $3.2 \cdot 10^{-3} = 32 \cdot \varepsilon$, hence if it was to terminate after its original condition many more function calls would probably be needed.

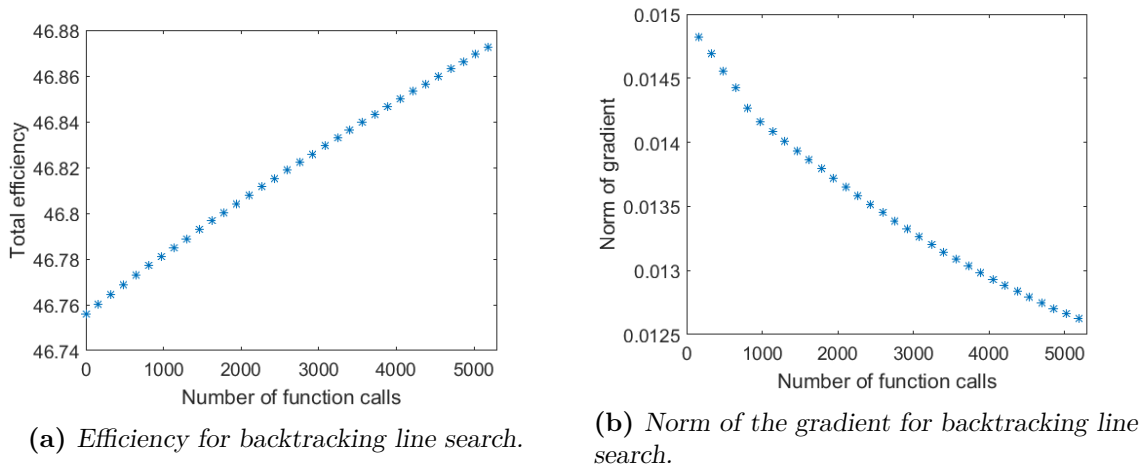


Figure 6.9: Performance of backtracking line search.

The optimization process has not gotten the time to finish, which also explains the small difference in optimized thicknesses for the two initial guesses. It was found that the step length μ_{start} satisfied the Wolfe conditions in every iteration, thus a constant step length of 20 is taken in every iteration. Using the Nelder-Mead method the efficiency increases by 0.81 percentage points thus approximately 7.4 times more than the increase achieved by the backtracking method.

As mentioned, the original stopping criteria in the backtracking method is that the norm of the gradient should be smaller than some threshold value $\tilde{\varepsilon}$. The norm of the gradient is calculated in every iteration and is seen in Fig. 6.9b plotted on the same axis as in Fig. 6.9a and is strictly decreasing in every iteration. The sequence seems to converge to zero as it should according to Sec. 5.2.1 and [29] thus the original stopping criteria makes sense.

6.4. Solution of the Optimization Problem

The norm of the gradient converges to zero very slowly, as it only decreases approximately 15% compared to its initial value using 5000 function calls, thus supporting the fact that backtracking line search is slow compared to the Nelder-Mead method.

The same is done for the exact line search method and its efficiency and gradient norm are seen in Fig. 6.10 and are almost identical to Fig. 6.9. The norm of the gradient is again a strictly decreasing sequence, hence the theorem about its convergence from Sec. 5.2.1 and [9] is satisfied. In addition it is denoted that the norm of the gradient in the final iteration is almost the same as for the final iteration using backtracking line search. The efficiency increases from 46.76% to 46.87%, thus exactly the same as for backtracking line search and much less than the Nelder-Mead method, and like for backtracking the efficiency is still increasing after 5000 function calls and the difference in function values between the last and second last point is again found to be $32 \cdot \varepsilon$. For the exact line search the gradient is calculated in every iteration and it is searched for a minimum in that direction using $N_{step} = 10$ steps at a time, and it is found that it is not necessary to extend the search direction in any of the iterations. Thus a minimum of $f(\vec{x}_k - \mu \vec{\nabla} f(\vec{x}_k))$ occurs for $\mu < 10$ in every iteration.

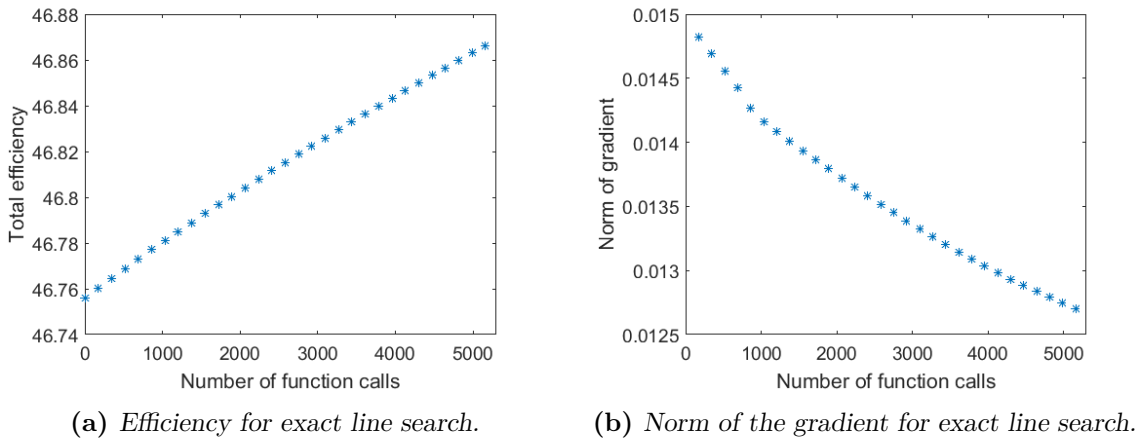


Figure 6.10: Performance of exact line search.

Hence for the considered optimization it is found that the performance of the Nelder-Mead method is approximately 7.4 times better than for the two gradient methods, and that the performance of backtracking line search and exact line search is about the same.

In [6] ten different optimization methods, including the Nelder-Mead method and the gradient method, are tested on their ability to produce three different transmittance curves. In one of them the goal is to reduce the reflectance to zero in the spectral region $7.7\mu\text{m} < \lambda < 12.2\mu\text{m}$ for light incident perpendicular on a structure of 21 layers consisting of two alternating materials with real refractive indices. The ten optimization methods are allowed to run equal time on the same computer, and their values of a merit function are compared, and it is found that the Nelder-Mead method is better than the gradient method. The merit function corresponds to the total efficiency optimized in this thesis, but in [6] it is desired to achieve a low merit function value. The overall problem is very similar to the one studied in this thesis and confirms the result that the Nelder-Mead method is better than the gradient method. In [6] the merit function value of the initial guess is 10.58 and decreases to 1.28 for the Nelder-Mead method and to 2.81 for the gradient method. Due to the difference in the problems, and especially in the initial guesses, the improvements of the merit function values are not comparable to those found here.

7. Results

With all the relevant theory derived in chapter 2 to 5 and the optimization program explained and tested in chapter 6, this chapter considers the important results in the thesis. In the previous chapter it was found that the two initial guesses converge to points acceptable close to each other, and that the Nelder-Mead method is better than the two gradient methods. Hence the Nelder-Mead method with the first initial guess is applied in this chapter to study the efficiency as a function of number of layers with fixed angle, and the efficiency as a function of angle with fixed number of layers. In addition the effect of the imaginary part of the refractive index for MgF_2 is studied. In Sec. 7.1 all this is done for an ideal solar cell as in the previous chapter, while Sec. 7.2 and 7.3 examines the efficiencies for a microcrystalline and amorphous solar cell. This chapter contains results presented in figures, while the thicknesses of the optimized beamsplitter are found in tables in Appendix A, and these thicknesses are to be used when fabricating the beamsplitter.

7.1 Results for an Ideal Solar Cell

This section considers the results for the ideal solar cell studied so far where the efficiency of a single solar cell with no beamsplitter is 46.76%. The section examines how the efficiency depends on number of layers, incident angle and the refractive index of MgF_2 .

7.1.1 Efficiency as a Function of Number of Layers

In this subsection the connection between the total efficiency and the number of layers is studied, where the incident angle is kept constant at 45° , and it is first chosen to apply $\eta_{TE} = 4\%$.

Until now a structure of 162 layers has been considered, as it was stated to be the optimal number of layers. As mentioned in Sec. 6.2.1 the structure consists of 10 blocks with 8 unit cells in each block, and varying the number of unit cells in each block implies a change in the number of layers. It is chosen to consider 2, 4, 6 and 10 unit cells in each block, which corresponds to a structure of 42, 82, 122 and 202 layers. The same optimization procedure is performed for each of them, and their optimized transmittance, reflectance, and absorbance are seen in Fig. 7.1, while the structure of 162 layers was seen in Fig. 6.5a. From the figures it is clear that the transmittance gets more ideal when the beamsplitter consists of more layers, as the cut off is more sharp and the band gap becomes more complete.

The total efficiency is calculated when the number of unit cells in each block ranges from 1 to 10, corresponding to a layer range of 22 to 202, and is seen in Fig. 7.2. If the beamsplitter only consists of 22 layers the efficiency is only 32% but increases to 40% when 20 extra layers are added. This tendency only applies when few layers are present, as the efficiency flattens out around 142 layers, and only a small improvement can be achieved by adding extra layers. The black horizontal line is the efficiency of a single solar cell when all the light from 280-2500nm is directed onto it, and was found to be 46.76% as mentioned in Sec. 3.1.1. The red horizontal line at 48.01% is the theoretical efficiency if a perfect beamsplitter is applied, which gives an ideal transmittance where all the light below 900 nm is directed to the solar cell and all light above 900 nm to the beamsplitter. The difference in efficiency between a perfect beamsplitter a single solar cell is thus 1.25 percentage point.

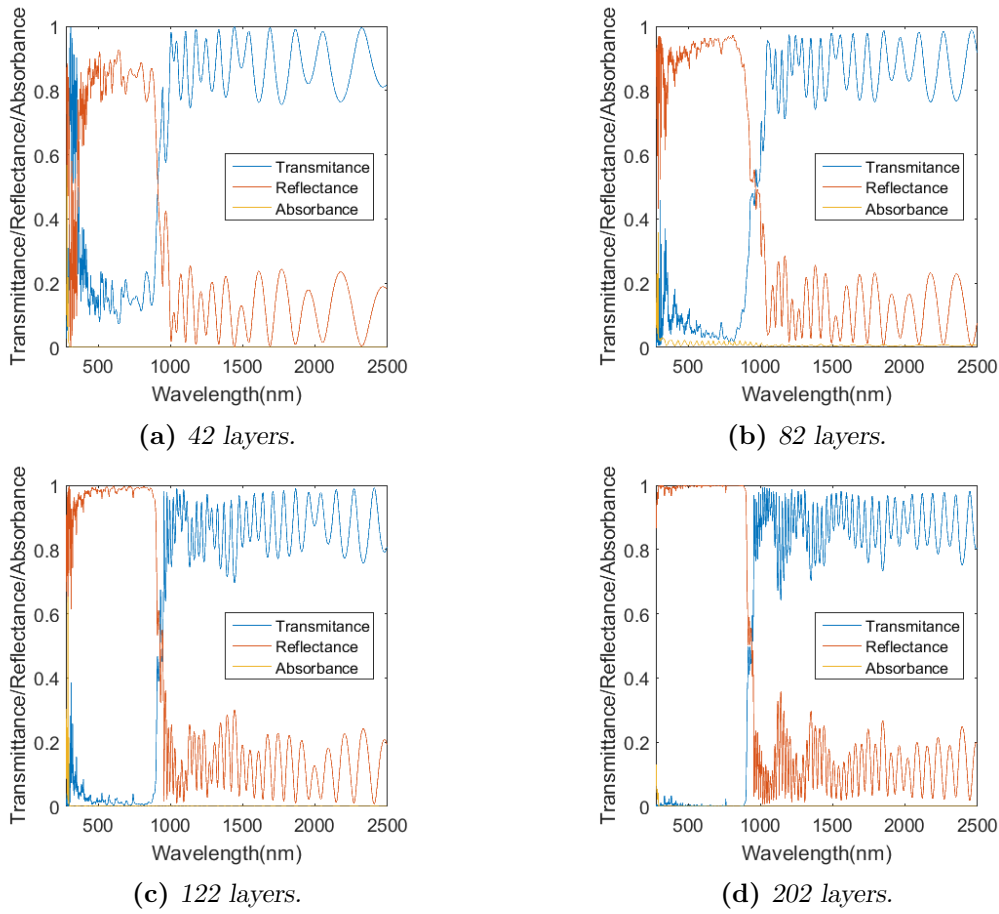


Figure 7.1: *transmittance, reflectance, and absorbance for optimized structures consisting of 42, 82, 122 and 202 layers for an ideal solar cell. The transmittance gets more ideal when more layers are applied.*

A necessary condition for constructing the beamsplitter must be that the efficiency of the hybrid system exceeds that of a single solar cell, which is seen to be satisfied if the beamsplitter consists of at least 122 layers giving an efficiency of 47.06%. Adding 80 extra layers the efficiency increases to 47.71%, thus 0.95 percentage points higher than for a single solar cell and a relative improvement of 2.0% compared to a single solar cell is achieved. It is not possible to have a perfect beamsplitter but it is found that if 202 layers are used the efficiency is only 0.3 percentage point below that of a perfect beamsplitter. As seen in Fig. 7.1d the transmittance is almost identically zero for wavelengths below 900 nm and the cut off is very sharp, but the oscillations above 900 nm imply that the transmittance is not totally ideal.

When manufacturing the beamsplitter, such a graph is extremely important as it shows how many layers are necessary to achieve a certain total efficiency, and how close it is possible to reach the theoretical limit. If, for example, it only is possible to construct a beamsplitter consisting of 50 layers, the efficiency of the hybrid system gets lower than that of a single solar cell, and it is not worth constructing it. It is remembered that these efficiencies are for an ideal solar cell and this graph is therefore useless in practice, but corresponding graphs are found for real solar cells in the next two sections and they can be used in practice.

If the efficiency of the thermoelectric element increases, it implies an increase in the total

7.1. Results for an Ideal Solar Cell

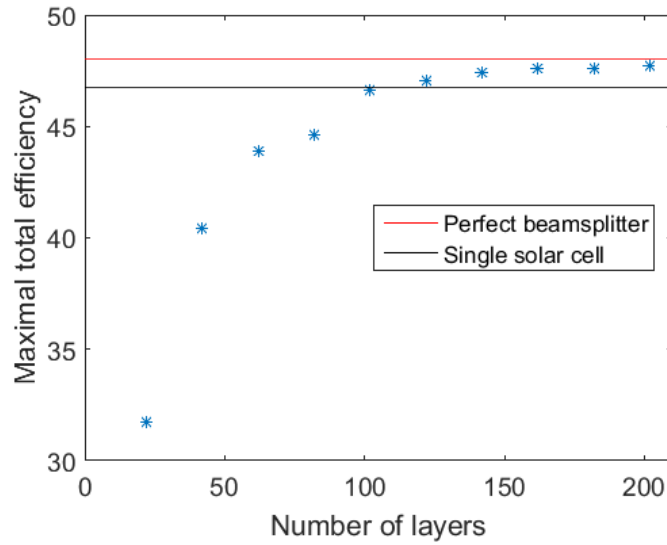
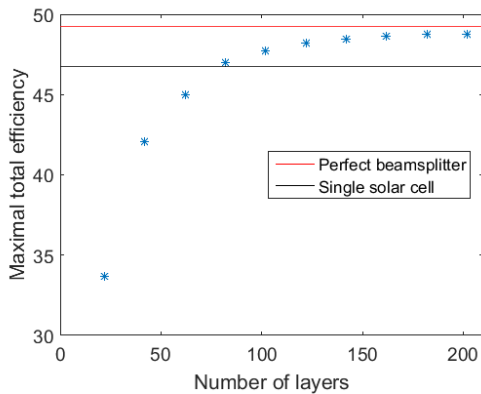
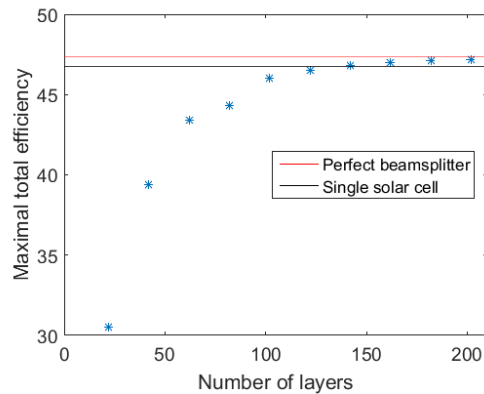


Figure 7.2: Total efficiency as a function of number of layers in the beamsplitter for an ideal solar cell with $\eta_{TE} = 4\%$. The black horizontal line at 46.76% is the efficiency of a single cell, and for the beamsplitter to have an eligibility it must consist of at least 122 layers. The relative improvement compared to a single solar cell is 2.0%, and the red horizontal line at 48.01% is the efficiency if a perfect beamsplitter is applied.

efficiency as well. Setting $\eta_{TE} = 8\%$ and performing the optimization leads to transmittances very similar to those in Fig. 7.1, and the efficiency as a function of the number of layers is seen in Fig. 7.3a. The shape of the graph is the same as in Fig. 7.2, the black line is unchanged, the red line is increased to 49.25% and the efficiency is generally shifted upwards due to the increased η_{TE} . Here the necessary condition is satisfied when the beamsplitter consists of 82 layers, instead of 122 layers, and if 202 layers are present the efficiency becomes 48.76%, thus 2 percentage points higher than for a single solar cell and the relative improvement becomes 4.3%.



(a) Efficiency as a function of number of layers for $\eta_{TE} = 8\%$. 82 layers are required to satisfy the necessary condition and the largest relative improvement compared to a single solar cell is 4.3%.



(b) Efficiency as a function of number of layers for $\eta_{TE} = 2\%$. 142 layers are required to satisfy the necessary condition and the largest relative improvement compared to a single solar cell is 0.8%.

Figure 7.3: Efficiency as a function of number of layers for $\eta_{TE} = 8\%$ and 2%.

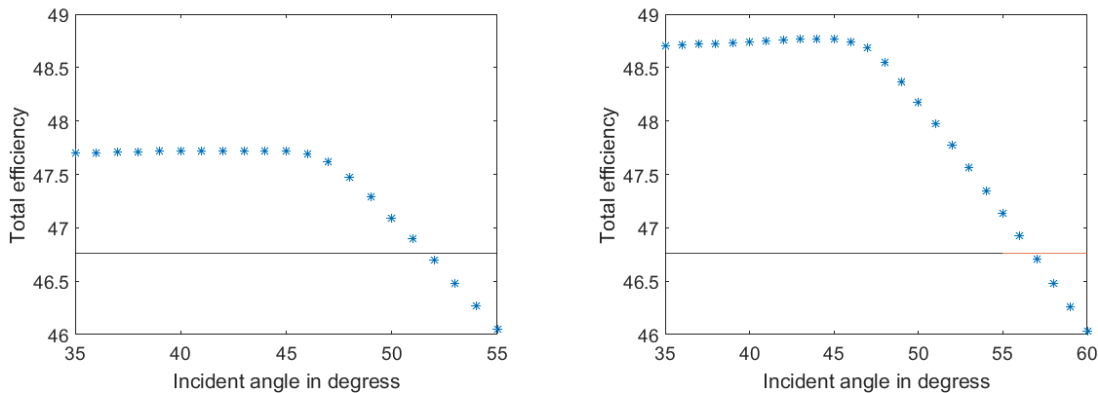
The same is done for $\eta_{TE} = 2\%$, and its efficiency as function of number of layers is seen in Fig. 7.3b. The beamsplitter here has to consist of 142 layers before the necessary condition is satisfied, and when 202 layers are present the efficiency is 47.18%, thus less than 0.5 percentage points higher than for a single solar cell and the relative improvement is only 0.8%.

From these figures it is seen that the number of layers has a great influence on the total efficiency, and if the beamsplitter consists of too few layers, it is not worth constructing it. But adding many extra layers does not imply an increase in the efficiency, as it flattens out when many layers are present. If a beamsplitter consists of 200 layers, it is better to increase the efficiency of the thermoelectric element than to add more layers.

7.1.2 Efficiency as a Function of Incident Angle

In this subsection the connection between total efficiency and incident angle is studied, where the number of layers is kept constant at 202 as it resulted in the highest efficiency as seen in Fig. 7.2 and 7.3.

Until now an incident angle of 45° has been applied in the optimization problem and all the figures, and for 202 layers the optimized transmittance, reflectance, and absorbance was seen in Fig. 7.1d. As explained in the introduction all the incident angles are not 45° , but varies in an interval centered at 45° . The beamsplitter is optimized to an incident angle of 45° , and to study its angle sensitivity it is chosen to apply the optimized structure and calculate the efficiency when the angle varies from 35° - 55° . This is seen in Fig. 7.4a for $\eta_{TE} = 4\%$ and in Fig. 7.4b for $\eta_{TE} = 8\%$, and the black line in both figures is the efficiency of a single solar cell at 46.76%.



(a) Efficiency as a function of angle for an ideal solar cell with $\eta_{TE} = 4\%$. The critical angle is 52°

(b) Efficiency as a function of angle for an ideal solar cell with $\eta_{TE} = 8\%$. The critical angle is 57°

Figure 7.4: Efficiency as a function of angle for an ideal solar cell.

The efficiency is almost the same when the angles ranges from 35° - 45° and decreases rapidly for larger angles. It is found that the maximal efficiency actually occurs when the angle is 42° - 44° even the structure is optimized for 45° giving a cut off wavelength close to 900 nm. For a quarter wave structure the design wavelength is $\lambda_0 = 4an \cos \theta$ from Eq. (2.30), and when $\cos \theta$ is a decreasing function for $0^\circ < \theta < 180^\circ$ it is found that a smaller angle results in a higher design wavelength implying a higher cut off wavelength. The fact that the positions of the band gaps depend on the incident angle was also observed in Fig. 2.3 and 2.12. Hence when the angle is smaller than 45° the cut off wavelength is higher than 900 nm and in principle, too much light is directed onto the solar cell, as it cannot

7.1. Results for an Ideal Solar Cell

utilize any wavelengths above 900 nm. However, even for the optimized structure the cut off is not perfectly sharp and it is possible that some wavelengths below 900 nm are directed onto the thermoelectric element instead of the solar cell, but increasing the cut off wavelength decreases that possibility and actually slightly increases the total efficiency. On the other hand, when the angle exceeds 45° the cut off wavelength becomes smaller than 900 nm, and too little light is directed onto the solar cell. This is more critical because the efficiency of the solar cell is linearly increasing up to 900 nm, and a too low cut off implies that the wavelengths that are best for the solar cell are directed onto the thermoelectric element. Hence it is better for the cut off wavelength to be too high than too low, which is supported by Fig. 7.4. In the figures the efficiency of the thermoelectric element is 4% and 8%, respectively, and the figures show similar behaviour, but the efficiency is shifted upwards when $\eta_{TE} = 8\%$. As in the previous subsection the black line is the efficiency of a single solar cell, and to satisfy the necessary condition for the eligibility of the beamsplitter the efficiency of the hybrid system must exceed that of a single solar cell. When $\eta_{TE} = 4\%$ this is seen to be satisfied for angles smaller than or equal to 52° , as seen in Fig. 7.4a, but when $\eta_{TE} = 8\%$ the critical angle increases to 57° as seen in Fig. 7.4b. Notice that the x axis in the figures are different, for $\eta_{TE} = 4\%$ the angles varies from $35\text{-}55^\circ$ and the critical angle is found in that interval. Increasing η_{TE} to 8% and applying the same angle interval, no critical angle is found as the efficiency exceeds 46.76% for all the angles, and it has been necessary to extend the angle interval to $35\text{-}60^\circ$ in order to find the critical angle.

7.1.3 Effect of Imaginary Refractive Index of MgF_2

In this subsection the effect of the imaginary part of the refractive index for MgF_2 is studied.

Until now MgF_2 as material 3 has had a refractive index whose real and imaginary part are seen in Fig. 6.1. For the initial structure the thickness of MgF_2 was 58 nm, but as explained in Sec. 6.4.1 the optimization process almost removes the layer and its optimized thickness is found to be 0.03 nm as seen in Fig. 6.6. Hence the effect of smaller real part of the refractive index is overshadowed by its higher imaginary part. To study the effect of the imaginary part, it has been chosen to let the refractive index of the material be purely real, and solve the optimization problem in the same way as earlier. It is found that the optimized thickness of MgF_2 in this case becomes 113 nm as seen by the first green point in Fig. 7.5, hence the thickness is almost doubled instead of removed. The transmittance, reflectance, and absorbance for the optimized structure is almost identical to Fig. 6.5a where MgF_2 had an imaginary part. In that case the efficiency of the optimized structure was 47.57% which was found after 5055 function calls as seen in Fig. 6.8. Without the imaginary part the efficiency is found to be 47.59% after 3806 function calls.

The material with a real part like MgF_2 and no imaginary part does not exist naturally and must be fabricated artificially. It is found that the improvement of the efficiency of using such material is only 0.02 percentage points, hence it is not worthwhile trying to fabricate such a material.

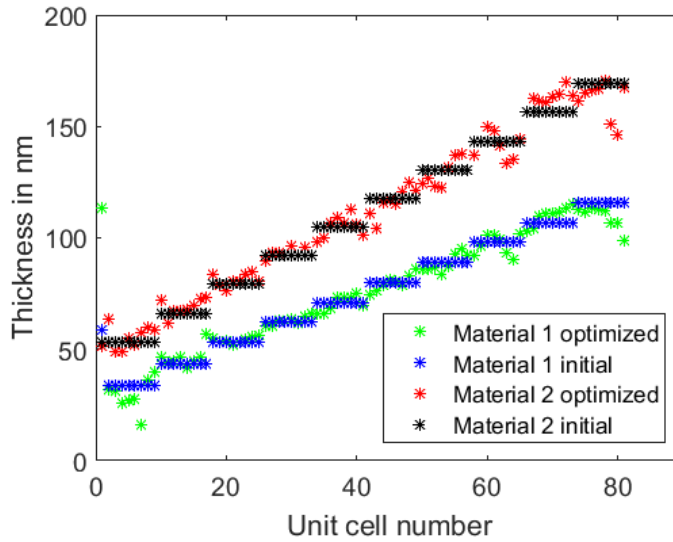


Figure 7.5: Thicknesses of all the layers for the initial and optimal structure for the ideal solar cell where the refractive index of MgF_2 is purely real. The optimized thickness for material 3 is 113 nm, where it was 0.03 nm in Fig. 6.6. Material 1 is Si_3N_4 and material 2 is SiO_2 , but the first layer of material 1 is MgF_2 .

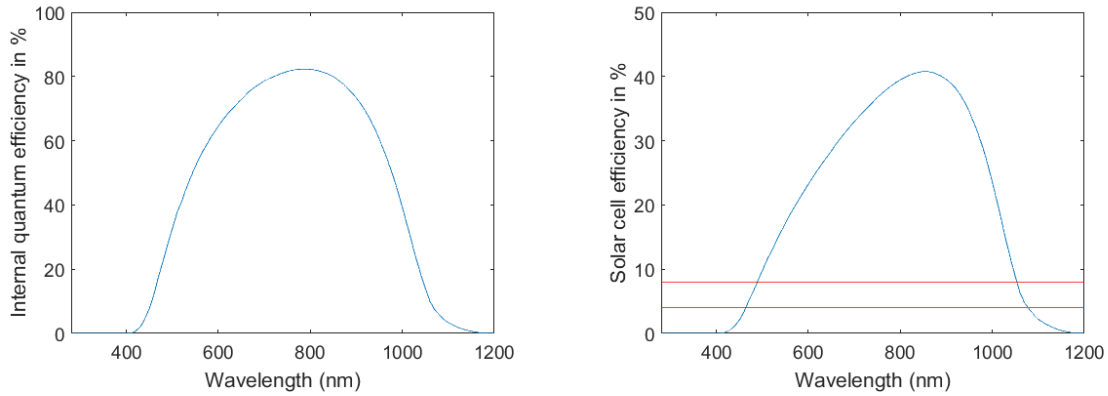
7.2 Results for a Microcrystalline Solar Cell

Until now only an ideal solar cell has been considered with an efficiency around 47%. No real solar cells have so high efficiency, in fact the best fabricated solar cells have efficiencies around 25%. [11] As explained in Sec. 3.2 limiting factors exist which strongly reduce the efficiency and one of these factors is the external quantum efficiency as shown in Fig. 3.4, which depends on the internal quantum efficiency IQE, the coverage factor $1 - A_c/A_{tot}$ and the total reflectance R . In general the efficiency depends on several more variables such as the concentration of donors and acceptors in the doped semiconductor, the diffusion lengths in the emitter and base layer and the mobility of electrons and holes. [34] The efficiency of real solar cells considered in the thesis is therefore simplified as it only takes the parameters mentioned in chapter 3 into account. The optimization process calculates the maximal efficiency of the hybrid system with the considered solar cell, and the principles in the optimization is independent of the solar cell type. If a specific solar cell with an efficiency different from those considered here is wanted in the hybrid system, it is possible to run the same optimization program, just with another input parameter for the solar cell efficiency.

For some chosen values of donor concentrations, diffusion lengths and mobilities the internal quantum efficiency is found from [11] and is seen in Fig. 7.6a, where the band gap wavelength is 1170 nm which is about the value for microcrystalline solar cells. [4] It is therefore chosen to apply the data in Fig. 7.6a for a microcrystalline solar cell. To find the external quantum efficiency $\text{EQE} = (1 - R)(1 - A_c/A_{tot})\text{IQE}$, values for the reflectance and coverage factor are needed, and have been chosen to be $R = 0.1$ and $A_c = 0$, hence the shadow effect of the contacts is neglected, and the external quantum efficiency becomes 90% of the internal quantum efficiency. Notice that R is chosen to be constant in the entire wavelength interval which indeed is a rough approximation.

The total efficiency of the solar cell as function of the wavelength also depends on the fill factor and is given in Eq. (3.8), where the fill factor has been set to 0.8. The efficiency

7.2. Results for a Microcrystalline Solar Cell



(a) Internal quantum efficiency for the considered microcrystalline solar cell with a band gap wavelength of 1170 nm. Data from [11].

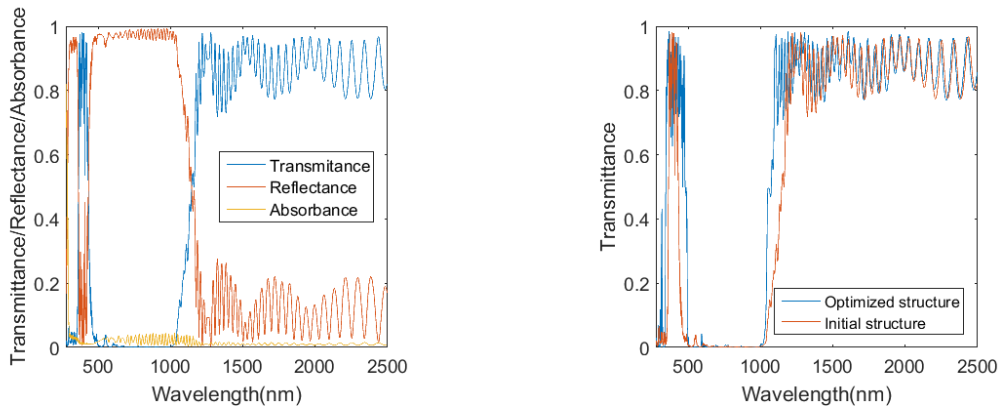
(b) Efficiency as function of wavelength for the considered microcrystalline solar cell. The ideal band gap for the beamsplitter is 464-1079 nm for $\eta_{TE} = 4\%$ and 489-1054 nm for $\eta_{TE} = 8\%$.

Figure 7.6: Data for the considered microcrystalline solar cell.

is seen in Fig. 7.6b and is found to have a maximum of 41% at 850 nm. The overall efficiency of the microcrystalline solar cell is found by integrating the efficiency in Fig. 7.6b multiplied by the solar spectrum and divided by the incident intensity, giving an efficiency of 17.47%. This efficiency corresponds to the 46.76% as the efficiency for the ideal solar cell, and the necessary condition for the hybrid system with the microcrystalline solar cell is that the total efficiency exceeds 17.47%.

The two red horizontal lines at 4% and 8% in Fig. 7.6b are the efficiencies of the thermoelectric element, and divide the wavelength interval from 300-1200 nm into three parts. For the short wavelengths the efficiency of the solar cell is smaller than that of the thermoelectric element, and in that region it is best to direct the light onto the thermoelectric element. This wavelength region was not present for the ideal solar cell as its efficiency as function of wavelength was given in Eq. (3.2) and is higher than η_{TE} for the small wavelengths. When the wavelength increases the solar cell efficiency increases as well and exceeds that of the thermoelectric element, why in that region it is best to direct the light onto the solar cell. For high wavelengths the solar cell efficiency decreases again and becomes smaller than the thermoelectric efficiency, and again it is best to direct the light onto the thermoelectric element. The ideal transmittance is illustrated in Fig. 1.3b in the introduction, and the ideal band gap is found to be 464-1079 nm for $\eta_{TE} = 4\%$ and 489-1054 nm for $\eta_{TE} = 8\%$.

With the efficiency given in Fig. 7.6b the next subject is to construct an appropriate initial guess where the transmittance is as close as possible to the ideal transmittance in Fig. 1.3b. Now the initial guess also depends on η_{TE} as it decides the ideal band gap, and in the following figures it has been chosen to apply $\eta_{TE} = 8\%$. The same method as in Sec. 6.2.1 is used to construct the initial guess which is found to consist of 9 blocks with 8 unit cells in each block implying 146 layers in total, where the front layer of MgF_2 has the thickness 102 nm. The transmittance, reflectance, and absorbance are calculated for the initial guess and are seen in Fig. 7.7a, where an almost complete band gap exists in the desired wavelength interval. It is noticed that absorbance is present in the entire wavelength interval due to the layer of MgF_2 with an imaginary part of the refractive index. It is desired to have a high transmittance for the wavelengths below 489 nm, but because of higher order band gaps this is difficult to achieve, and only the wavelengths



(a) transmittance, reflectance, and absorbance for the initial guess consisting of 146 layers for the microcrystalline solar cell.

(b) Transmittance for the initial and optimized structure consisting of 146 layers for the microcrystalline solar cell.

Figure 7.7: Comparison of transmittance for initial and optimized structure for the microcrystalline solar cell.

from approximately 360-420 nm are thus directed to the thermoelectric element where they contribute to the total efficiency. The higher order band gaps will be explained in details in Sec. 7.5.1. Most of the wavelengths from 280-350 nm are directed to the solar cell where they do not contribute at all to the efficiency, as it is zero in that interval as seen in Fig. 7.6b, and the energy is therefore converted to heat in the solar cell. The upper band gap edge is around 1054 nm and most of the wavelengths above that value are directed onto the thermoelectric element as desired, and the efficiency of the hybrid system for the initial guess is found to be 18.46%, thus almost 1 percentage point higher than a single solar cell. An optimized structure is found and the transmittance, reflectance, and absorbance calculated, and a comparison of transmittance for the initial and optimized structure is seen in Fig. 7.7b. The transmittance of the optimized structure is seen to be closer to the ideal one as both cut offs around 489 and 1054 nm are sharper. The efficiency for the optimized structure is found to be 19.17%, thus 0.71 percentage points higher than the initial guess and 1.7 percentage points higher than for a single solar cell, and the relative improvement compared to a single solar cell is 9.7%.

As in Sec. 6.4.1 the thicknesses for the optimized structure are compared to those for the initial guess as seen in Fig. 7.8. The thicknesses of the initial guess are seen by the staircases while the optimized thicknesses are distributed around them, and the average change in thickness between the initial and optimized structure is found to be 5.3 nm. The front layer of MgF_2 for the optimized structure is found to be 77 nm while it was 102 nm for the initial guess. This is remarkable as the front layer was totally removed for the ideal solar cell as seen in Fig. 6.6, but remains for the microcrystalline solar cell giving rise to a non-negligible absorbance for the optimized structure. Hence when the efficiency is around 17% instead of 47% it seems that the effect of smaller real part of the refractive index is not overshadowed by the imaginary part as was the case for the ideal solar cell.

The results in this section so far were calculated for a structure of 146 layers and an incident angle of 45° . As for the ideal solar cell, the efficiency is examined as a function of number of layers and incident angle, which is the subject for the next two subsections.

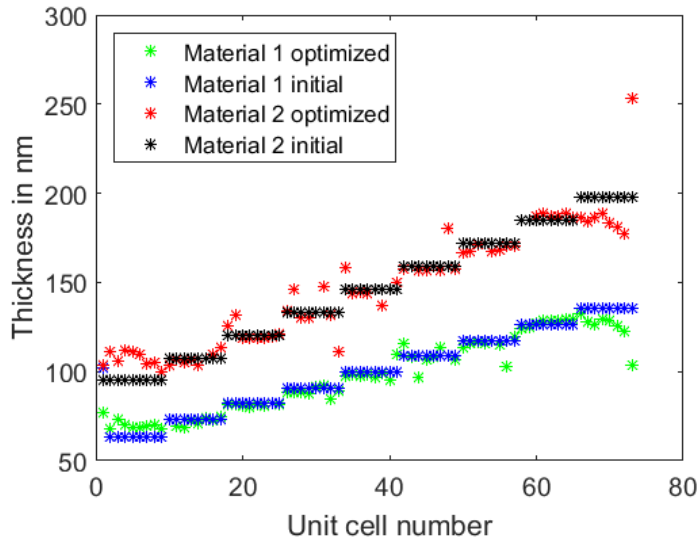


Figure 7.8: Thicknesses of all the layers for the initial and optimized structure consisting of 146 layers for a microcrystalline solar cell. The initial structure consists of 9 blocks as seen by the staircases, while the optimized thicknesses are distributed around them. The average change in thickness between the initial and optimized structure is 5.3 nm. Material 1 is Si_3N_4 and material 2 is SiO_2 , but the first layer of material 1 is MgF_2 .

7.2.1 Efficiency as a Function of Number of Layers

This section is an analogy to Sec. 7.1.1 and examines how the efficiency depends on the number of layers when the incident angle is kept constant at 45° , and it is first chosen to apply $\eta_{TE} = 8\%$ as in the previous section.

As seen in Fig. 7.1 where an ideal solar cell was considered the transmittance, reflectance, and absorbance are strongly dependent on the number of layers. This is also the case for a microcrystalline solar cell, and it is chosen to consider structures consisting of 20, 56, 128 and 164 layers whose transmittance, reflectance, and absorbance are seen in Fig. 7.9. The transmittance gets closer to the ideal one as more layers are present, but the improvement from 128 to 164 layers is not so significant.

The total efficiency of the hybrid system is calculated when the number of layers varies from 20 to 182 and is seen in Fig. 7.10a. As mentioned, the efficiency of a single solar cell is 17.47% and if a perfect beamsplitter is applied which gives the ideal transmittance, the efficiency of the hybrid system is found to be 20.23% and as earlier these two efficiencies are shown by the black and red horizontal line, respectively. The necessary condition for constructing the beamsplitter is that the efficiency of the hybrid system exceeds that of a single solar cell, which is seen to be satisfied using just 56 layers, where 82 layers were required for the ideal solar cell as seen in Fig. 7.3a. The sequence flattens out and is actually decreasing by 0.04% when the number of layers increases from 164 to 182. It is found that the transmittance, reflectance, and absorbance for structures consisting of 164 and 182 are almost identical, which indicates that the efficiency as a function of number of layers has converged. It is not reasonable that the efficiency decreases when more layers are available, and if the optimal structure really was found with 164 layers, the optimization should in principle find that the extra layers should have a thickness of 0. For all the different optimization processes the same value of $\varepsilon = 10^{-4}$ has been applied, and a way to finer optimize the structure is to let ε in some way depend on the number of parameters.

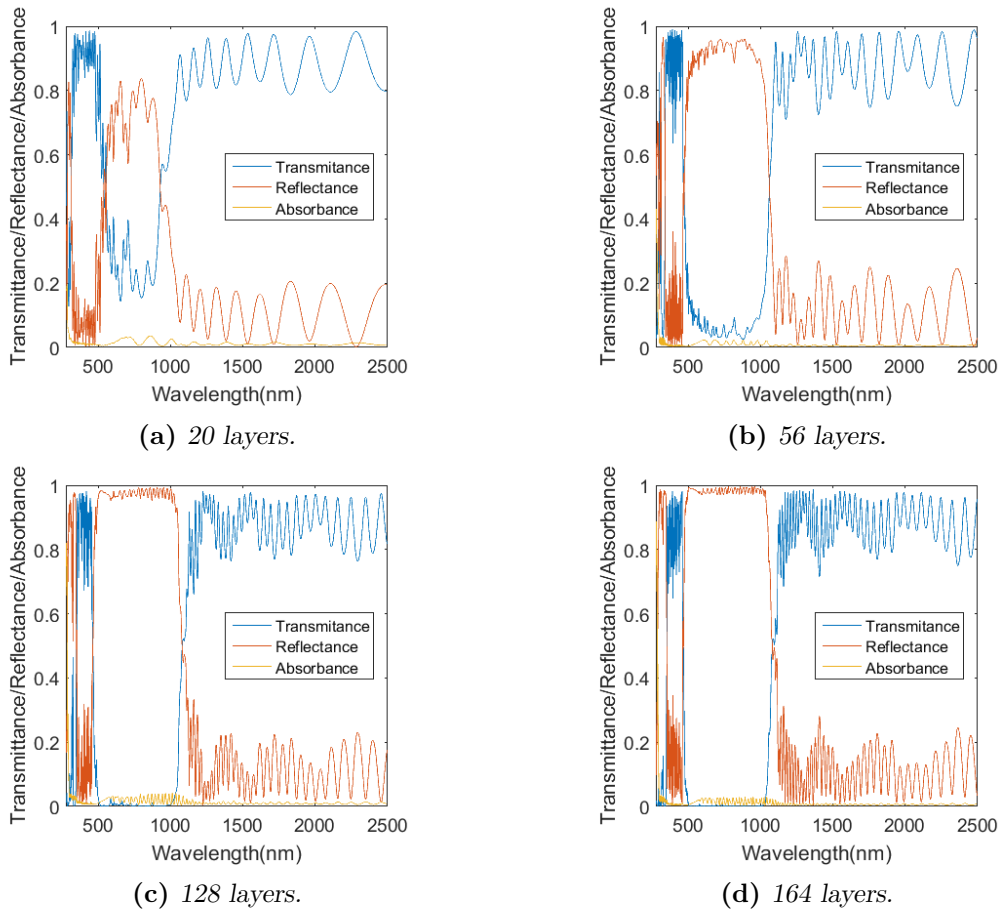


Figure 7.9: transmittance, reflectance, and absorbance for optimized structures consisting of 20, 56, 128 and 164 layers for the microcrystalline solar cell. The transmittance gets more ideal when more layers are applied.

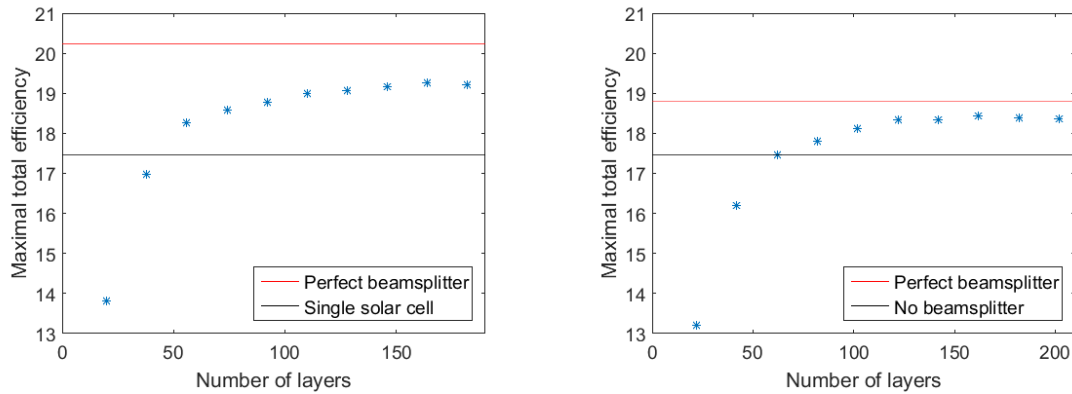


Figure 7.10: Maximal total efficiency as a function of number of layers for fixed η_{TE} for the microcrystalline solar cell.

Another way to a finer optimization is to modify the four processes in Fig. 5.4 during the optimization, such that e.g the reflected point R is closer than W to the line BG , and

similar modifications can be made for the other processes.

The maximal total efficiency is found to be 19.25% for 164 layers, thus a relative improvement of 10.2% compared to a single solar cell is achieved. The thicknesses of the optimized structure are found in table A.4 in Appendix A, and these thicknesses are to be used when fabricating the beamsplitter.

The same is done for $\eta_{TE} = 4\%$ and when calculating the transmittance, reflectance, and absorbance for the optimized structures, they are found to be very similar to those in Fig. 7.9. The desired band gap is broader compared to that for $\eta_{TE} = 8\%$, as it was found to be 464-1079 nm for $\eta_{TE} = 4\%$ and 489-1054 nm for $\eta_{TE} = 8\%$ as mentioned in the previous section. Hence a little more light is directed onto the solar cell when $\eta_{TE} = 4\%$, and the efficiency of the hybrid system as a function of number of layers is seen in Fig. 7.10b, where a perfect beamsplitter is found to give an efficiency of 18.79%. The graph shows same behaviour as Fig. 7.10a but now 82 layers are required to satisfy the necessary condition, where 122 were required for the ideal solar cell as seen in Fig. 7.2. The sequence flattens out for a smaller number of layers and is actually decreasing from 122-142 layers and from 162-202 layers, indicating that the sequence has converged. The maximum is found to be 18.44% for 162 layers, thus a relative improvement of 5.5% compared to a single solar cell is achieved. The thicknesses of the optimized structure are found in table A.3 in Appendix A.

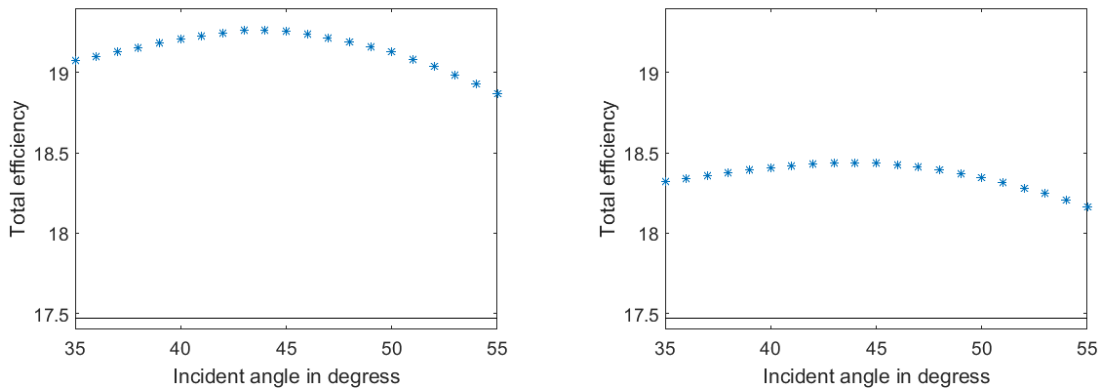
Notice that the distance between the black and red line in Fig. 7.10a is approximately twice as big as in Fig. 7.10b, and this also applies for the distance between the best point and the red line. For $\eta_{TE} = 8\%$ the relative improvement compared to a single solar cell was found to be 10.2%, while the number was 5.5% for $\eta_{TE} = 4\%$. The improvement is almost twice as big when the thermoelectric efficiency is doubled, indicating that for small thermoelectric efficiencies the relative improvement scales approximately linear with it. Same result is obtained in [4] where the relative improvement is plotted against η_{TE} in Fig. 3 and is seen to be approximately linear. Hence one way to improve the efficiency of the hybrid system is to increase the efficiency of the thermoelectric element, and this can be done totally independent of the solar cell and the beamsplitter design. This shows the fact that cooperation with researchers in e.g thermoelectricity has the potential to increase the efficiency of the hybrid system, as they probably have some ideas to increase the thermoelectric efficiency.

7.2.2 Efficiency as a Function of Incident Angle

This subsection is analogue to Sec. 7.1.2 and examines the efficiency as a function of incident angle for a microcrystalline solar cell where the applied structure is optimized for 45° .

For $\eta_{TE} = 8\%$ the optimal number of layers was found to be 164 as seen in Fig. 7.10a, and therefore the angle is varied when the optimized structure consisting of 164 layers is kept constant. As in Sec. 7.1.2 the angle is varied from 35° - 55° and the efficiencies are seen in Fig. 7.11, where the highest efficiency is found to be 19.27% for an angle of 44° even the structure is optimized for 45° giving an efficiency of 19.25%. The black horizontal line is the efficiency of a single microcrystalline solar cell at 17.47%. The efficiency as function of angle is approximately parabolic in contrast to the efficiency for the ideal solar cell in Fig. 7.4b where it was almost constant for angles smaller than 45° but decreased rapidly for larger angles. As explained in Sec. 7.1.2 a larger incident angle implies a smaller cut off wavelength, which must apply to both cut off wavelengths when the wavelength interval now consists of three parts instead of two for the ideal solar cell.

Hence a larger angle implies that both cut off wavelengths get smaller and the entire



(a) Total efficiency as a function of angle for $\eta_{TE} = 8\%$ where the structure consists of 164 layers. The critical angle is 71° .

(b) Total efficiency as a function of angle for $\eta_{TE} = 4\%$ where the structure consists of 162 layers. The critical angle is 66° .

Figure 7.11: Total efficiency as a function of angle for fixed η_{TE} and number of layers. The black horizontal lines are the efficiency of a single microcrystalline solar cell at 17.47%.

band gap shifts towards smaller wavelengths. The efficiency as a function of wavelengths for the microcrystalline solar cell was seen in Fig. 7.6b where the optimal band gap is between the two intersections of the blue curve and one of the red curves. Shifting the band gap towards smaller wavelengths imply that the efficiency just below the upper cut off wavelength is replaced by the efficiency just below the lower cut off wavelength, which leads to a reduction of the total efficiency. Hence the band gap shift implies that the wavelength dependent efficiency decreases from 15-20% to 4 or 8%, hence not much compared to the ideal solar cell, where the decrease is from almost 100% down to 4 or 8%. Thus for the microcrystalline solar cell the change in efficiency caused by the downward band gap shift is relatively small, implying that the total efficiency decreases less as function of the angle than for the ideal solar cell.

Similar a smaller incident angle implies that the band gap gets shifted towards higher wavelengths, and the efficiency just above the lower cut off wavelength is replaced by the efficiency just above the upper cut off wavelength, which implies a reduction in the total efficiency. As the efficiency in Fig. 7.6b is not bell shaped but high efficiency is found for larger angles, the reduction in total efficiency is highest when the band gap is shifted towards lower wavelengths. Hence the efficiency is faster decreasing for larger angles than for smaller angles, which is also indicated in Fig. 7.11a. Increasing the angle above 55° it is found that the critical angle is 71° , where it was only 57° for the ideal solar cell, but decreasing the angle below 35° no lower critical angle is found. Even for an incident angle of 0° the efficiency is found to be 18.45% thus almost one percentage point above the black line.

The same is done for $\eta_{TE} = 4\%$ and from Fig. 7.10b it was found that 162 layers were optimal, and the angle is therefore changed from $35-55^\circ$ when the number of layers is kept constant at 162. The efficiency as function of angle is seen in Fig. 7.11b and follow same tendency as in Fig. 7.11a. The maximal efficiency is found to be 18.44% for both 44 and 45° and is approximately parabolic in the small angle interval. The two figures have same axes and when $\eta_{TE} = 4\%$ the efficiency is shifted downwards compared to $\eta_{TE} = 8\%$. The critical angle is found to be 66° , and for an incident angle of 0° the efficiency is found to be 17.81%, thus still above the black line.

7.3. Results for an Amorphous Solar Cell

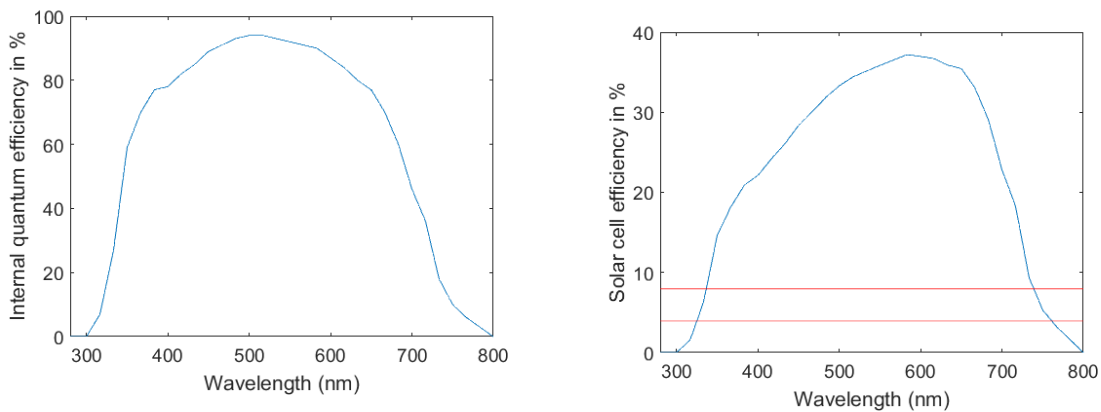
The effect of the imaginary part of the refractive index for MgF_2 is briefly studied as in Sec. 7.1.3. When the imaginary part is the one in Fig. 6.1b the thickness of the front layer is found to be 65 nm as seen as the first number in Table A.4 and the efficiency of the hybrid system becomes 19.25%. Setting the imaginary part to zero the thickness of the front layer is found to be 118 nm and the efficiency increases to 19.60%, thus 0.35 percentage points higher, where this increase was only 0.02 percentage points for the ideal solar cell. The new efficiency is 12.2% higher than that of a single solar cell, where it was 10.2% higher when MgF_2 has an imaginary part. Hence in the case of a microcrystalline solar cell, it is noticeable better to apply a material without an imaginary part on the refractive index. But as explained earlier such a material does not exist naturally and it is possible that the expenses in trying to fabricate such a materials exceed the benefit of the improved efficiency.

The last couple of pages were the results for a microcrystalline solar cell and same kind of results are found for an amorphous solar cell in the following section.

7.3 Results for an Amorphous Solar Cell

In this section an amorphous solar cell is studied and its efficiency found as function of number of layers and incident angle.

Like for the microcrystalline solar cell, to calculate the solar cell efficiency it is necessary to know the internal quantum efficiency, the reflectance, coverage factor and fill factor. It has not been possible to find some data points for the internal quantum efficiency, as was the case for the microcrystalline solar cell where data was found from [11], but a plot of IQE against wavelength is found in article [13] where the band gap wavelength of the amorphous solar cell is 800 nm. The data points are therefore manually read from the article and interpolated in the wavelength interval, and are seen in Fig. 7.12a. The upper band gap edge is 800 nm where it was 1170 for the microcrystalline solar cell in Fig. 7.6a, and the maximal internal quantum efficiency is found to be 94% for a wavelength of 520 nm. According to [13] the fill factor is 0.6296, the coverage factor is not mentioned and the reflectance is strongly dependent on wavelength, and it is a rough approximation to



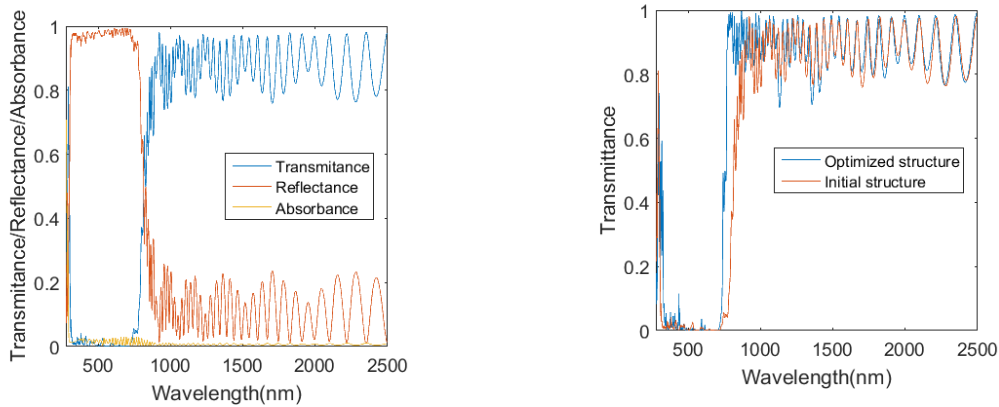
(a) Internal quantum efficiency for the considered amorphous solar cell with a band gap wavelength of 800 nm. Data manually read from [13].

(b) Efficiency as function of wavelength for the considered amorphous solar cell. The ideal band gap for the beamsplitter is 325-762 nm for $\eta_{TE} = 4\%$ and 337-740 nm for $\eta_{TE} = 8\%$.

Figure 7.12: Data for the considered amorphous solar cell.

consider it as a constant of 0.1 as done in this thesis. With these numbers the efficiency as a function of wavelength is found from Eq. (3.8) and is seen in Fig. 7.12b, where the two red horizontal lines are the thermoelectric efficiencies of 4 and 8% and the ideal band gap is found to be 325-762 nm for $\eta_{TE} = 4\%$ and 337-740 nm for $\eta_{TE} = 8\%$. The overall efficiency is given in Eq. (3.9) and is found to be 15.77%, while it is reported in [13] to be only 9.47%, which is found from the fill factor, a measured short circuit density of 17.519mA/cm² and a measured open circuit voltage of 858mV. The large deviation between the calculated efficiency and the one from the article must partly be due to the rough approximation in the reflectance, and the possibility that the article uses some of the parameters for the semiconductor that are not considered in this thesis. Another reason for the large deviation is the fact that the efficiency of 9.47% is measured for a specific solar cell, where electric resistance in the contacts reduces the efficiency. This phenomena is not included at all in the calculation, as the contact area has been set to zero and no electric resistance is assumed, and it is therefore expected that the calculated efficiency becomes higher than the measured. Despite the deviance in efficiency compared to the article the efficiency in Fig. 7.12b is still applied for an amorphous solar cell. The idea in using such an efficiency is that the band gap is quite different from the one for the microcrystalline solar cell, and it is investigated which type of solar cell it will be most beneficial for when implemented in the hybrid system.

The initial guess for $\eta_{TE} = 8\%$ is found to consist of 7 blocks with 9 unit cells in each, resulting in 128 layers in total. As the band gap wavelength of the amorphous solar cell is smaller than for the microcrystalline fewer blocks are needed to give the desired band gap. The transmittance, reflectance, and absorbance for the initial guess are seen in Fig. 7.13a where it is hard to see that the wavelength interval is divided into three parts because the lower band gap edge at 337 nm is relatively close to the lower limit of 280 nm, but it is desired to have a high transmittance for wavelengths below 337 nm. The



(a) *transmittance, reflectance, and absorbance for the initial guess consisting of 128 layers for the amorphous solar cell.*

(b) *Transmittance for the initial and optimized structure consisting of 128 layers for the amorphous solar cell.*

Figure 7.13: *Comparison of transmittance for initial and optimized structure for the amorphous solar cell.*

transmittance, reflectance, and absorbance are comparable to those found for the ideal solar cell in Fig. 6.2 where a band gap of 900 nm was applied without a desired cut off for the small wavelengths. The total efficiency for the initial guess is found to be 17.98% thus more than 2 percentage points higher than for a single amorphous solar cell. The

7.3. Results for an Amorphous Solar Cell

transmittances for the optimized and initial structures are seen in Fig. 7.13b where the cut off around 740 nm is sharper for the optimized structure. The efficiency for the optimized structure is found to be 18.72% thus almost 3 percentage points higher than for a single amorphous solar cell, and the relative improvement is 18.7%, where it only was 10.2% for the microcrystalline solar cell. The reason for this must be the fact than the amorphous solar cell with the band gap wavelength of 800 nm only uses a small part of the solar spectrum, and the hybrid system ensures that wavelengths above 800 nm not are totally wasted. The improvement of approximately 3 percentage points will probably not depend so much of the solar cell efficiency as long as the band gap is unchanged, and if a solar cell with efficiency of only 9.47% is considered as in [13], it is plausible that the efficiency of the hybrid system in this case will be approximately 12.5%, and a relative improvement of approximately 30% will be achieved. Hence a solar cell with a small band gap wavelength has the potential to be most beneficial to implement in the hybrid system, and if its solar cell efficiency is low the relative improvement will be large.

The thicknesses for the optimized structure are compared to those for the initial guess as seen in Fig. 7.14, and the average change in thickness between the initial and optimized structure is found to be 6.2 nm. The front layer of MgF_2 for the optimized structure is found to be 28 nm while it was 70 nm for the initial guess. Here the front layer is to give rise to a band gap wavelength around 337 nm, where it was 489 nm for the microcrystalline case explaining why the layers of MgF_2 are thinner for the amorphous solar cell.

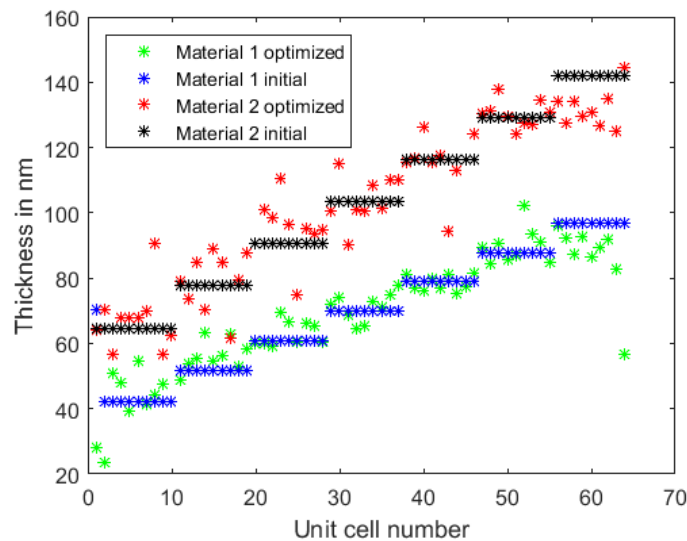


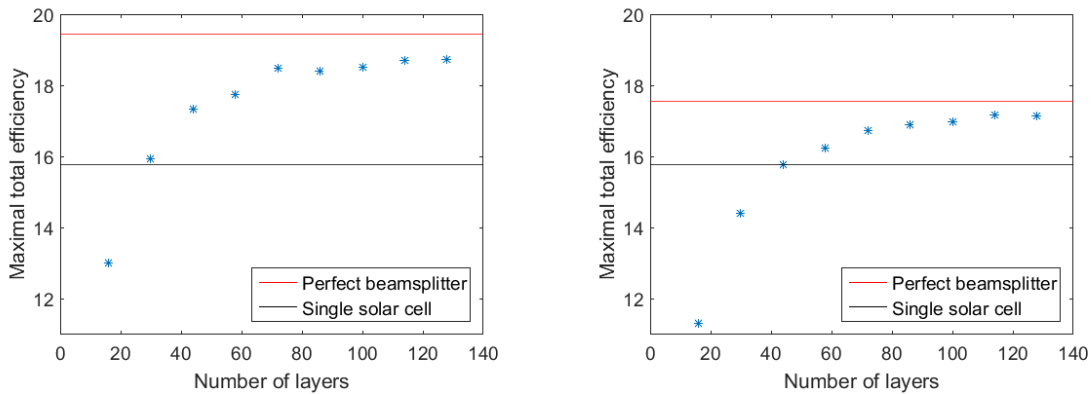
Figure 7.14: Thicknesses of all the layers for the initial and optimized structure consisting of 128 layers for the amorphous solar cell. The initial structure consists of 7 blocks as seen by the staircases, while the optimized thicknesses are distributed around them. The average change in thickness between the initial and optimized structure is 6.2 nm. Material 1 is Si_3N_4 and material 2 is SiO_2 , but the first layer of material 1 is MgF_2 .

Until now for the amorphous solar cell the number of layers has been 128 and the incident angle has been 45° , and they are varied in the two next subsections in order to find the efficiency as a function of number of layers and of incident angle.

7.3.1 Efficiency as a Function of Number of Layers

This subsection is analogue to Sec. 7.1.1 and 7.2.1 and examines the efficiency as a function of number of layers for an amorphous solar cell when the incident angle is kept constant at 45° .

The transmittance, reflectance, and absorbance calculated for different number of layers are very similar to those in Fig. 7.1 and 7.9, and are therefore not included. The maximal efficiency is found when the number of layers is varied from 16 to 128 and are seen in Fig. 7.15a, where the efficiency of a perfect beamsplitter is found to be 19.43%. The necessary condition is satisfied using just 30 layers where 56 layers were required for the microcrystalline solar cell as seen in Fig. 7.10a. The sequence is decreasing by 0.08% when the number of layers increases from 72 to 86, but is otherwise increasing to its maximum of 18.72% when 128 layers are present, which was also the considered number in the previous section. The thicknesses of the optimized structure are found in table A.2 in Appendix A. The same is done for $\eta_{TE}=4\%$ and its efficiency as function of number of layers is seen in Fig. 7.15b, where the efficiency of a perfect beamsplitter is found to be 17.56%. The maximum is found to be 17.18% for 114 layers thus a relative improvement of 8.9% is achieved, where 18.7% was achieved when $\eta_{TE}=8\%$ supporting the fact that the relative improvement scales approximately linear with η_{TE} as also found in [4]. The thicknesses of the optimized structure are found in table A.1 in Appendix A.



(a) Maximal total efficiency as a function of number of layers for $\eta_{TE}=8\%$ for the amorphous solar cell.

(b) Maximal total efficiency as a function of number of layers for $\eta_{TE}=4\%$ for the amorphous solar cell.

Figure 7.15: Maximal total efficiency as a function of number of layers for fixed η_{TE} for the amorphous solar cell.

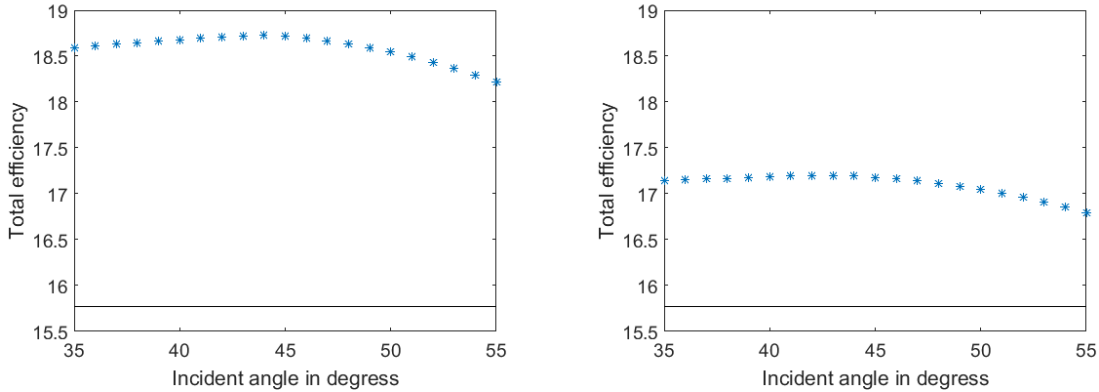
7.3.2 Efficiency as a Function of Incident Angle

This subsection is analogue to Sec. 7.1.2 and 7.2.2 and examines the efficiency as a function of incident angle for an amorphous solar cell where the applied structure is optimized for an incident angle of 45° .

The same is done as earlier where the number of layers is kept constant at the value giving the highest efficiency in Fig. 7.15, which was found to be 128 for $\eta_{TE}=8\%$ and 114 for $\eta_{TE}=4\%$. Varying the incident angle from 35° - 55° gives the efficiencies in Fig. 7.16, where the maximum is 18.73% for 44° when $\eta_{TE}=8\%$ and 17.19% for 44° when $\eta_{TE}=4\%$. The efficiencies show same parabolic behaviour as the microcrystalline solar cell in Fig. 7.11, and the critical angles for $\eta_{TE}=8\%$ and 4% are found to be 74° and 69° , respectively, and

7.4. Orientation of the Beamsplitter

for an incident angle of 0° the efficiencies are 18.17% and 16.89%, thus significantly higher than for a single solar cell, supporting the fact that there is no lower critical angle.



(a) Total efficiency as a function of angle for $\eta_{TE} = 8\%$ where the structure consists of 128 layers.

(b) Total efficiency as a function of angle for $\eta_{TE} = 4\%$ where the structure consists of 114 layers.

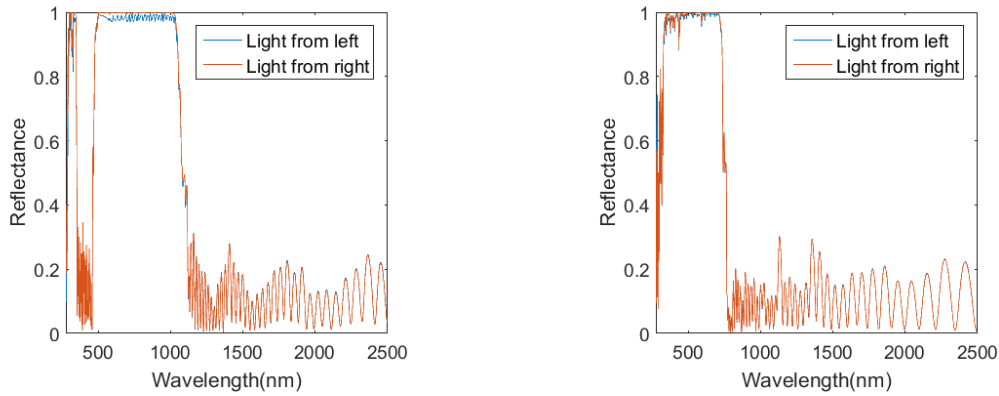
Figure 7.16: Total efficiency as a function of angle for fixed η_{TE} and number of layers. The black horizontal lines are the efficiency of a single amorphous solar cell at 15.77%.

For the amorphous solar cell with removed imaginary part of the refractive index for MgF_2 the thickness of the front layer is found to be 73 nm, where it was 28 nm before as seen as the first number in Table A.2. The efficiency is found to be 18.73%, thus only 0.01 percentage points higher than before. Hence for the amorphous solar cell it is not worthwhile trying to fabricate such an artificial material.

7.4 Orientation of the Beamsplitter

Until now the orientation of the beamsplitter has been as in Fig. 2.11 with MgF_2 as the first layer and glass as the last layer. As mentioned in Sec. 2.4.1 reciprocity causes that the transmittance through the beamsplitter is the same as if light is incident from the other direction, but the reflectance and absorbance depend on the orientation of the beamsplitter as seen in Fig. 2.9. One of the purposes of the beamsplitter is to reflect the light in the band gap where the transmittance is small, but it is also possible that this light is absorbed instead of reflected which will decrease the efficiency of the hybrid system. The optimal orientation of the beamsplitter is the one with the highest reflectance in the band gap. The reflectance is calculated for light incident from both sides on the same beamsplitter and is seen in Fig. 7.17a for a microcrystalline solar cell and in Fig. 7.17b for an amorphous solar cell.

In both figures the difference between the two directions is largest in the band gap and the reflectance is highest for light incident from right as it is almost equal to one in the entire band gap while oscillations exist when light is incident from left, which is most clearly seen in Fig. 7.17a. For light incident from left absorbance occur mostly in the band gap as seen in Fig. 7.9, and it is noticed that the reflectance in Fig. 7.9d is the same as the reflectance for light incident from left in Fig. 7.17a. In the band gap no light is transmitted through the beamsplitter and must either be reflected or absorbed in MgF_2 layer. At the first interface between air and MgF_2 some light is reflected and another part transmitted into the beamsplitter, but when it cannot be transmitted it is reflected at other interfaces and



(a) Reflectance for light incident from left and right on the optimized beamsplitter consisting of 164 layers when a microcrystalline solar cell is applied and $\eta_{TE} = 8\%$.

(b) Reflectance for light incident from left and right on the optimized beamsplitter consisting of 128 layers when an amorphous solar cell is applied and $\eta_{TE} = 8\%$.

Figure 7.17: Reflectance for light incident from left and right on an optimized beamsplitter. In the band gaps the reflectance is highest for light incident from right and the optimal orientation is opposite as considered earlier.

transmitted through the MgF_2 layer again on the way out of the beamsplitter. Hence the light has possibly to pass through the absorbing layer more than once, implying that the absorbance increases in the band gap. Outside the band gap the light can be transmitted through the entire beamsplitter, thus it is only necessary to pass through the absorbing layer once and the absorbance gets smaller.

On the other hand when light is incident from the opposite direction, MgF_2 is the final layer and much of the light is reflected before entering the absorbing layer, and the absorbance is therefore smallest for this orientation and the reflectance is highest. This direction is opposite of what has been done so far, thus it is better to change the orientation of the beamsplitter such that the light enters the structure from the glass side and leaves it from the MgF_2 layer, as illustrated in Fig. 7.18 where the orientation is opposite of Fig. 2.11. Notice that this is opposite of the example with a metal film deposited on glass from [19] as illustrated in Fig. 2.9. The reason for this deviation must be that [19] only considers a metal layer and a glass layer, while the beamsplitter studied here contains more than 100 layers and many more reflections can therefore occur.

The efficiency is calculated for the reversed orientation and is found to be 19.52% for the microcrystalline and 18.81% for the amorphous for $\eta_{TE} = 8\%$ where the numbers were 19.25% and 18.72% for the original orientation. For $\eta_{TE} = 4\%$ the efficiencies are found to be 18.45% and 17.22%, where they were 18.44% and 17.18% for the original orientation. The critical angles are found in the same way as earlier and yield 66° and 75° for the microcrystalline solar cell and 70° and 75° for the amorphous.

7.5. Results for a Low-wavelength-pass Beamsplitter

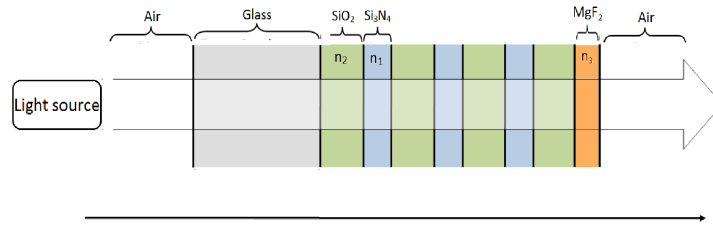


Figure 7.18: Optimal orientation of the beamsplitter where light enters from the glass side and leaves from the MgF_2 side. This orientation is opposite of Fig. 2.11 and of what has been done so far.

7.5 Results for a Low-wavelength-pass Beamsplitter

Until now the thesis has considered a high-wavelength-pass beamsplitter whose purpose is to reflect the short wavelengths onto the solar cell as seen in Fig. 1.1b where the thermoelectric element is below the beamsplitter. A low-wavelength-pass beamsplitter as suggested in [33] is seen in Fig. 1.1a and is studied in detail in this section. Because of the switch in position between the solar cell and thermoelectric element the ideal transmittance is completely opposite to that in Fig. 1.3b and is instead seen in Fig. 7.19 where the three important parts of the wavelength interval are clearly seen. As for the high-wavelength-pass beamsplitter the ideal reflectance equals one in the region where the ideal transmittance is zero, thus absorption is not present in the ideal case as expected.

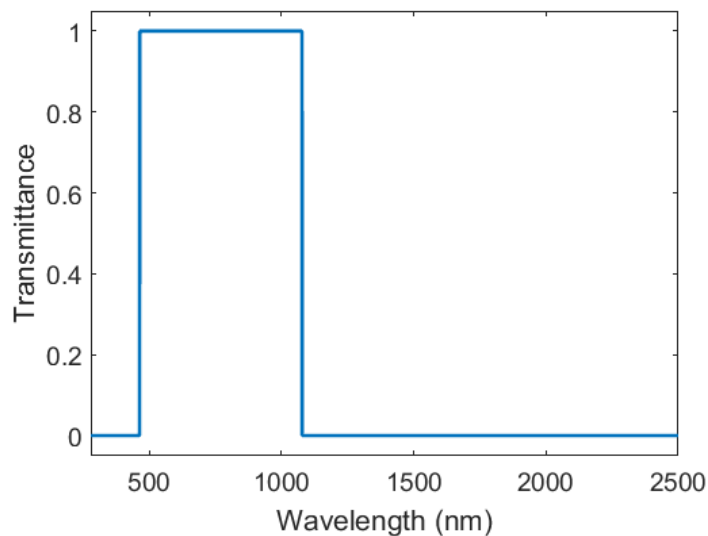


Figure 7.19: Ideal transmittance for a low-wavelength-pass beamsplitter. The very short wavelengths are reflected onto the thermoelectric element, the medium long wavelengths transmitted onto the solar cell while the longest wavelengths are reflected onto the thermoelectric element.

7.5.1 Origin of Higher Order Band Gaps

In this subsection the origin of higher order band gaps is explained.

An initial guess is needed in order to run the optimization program, but it turns out that it is impossible to have a good initial guess whose transmittance is close to the ideal one in Fig. 7.19. The layers are constructed from Eq. (2.30) with a thickness of $a = \lambda_0/(4n \cos \theta)$ where λ_0 is the design wavelength for the band gap in the beamsplitter and θ is the propagation angle in the material. As explained in Sec. 2.3.1 these thicknesses imply a phase change of $\pi/2$ after propagating through the layer, thus propagating forth and back implies a phase change of π . The interface from low to high refractive index also gives a phase change of π , leading to constructive interference between the waves reflected at the first and second interfaces, and similar occur for the other interfaces. [17] If a wavelength of $\lambda = \lambda_0/3$ is incident on the structure, the phase changes after propagation through each layer becomes $3\pi/2$ instead of $\pi/2$, but the reflected waves are still in phase and constructive interference occurs, thus a band gap of a third of the design wavelength also exists. This is the first higher order band gap and similar band gaps are found for $\lambda = \lambda_0/5$, $\lambda = \lambda_0/7$ and so on. The three times shorter wavelengths have a three times higher energy, and these higher order band gaps are seen in the dispersion relations in Fig. 2.3. Another way to show the existence of the higher order band gaps is from Eq. 2.28, which contains factors like $\cos(a_1 k_{z1})$ on its right hand side. For real refractive indices it is found that

$$\cos(a_1 k_{z1}) = \cos\left(\frac{\lambda_0}{4n_1 \cos \theta} \frac{2\pi}{\lambda} n_1 \cos \theta\right) = \cos\left(\frac{\pi}{2} \frac{\lambda_0}{\lambda}\right), \quad (7.1)$$

where it is utilized that a_1 has the optimal thickness of $\lambda_0/(4n_1 \cos \theta)$. When $\lambda = \lambda_0$ the factor in Eq. (7.1) equals zero, similar is found when $\lambda = \lambda_0/3$, and the same argument applies for the other factors in Eq. (2.28), showing that its right side is unchanged when the wavelength is a third of the design wavelength, and higher order band gaps therefore exist at these energies.

If the structure is still periodic but does not consist of quarter wave layers, a phase shift after propagating through a periodic of an integer times π still gives rise to constructive interference. This implies that higher order band gaps occur for $\lambda = \lambda_0/m$, where m is any integer and not just odd. This is also seen in the dispersion relations in Fig. 2.3 where the structure slightly deviates from being quarter wave layers, which leads to the small band gaps that would not be present if a perfect quarter wave structure was applied. These small band gaps are found for an energy twice as big as for the first band gap coming from the first higher order band gap at $\lambda = \lambda_0/2$.

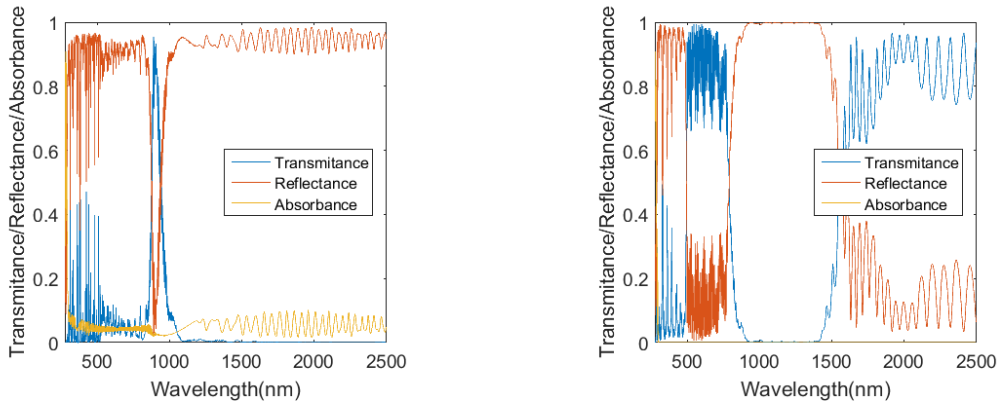
7.5.2 Low-wavelength-pass Beamsplitter for a Microcrystalline Solar Cell

In this subsection the effect of higher order band gaps is examined for the microcrystalline solar cell and it is investigated whether it is possible to construct a low-wavelength-pass beamsplitter.

For the microcrystalline solar cell with $\eta_{TE} = 8\%$ the desired band gap now becomes from 1054-2500 nm as illustrated in Fig. 7.19, and the first higher order band gap at a third of the wavelength becomes from approximately 350-870 nm, and next band gap at a fifth of the wavelength from approximately 210-500 nm. The structure consists of quarter wave layers, thus the other higher order band gaps are not seen here. These two higher order band gaps together exists for the wavelengths from approximately 210-870, thus covering a large part of the interval where no band gap is desired. Following the same method as in Sec. 6.2.1 to construct the initial guess, it is found to consist of 13 blocks with 7 unit cells

7.5. Results for a Low-wavelength-pass Beamsplitter

in each, resulting in 184 layers in total. The transmittance, reflectance, and absorbance for the initial guess is seen in Fig. 7.20a, where a complete band gap is seen for wavelengths above approximately 1080 nm. It was desired to have a high transmittance from 489-1054 nm, but the higher order band gaps cover the most of this interval and the transmittance is only high from approximately 860-980 nm as seen in the figure, and the transmittance is not at all close to the ideal one in Fig. 7.19. If a narrower band gap is desired it is



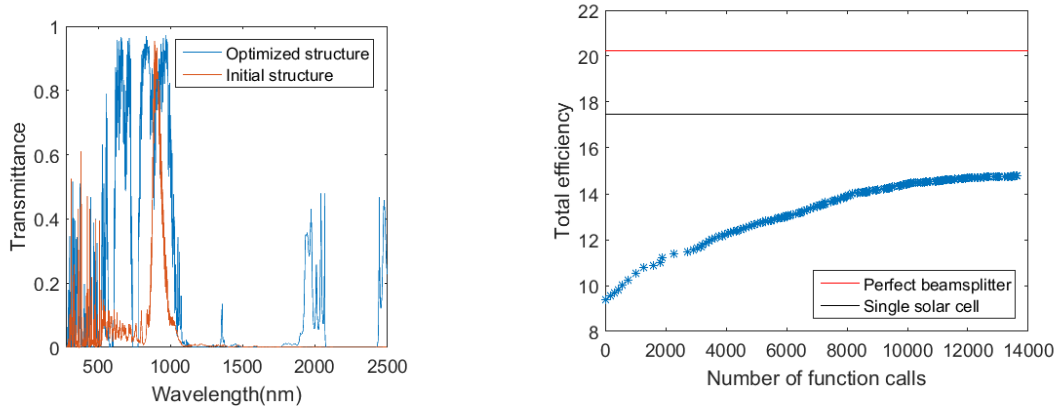
(a) transmittance, reflectance, and absorbance for the initial guess for a low-wavelength-pass beamsplitter consisting of 184 layers.

(b) transmittance, reflectance, and absorbance for a structure with a desired band gap from 900-1500 nm for a beamsplitter consisting of 98 layers.

Figure 7.20: transmittance, reflectance, and absorbance for two different structures for a low-wavelength-pass beamsplitter.

possible to have a high transmittance for wavelengths below the band gap, and an example of this is seen in Fig. 7.20b which shows the transmittance, reflectance, and absorbance for a structure consisting of 98 quarter wave layers where the desired band gap is from 900-1500 nm. A band gap is found in the desired region and the first higher order band gap from approximately 300-500 nm, but a high transmittance is found from 500-900 nm because it is not covered by any band gap. The next band gap at a fifth of the wavelength becomes from approximately 180-300 nm and is therefore not seen in the figure. Hence it seems problematic to have a low-wavelength-pass beamsplitter, as it cannot reflect the long wavelengths without also reflecting the short ones. To examine whether it is possible to somehow construct such a low-wavelength-pass beamsplitter anyway, the optimization program is run with a modified `eta_function` with R and T interchanged in Eq. (4.20) to calculate the efficiency for the hybrid system with a low-wavelength-pass beamsplitter. The transmittance for the optimized low-wavelength-pass beamsplitter is seen in Fig. 7.21a together with that for the initial guess, and the optimized structure is seen to be significantly better than the initial guess. The transmittance becomes high in some parts of the desired region, but it still far from the ideal transmittance for the low-wavelength-pass beamsplitter, and furthermore the desired band gap is not complete as non-negligible transmittance occur for some wavelengths above 1054 nm. The efficiency for the initial guess is found to be 9.39% thus far from the limit of 17.47% for a single microcrystalline solar cell, and for the optimized structure it is found to be 14.77%, thus still far below the limit.

It is therefore concluded that it is not possible to have a beamsplitter that transmits the short wavelengths and reflects the long. The efficiency for the optimization process is seen in Fig. 7.21b, where the increase is remarkably higher than for the high-wavelength-pass



(a) Transmittance for the initial and optimized structure for a low-wavelength-pass beamsplitter for the microcrystalline solar cell

(b) Efficiency for the low-wavelength-pass beamsplitter for a microcrystalline solar cell. The optimization process uses almost 14000 function calls and achieves an increase of more than 5 percentage point, which is much more than for the high-wavelength-pass beamsplitter as seen in Fig. 6.8.

Figure 7.21: Transmittance and efficiency of a low-wavelength-pass beamsplitter for a microcrystalline solar cell.

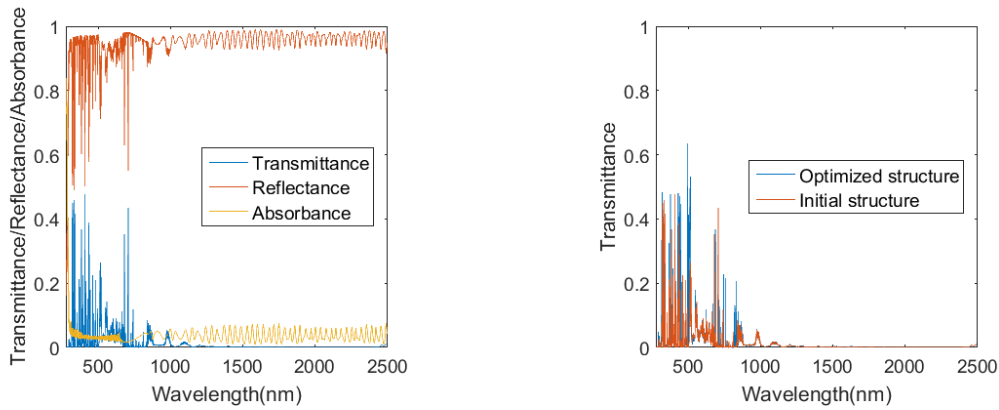
beamsplitter considered so far. For comparison, see the efficiency for the ideal solar cell for a high-wavelength-pass beamsplitter in Fig. 6.8, where the increase is approximately 0.8 percentage point using 5000 function calls. For the microcrystalline and amorphous solar cells the increase during the optimization process is typical also less than 1 percentage point and uses less than 5000 function calls. Optimizing the low-wavelength-pass beamsplitter demands almost 14000 function calls, and results in an increase of more than 5 percentage point. This is due to the fact that the initial guess is far from the optimal and great improvement opportunities exist for the optimization process, which therefore uses many function calls. The initial guesses for the high-wavelength-pass beamsplitter usually were relatively close to the ideal and fewer function calls are therefore needed during the optimization. But as seen in the figure even the optimized efficiency is still far below the limit of a single solar cell illustrated as the black line, and it is thus impossible to construct such a low-wavelength-wavelength-pass beamsplitter to be implemented in the hybrid system to increase the efficiency.

7.5.3 Low-wavelength-pass Beamsplitter for an Amorphous Solar Cell

In this subsection the same is done for the amorphous solar cell.

In the same way it is tried to construct a low-wavelength-pass beamsplitter for the amorphous solar cell with $\eta_{TE} = 8\%$, where the desired band gap is from 740-2500 nm. The band gap is broader than for the microcrystalline solar cell, thus the initial guess is found to consist of 15 blocks with 8 unit cells in each, resulting in 242 layers in total. The transmittance, reflectance, and absorbance for the initial guess are seen in Fig. 7.22a, where the band gap is almost complete in the desired region. But as in the microcrystalline case, the transmittance is also very small in the region where it was desired to have a high transmittance, and again the initial guess is far from optimal. Because of the broader band gap, the first higher order band gap is from approximately 250-870 nm and covers the entire region where no band gap was desired, and the transmittance is therefore small

7.6. Conclusion on the Results



(a) transmittance, reflectance, and absorbance for the initial guess for a low-wavelength-pass beamsplitter for the amorphous solar cell.

(b) Transmittance for the initial and optimized structures for a low-wavelength-pass beamsplitter for the amorphous solar cell.

Figure 7.22: Comparison of transmittance for initial and optimized structure for a low-wavelength-pass beamsplitter for the amorphous solar cell.

in that region. Hence the initial guess for the low-wavelength-pass beamsplitter with an amorphous solar cell is even worse than for the microcrystalline case, because no region with a high transmittance is found as it was the case for the microcrystalline in Fig. 7.20a. The transmittances for the optimized and initial structure are seen in Fig. 7.22b, where the optimized transmittance is only slightly better than for the initial guess and still far from the ideal one.

The efficiency for the initial guess is found to be 8.42%, thus far below the limit of 15.77% which is the efficiency of a single amorphous solar cell. The efficiency of the optimized structure is found to be 8.44%, thus only 0.2 percentage points higher than the initial guess and still far below the limit.

For both solar cell types it is thus concluded that it is not possible to construct a low-wavelength-pass beamsplitter using the ideas presented in this thesis. If such a beamsplitter is to be constructed in some way, it is probably to consist of materials whose refractive indices significantly change as a function of wavelength, and such materials are not known today, and a lot of research is to be done in order to fabricate such artificial materials.

7.6 Conclusion on the Results

This section contains a conclusion on the obtained results for the microcrystalline and amorphous solar cell.

The important results obtained in this chapter are summarized in Table 7.1. For both solar cell types the optimized efficiencies are higher when $\eta_{TE} = 8\%$ than when it is 4%, as expected, and the relative improvement of the total efficiency compared with a single solar cell is found to be approximately linearly increasing with η_{TE} which is also found in [4]. The efficiency of an amorphous solar cell is smaller than for a microcrystalline, and the maximal total efficiencies are therefore also smaller. But the improvement is found to be larger for the amorphous solar cell which is due to the fact that it has a lower band gap wavelength, and thereby in itself utilizes a smaller fraction of the solar spectrum than the microcrystalline solar cell. The relative improvement of the hybrid system using the amorphous solar cell is almost almost twice as big than for the microcrystalline solar cell as seen in the 6th row in the table, and approximately the same result is obtained in [4]

Solar cell type	Microcrystalline	Microcrystalline	Amorphous	Amorphous
Thermoelectric efficiency	4%	8%	4%	8%
Single solar cell	17.47%	17.47%	15.77%	15.77%
Perfect beamsplitter	18.79%	20.23%	17.56%	19.43%
Optimized beamsplitter	18.44%	19.25%	17.18%	18.72%
Number of layers	162	164	114	128
Relative improvement	5.5%	10.2%	8.9%	18.7%
Critical angle	66°	71°	69°	74°
Low-pass beamsplitter	No	No	No	No
Reverse orientation				
Optimized beamsplitter	18.45%	19.52%	17.22%	18.81%
Relative improvement	5.6%	11.7 %	9.1 %	19.2%
Critical angle	70°	75°	69°	75°

Table 7.1: Overview of the results for the microcrystalline and amorphous solar cell where the last three rows are for the reverse orientation of the beamsplitter. The thicknesses of the optimized beamsplitters are seen in Appendix A.

where other data for the solar cell efficiency has been applied and a perfect beamsplitter assumed. The hybrid system ensures that wavelengths for the entire solar spectrum is partly utilized, and this is therefore most beneficial for the amorphous solar cell. When it also has a lower efficiency the relative improvement gets larger too and is 18.7%. Another advantage in using the amorphous solar cell is that the optimized beamsplitter consists of significantly fewer layers.

The efficiencies for both solar cell types are found to be approximately parabolic as a function of incident angle, where the maximum occurs for angles close to 45°. The curvature of the parabola is relative small and the efficiency only changes slightly when the angle is varied from 35-55°, hence the beamsplitter is not so sensitive to incident angle. This is a nice property as it therefore becomes unnecessary to use different beamsplitters optimized for different incident angles but the optimized beamsplitter in this thesis should be enough.

It is found that higher order band gaps make it impossible to construct a low-wavelength-pass beamsplitter, and the optimization process for both solar cell types yield that the efficiency of the hybrid system when a low-wavelength-pass beamsplitter is applied is smaller than the efficiency of a single solar cell. The configuration of the hybrid system must therefore be that of a high-wavelength-pass beamsplitter as seen in Fig. 1.1b.

At last it is found that the efficiency of the hybrid system increases if the orientation of the beamsplitter is reversed, such that light enters the beamsplitter from the glass side and leaves it from the MgF₂ side as illustrated in Fig. 7.18. The last three rows in the table are the results when the beamsplitter is reversed.

8. Conclusion

In the thesis a design of a beamsplitter for a hybrid system consisting of a solar cell and a thermoelectric element has been studied, where the beamsplitter directs the relevant part of the solar spectrum onto the solar cell and the remaining part onto the thermoelectric element. The beamsplitter consists of more than 100 alternating layers of Si_3N_4 and SiO_2 deposited on glass with an outer layer of MgF_2 , and these thicknesses are optimized in order to maximize the efficiency of the hybrid system which exceeds the efficiency of a single solar cell. Thus the thesis considers the optimization of a complicated function of more than 100 variables.

Starting with Maxwell's equations an analytic solution of the wave equation for the electric field in an infinite beamsplitter has been found and band gaps are seen to occur. Two equivalent transfer matrix methods dealing with a finite beamsplitter have been derived in order to calculate the transmittance, reflectance, and absorbance through the beamsplitter. There exist regions where the transmittance is zero which correspond to the band gaps.

Solar cells have been studied and expressions for their efficiency derived. Starting with ideal solar cells without any losses an upper limit for the efficiency is found and limiting factors are taken into account in order to describe real solar cells, where a microcrystalline and an amorphous solar cell are considered in the calculations. Thermoelectric elements have been studied and expressions for their efficiency derived, where efficiencies of 4% and 8% are applied in the calculations and an expression for the total efficiency of the hybrid system is found.

Three different optimization methods have been studied in detail and implemented in Matlab in order to optimize the thicknesses of the beamsplitter. As an initial guess to the optimization process a quarter wave structure has been applied. The optimization methods are compared based on their performance and time consumption, and the Nelder-Mead method is found to be approximately 7.4 times better than the two gradient methods.

A design of the hybrid system is suggested in [33] where a low-wavelength-pass beamsplitter is assumed as illustrated in Fig. 1.1a, but due to higher order band gaps such a beamsplitter has been found impossible to construct. It is found that a design with a high-wavelength-pass beamsplitter as illustrated in Fig. 1.1b is better. For this beamsplitter type the efficiency of the hybrid system is found to be noticeable higher than for single solar cells, and that the relative improvement scales approximately linear with the thermoelectric efficiency. The microcrystalline solar cell has a higher efficiency than the amorphous, but the improvement of the efficiency is larger for the amorphous, which is due to its smaller band gap wavelength. The relative improvement for the amorphous solar cell is found to be almost twice as big as for the microcrystalline. The efficiencies are found as function of number of layers and incident angle when it varies from $35\text{-}55^\circ$, and is found to be approximately parabolic with a small curvature, thus it is sufficient to consider a beamsplitter consisting of just one optimized structure. It is found optimal to orient the beamsplitter in such a way that light enters it from the glass side and leaves from the MgF_2 side as illustrated in Fig. 7.18. Optimal thicknesses for constructing the beamsplitter are found in Appendix A.

The results for the high-wavelength-pass beamsplitter are summarized in Table 7.1.

Bibliography

- [1] Refractive index database. <http://refractiveindex.info/>. Last visited June 6, 2016.
- [2] Ewen Ritchie Alin Argeseanu and Krisztina Leban. A new solar position sensor using low cost photosensors matrix for tracking systems. OPTIM, 4, 2010.
- [3] Stephen Boyd and Lieven Vandenbergh. Convex Optimizatin. Cambridge University Press, second edition, 2009. ISBN 978-0-521-83378-3.
- [4] A. Muto X. Chen G. Chen D. Kraemer, L. Hu and M. Chiesa. Photovoltaic-thermoelectric hybrid systems: A general optimization methodology. Applied Physics Letter, 92, 2008.
- [5] John D'Errico. fminsearchbnd, fminsearchcon. <http://www.mathworks.com/matlabcentral/fileexchange/8277-fminsearchbnd-fminsearchcon/content/FMINSEARCHBND/fminsearchbnd.m>. Last visited June 6, 2016.
- [6] J. A. Dobrowolski and R. A. Kemp. Refinement of optical multilayer systems with different optimization procedures. Applied Optics, 29, 1990.
- [7] Everredtronic. <http://www.everredtronic.com/EN/TEM/thermoelectric.generator.html>. Last visited June 6, 2016.
- [8] American Society for Testing and Materials. Reference Solar Spectral Irradiance: Air Mass 1.5. <http://rredc.nrel.gov/solar/spectra/am1.5/>. Last visited June 6, 2016.
- [9] Robert M. Freund. Nonlinear programming, course number 15.084j, lecture 5 (massachusetts institute of technology: Mit opencourseware). <http://ocw.mit.edu>, 2004.
- [10] Julian H. Goldsmid. Introduction to Thermoelectricity. Springer, first edition, 2010. ISBN 978-3-642-00715-6.
- [11] Christiana Honsberg and Stuart Bowden. A collection of resources for the photovoltaic educator. <http://www.pveducation.org/>. Last visited June 6, 2016.
- [12] Roger A. Freedman Hugh D. Young and A. Lewis Ford. University Physics. Pearson Addison-Wesley, twelfth edition, 2008. ISBN 978-0-321-50130-1.
- [13] U. Kroll C. Bucher S. Fay T. Moriarty A. Shah J. Meier, J. Spitznagel. Potential of amorphous and microcrystalline silicon solar cells. Thin Solid Films, 451, 2004.
- [14] Margaret H. Wright Jeffrey C. Lagarias, James A. Reeds and Paul E. Wright. Convergence properties of the nelder-mead simplex algorithm in low dimensions. SIAM Journal of Optimization, 9, 1998.
- [15] S. G. Johnson J.N Winn, J. D. Joannopoulos and R.D Meade. Photonic Crystals - Molding the flow of light. Princeton University Press, second edition, 2008. ISBN 978-00691-12456-8.
- [16] Frederick J. Milford John R. Reitz and Robert W. Christy. Foundations of Electromagnetic Theory. Pearson, fourth edition, 2009. ISBN 978-0-321-58174-7.
- [17] Miles V. Klein and Thomas E. Furtak. Optics. 2. Edition. John Wiley & Sons, 1986. ISBN 0-471-87297-0.

- [18] PV Lighthouse. <https://www.pvlighthouse.com.au/>. Last visited June 6, 2016.
- [19] H. Angus Macleod. Thin-Film Optical Filters. CRC Press, fourth edition, 2010. ISBN 978-1-4200-7302-7.
- [20] John H. Mathews and Kurtis K. Fink. Numerical Methods Using Matlab. Prentice-Hall Inc., fourth edition, 2004. ISBN 0-13-065248-2.
- [21] Mathworks. Optimizing nonlinear functions. <http://se.mathworks.com/help/matlab/math/optimizing-nonlinear-functions.html>, 2016.
- [22] Donald Neamen. Semiconductor Physics and Devices. Mc Graw Hill, fourth edition, 2012. ISBN 978-007-108902-9.
- [23] Rolf S. Poulsen Niclas M. Andersen, Enok J. H Kristensen and Joana A.R: Sohnesen. Modellering af båndgab i en- og todimensionelle fotoniske krystaller. 2012.
- [24] Jorge Nocedal and Stephen Wright. Numerical Optimization. Springer, second edition, 2006. ISBN 978-0387-30303-1.
- [25] Lukas Novotny and Bert Hecht. Principles of Nano-Optics. Cambridge, second edition, 2012. ISBN 978-1-107-00546-4.
- [26] J.González-Hernández P. Vorobiev Yu. Vorobiev and L. Bular. Thermal-photovoltaic solar hybrid system for efficient solar energy conversion. Solar Energy, 80, 2006.
- [27] R. K. Pathria and Paul D. Beale. Statistical Mechanics. Elsevier, third edition, 2011. ISBN 978-0-12-382188-1.
- [28] Thomas Garm Pedersen. Electric, Optical & Magnetic Properties of Nanostructures, 2015.
- [29] Shirish K. Shevade. Video lecture: Global convergence theorem. <http://www.youtube.com/watch?v=0UIt48Dt-5c&feature=relmfu>, 2012.
- [30] Enok Johannes Haahr Skjølstrup. Matlab Code to Master's Thesis. <https://www.dropbox.com/sh/i9rm4o4fthu6hsa/AACdq3RaUUDPM-UqDwMjt060a?dl=0>. Last visited June 7, 2016.
- [31] A. F. Turner and P. W. Baumeister. Multilayer mirrors with high reflectance over an extended spectral region. Applied Optics, 5, 1966.
- [32] Peter Würfel. Physics of Solar Cells - From Basic Principles to Advanced Concepts. Wiley-VCH, second edition, 2009. ISBN 978-3-527-40857-6.
- [33] Gilles Flamant Peng Li Xing Ju, Zhifeng Wang and Wenyu Zhao. Numerical analysis and optimization of a spectrum splitting concentration photovoltaic-thermoelectric hybrid system. Solar Energy, 86, 2012.
- [34] Miro Zeman. Introduction to photovoltaic solar energy. <http://aerostudents.com/files/solarCells/CH1IntroductionToPhotovoltaicSolarEnergy.pdf>. Accessed on the 18th of May, 2016.

A. Thicknesses of the Optimized Beamsplitters

This appendix contains the thicknesses for the optimized beamsplitters for an amorphous and microcrystalline solar solar cell with $\eta_{TE} = 4\%$ and 8% . These thicknesses are to be used when fabricating the beamsplitter, but notice that unit cell number 1 contains the front layers and the last unit cell contains the layers directly on the glass substrate, thus when fabricating the beamsplitter the tables have to be read from behind.

Unit cell number	Si ₃ N ₄	SiO ₂	Unit cell number	Si ₃ N ₄	SiO ₂
1	12*	88	30	67	109
2	24	65	31	67	101
3	47	22	32	75	100
4	67	58	33	70	110
5	50	72	34	72	114
6	46	83	35	78	124
7	35	61	36	78	121
8	47	80	37	81	103
9	51	66	38	72	105
10	45	71	39	75	124
11	50	81	40	83	123
12	50	74	41	83	120
13	57	84	42	81	113
14	54	68	43	73	100
15	65	100	44	80	124
16	41	98	45	86	121
17	46	82	46	81	156
18	68	90	47	86	130
19	52	87	48	94	131
20	50	90	49	96	141
21	58	78	50	89	132
22	60	107	51	93	137
23	66	101	52	89	144
24	62	90	53	89	134
25	65	99	54	95	119
26	70	98	55	98	136
27	64	95	56	86	123
28	61	102	57	70	134
29	77	94			

Table A.1: Thicknesses in nm of the optimized beamsplitter for the amorphous solar cell with $\eta_{TE} = 4\%$ which consists of 114 layers. The number with a * is the thickness of the front layer of MgF₂ and all the thicknesses are rounded to an integer.

Unit cell number	Si ₃ N ₄	SiO ₂	Unit cell number	Si ₃ N ₄	SiO ₂
1	28*	64	33	65	101
2	24	70	34	73	109
3	51	57	35	71	101
4	48	68	36	75	110
5	39	68	37	78	110
6	54	68	38	81	115
7	41	70	39	77	117
8	44	91	40	76	126
9	48	56	41	80	115
10	42	63	42	77	117
11	49	79	43	81	94
12	54	74	44	75	113
13	55	85	45	77	116
14	63	70	46	81	124
15	55	89	47	89	130
16	56	85	48	84	131
17	63	62	49	91	138
18	53	79	50	86	130
19	58	88	51	87	124
20	60	91	52	102	128
21	60	101	53	94	127
22	59	98	54	91	135
23	70	110	55	85	131
24	66	97	56	96	134
25	61	75	57	92	128
26	66	95	58	87	134
27	65	94	59	93	129
28	60	95	60	86	131
29	72	100	61	89	127
30	74	115	62	92	135
31	69	90	63	83	125
32	64	101	64	57	144

Table A.2: Thicknesses in nm of the optimized beamsplitter for the amorphous solar cell with $\eta_{TE} = 8\%$ which consists of 128 layers. The number with a * is the thickness of the front layer of MgF₂ and all the thicknesses are rounded to an integer.

Unit cell number	Si ₃ N ₄	SiO ₂	Unit cell number	Si ₃ N ₄	SiO ₂
1	4*	148	42	101	151
2	3	98	43	103	145
3	70	105	44	104	164
4	71	101	45	103	161
5	65	105	46	119	161
6	66	101	47	96	166
7	66	101	48	113	159
8	67	101	49	105	157
9	64	98	50	98	169
10	72	98	51	116	160
11	68	103	52	110	169
12	68	101	53	132	165
13	76	109	54	121	169
14	84	107	55	114	164
15	83	119	56	108	168
16	70	122	57	93	163
17	70	105	58	123	176
18	89	111	59	125	175
19	83	117	60	125	182
20	79	113	61	127	174
21	88	133	62	133	162
22	85	116	63	115	177
23	78	118	64	117	182
24	83	128	65	128	184
25	87	119	66	131	187
26	84	124	67	126	194
27	91	141	68	136	191
28	88	120	69	131	191
29	82	133	70	137	189
30	91	133	71	133	195
31	90	131	72	128	202
32	92	147	73	135	183
33	93	123	74	139	196
34	96	141	75	127	197
35	92	152	76	129	204
36	92	163	77	133	196
37	95	137	78	133	193
38	96	144	79	129	193
39	99	143	80	124	168
40	94	148	81	116	276
41	104	141			

Table A.3: Thicknesses in nm of the optimized beamsplitter for the microcrystalline solar cell with $\eta_{TE}=4\%$ which consists of 162 layers. The number with a * is the thickness of the front layer of MgF₂ and all the thicknesses are rounded to an integer.

Appendix A. Thicknesses of the Optimized Beamsplitters

Unit cell number	Si ₃ N ₄	SiO ₂	Unit cell number	Si ₃ N ₄	SiO ₂
1	65*	102	42	96	148
2	67	118	43	101	146
3	75	103	44	94	134
4	68	102	45	97	140
5	68	102	46	100	158
6	68	102	47	106	160
7	68	100	48	113	166
8	67	102	49	106	163
9	67	103	50	109	152
10	70	100	51	103	160
11	72	93	52	106	163
12	77	89	53	109	162
13	74	112	54	110	161
14	68	112	55	107	167
15	77	109	56	109	169
16	75	110	57	115	176
17	73	105	58	116	173
18	72	110	59	119	177
19	75	110	60	115	174
20	80	120	61	113	167
21	86	120	62	113	174
22	79	119	63	118	176
23	77	131	64	115	178
24	89	124	65	120	180
25	84	118	66	121	181
26	83	115	67	123	179
27	81	116	68	127	186
28	84	115	69	129	188
29	86	136	70	131	190
30	90	132	71	131	191
31	81	135	72	133	189
32	89	140	73	131	189
33	92	122	74	133	190
34	91	120	75	132	193
35	88	120	76	132	192
36	88	137	77	130	190
37	96	135	78	130	196
38	100	160	79	132	193
39	101	145	80	126	189
40	100	142	81	126	176
41	97	140	82	101	286

Table A.4: Thicknesses in nm of the optimized beamsplitter for the microcrystalline solar cell with $\eta_{TE} = 8\%$ which consists of 164 layers. The number with a * is the thickness of the front layer of MgF₂ and all the thicknesses are rounded to an integer.

B. Link to Matlab Code

A big and important part of the thesis consists of the developed Matlab code, which can be found in the following link from the author's Dropbox:

<https://www.dropbox.com/sh/i9rm4o4fthu6hsa/AACdq3RaUUDPM-UqDwMjt060a?dl=0>

The folder contains 7 txt files and 9 Matlab files. The txt files contain data of refractive indices from [1] and [18], the solar spectrum from [8] and the internal quantum efficiency for the microcrystalline solar cell from [11], and to run the code it is necessary to save all these files. The MAIN FILE is the code to run as it calls all the other functions in the folder. To obtain the results presented in the thesis takes several hours depending on the computer, but the present default settings in the MAIN FILE from the link is set such that the code can be executed in few minutes. To change these settings to those in the thesis, change `lambda_diff` in line 12 from 20 to 1 and `nu` in line 23 from 1 to 8. Other results can be obtained by changing the solar cell type and beamsplitter type. It is found that the admittance method is approximately 1.5 times faster than the electric field method and that the Nelder-Mead is approximately 7.4 times faster than the gradient methods, thus it is recommended to use these methods when running the code.